

## ABSTRACT

CAO, JING. Tailorable Release of Small Molecules Utilizing Plant Viral Nanoparticles and Fibrous Matrix. (Under the direction of Julie A. Willoughby).

We have engineered *Red clover necrotic mosaic virus* (RCNMV) derived plant viral nanoparticles (PVNs) within a fibrous matrix to optimize its application for delivery and controlled release of active ingredients. RCNMV's structure and unique response to divalent cation depletion and re-addition enables the infusion of small molecules into its viral capsid through a pore formation mechanism. While this PVN technology shows a potential use in nano-scale therapeutic drug delivery, its inherent molecular dynamics to environmental stimuli places a constraint on its application and functionality as a vehicle for tailorable release of loading cargo. In this study, we enhance the understanding of the PVN technology by elucidating its mechanism for loading and triggered release of doxorubicin (Dox), a chemotherapeutic drug for breast cancer. Of critical importance is the methodology for manipulation of Dox's loading capacity and its binding location on either the exterior or interior of the virion capsid. The ability to control the active ingredient binding location provides an additional approach of tunable release from the PVN delivery vehicle besides its inherent pH- and ion- responsive release of loading cargo.

The efficacious and controlled release strategy for agricultural active ingredients, such as nematicides, is also a large social need right now. Crop infestation of plant parasite nematodes causes in excess of \$157 billion in worldwide crop damage annually. If an effective control strategy for these pests could be developed, it is estimated that the current market for effective nematicides is between \$700 million and \$1 billion each year worldwide. In this study, we report on the utilization of PVN technology to encapsulate the biological

nematicide, abamectin (Abm), within the PVN's interior capsid (PVN<sup>Abm</sup>). Creating PVN<sup>Abm</sup> addresses Abm's issues of soil immobility while rendering a controlled release strategy for its bioavailability to root knot nematodes (RKNs). The encapsulation by a PVN carrier also improves the stability of Abm as well as further isolates its toxicity from the end-user. We used this crop treatment methodology by applying PVN<sup>Abm</sup> to tomato seedlings that we artificially inoculated with RKN *M. hapla*. We show that the zone of root protection from RKN that is limited by free Abm in the soil is improved; contributing to the enhanced nematicide performance in crop protection.

Lignocellulosic materials were engineered as a supporting fibrous matrix to distribute PVN<sup>Abm</sup> or free Abm in a field-deployable matrix. This enables a cost-effective, environmentally sound method for simply applying the crop protection agent at the point of seed planting. An approach designed to be useful for smallholder farmers in East Africa regions. In addition, the chemical and physical properties of the fibrous matrix provide an additional release mechanism for transporting active ingredients. Varying the source of lignocellulosic materials and pre-processing pulping methods results in fibrous matrices with distinct difference in their cargo release rate for both Abm in free form or encapsulated in PVN. The relative slow and sustainable cargo release is achieved by incorporating with banana lignocellulosic matrix that contains higher amount of lignin in the bulk, which enables a delayed and long-term activity against nematodes. On the other hand, the decreased amount of lignin in abaca lignocellulosic matrix give rise to a burst release of loaded Abm or PVN<sup>Abm</sup>, which exhibits a simultaneous effectiveness against nematodes, but compromises the crop protection around the growing plant in the long-term.

In summary, our work demonstrates the potential for utilization of a PVN-matrix hybrid system for active ingredient delivery, where manipulating the properties and interactions among these components, active ingredient, PVN and fibrous matrix, provides unlimited possibilities for the tailorable release of active ingredients in any given application.

© Copyright 2014 Jing Cao

All Rights Reserved

Tailorable Release of Small Molecules Utilizing Plant Viral Nanoparticles and Fibrous Matrix

by  
Jing Cao

A dissertation submitted to the Graduate Faculty of  
North Carolina State University  
in partial fulfillment of the  
requirements for the degree of  
Doctor of Philosophy

Fiber and Polymer Science

Raleigh, North Carolina

2014

APPROVED BY:

---

Julie A. Willoughby  
Committee Co-Chair

---

Saad Khan  
Committee Co-Chair

---

Jon P. Rust

---

Steve A. Lommel

---

Charles H. Opperman

## **DEDICATION**

This dissertation is dedicated to my dear grandparents, my father and my mother, for their forever love and support.

## **BIOGRAPHY**

Jing Cao was born on March 21th, 1986 in Zhuzhou, Hunan Province, China. She spent eighteen years of her life and study here until graduating with her high school diploma from Zhuzhou Eight Middle School.

In 2004, she earned her Bachelor of Science degree at Beijing Institute of Clothing Technology, Beijing, China, in Textile Chemistry and a minor in International Trading and Business. Her Master of Science degree in Textile Science was complete in 2010 at University of Georgia in Athens, Georgia, and involved the study of designing a biomaterial for hernia scaffold. After that, she worked as a research technician, focusing on developing an algae-based biodegradable plastics.

In January 2011, she enrolled in the Ph.D program of Fiber and Polymer Science at North Carolina State University in Raleigh, North Carolina. Her doctoral research, under direction of Dr. Julie A. Willoughby, focused on tailorable release of small molecules utilizing plant viral nanoparticles and fibrous matrix. After graduation, she will pursue an industrial career.

## ACKNOWLEDGMENTS

This dissertation work would never have been completed without help and support of people who are gratefully acknowledged here.

Foremost, sincere thanks to my research advisor, Dr. Julie Willoughby, for all that she has offered to me over the entire course of my study and research in the past three years. Her encouragement, great insight in the research, and substantial assistance and guidance on experimental design, presentation skills, scientific writings, and a few to name have been invaluable experience in my life.

From the Department of Textile Engineering, Chemistry and Science, I would like to give my specific thanks to Dr. Jon Rust for providing me assistantship in the first year and giving me the opportunity to start my Ph.D program. I appreciated all helps, smiles and encouragement he always gave to me. I also would like to thank Dr. Russell Gorga for being my committee member in my preliminary exam and valuable suggestions in my research work. Thank you to Birgit Andersen for training me in FITR and running XRD for my samples. I also thank Dr. Bryan Ormond for his help in HPLC. Thanks Senior Design Team, Brian Wells, Lauren Hunt, Ellery Ward, Adrian Mikol, for making and testing cellulose matrices. Thanks all helps and supports from our Willoughby Research Group: Amsarani Ramamoorthy, Kewei Xu, Nisarg Tambe.

From the Department of Plant Pathology, I would like to thank Dr. Steve Lommel and Dr. Charles Opperman for their valuable suggestions, ideas and comments in the research. Dr. Lommel provided extremely helps in my understanding of virology. Dr. Opperman helped me

in arranging and understanding the nematode assay and crop protection testing. I also want to give my thanks to Dr. Tim Sit for his insight and suggestions in my experiment design and Dick Guenther for his cooperation in the research work. I appreciated all discussions with Tim and Dick.

From the Department of Chemical Engineering, I would like to thank Dr. Saad Khan for being the co-chair of my dissertation committee. He always gave me great help when I needed. His smart opinions on research work and publication is very valuable to me. I thanks Alexander Richter for his assistance with DLS and Zeta potentials.

From the Analytical Instrumentation Facility, I want to give my thanks to Dale Batchelor and Chuck Mooney for the SEM images, Fred Stevie for the XPS analyses. I also would like to thank Kevin Wise from Department of Forest Biomaterials for use of this lab and making woodfiber matrix to my research work.

My deep appreciation goes to my lovely families for their endless love, support and confidence on me.

Finally, I would like to acknowledge the funding agencies for financially supporting the research presented in this dissertation.

## TABLE OF CONTENTS

<b>LIST OF TABLES</b> .....	ix
<b>LIST OF FIGURES</b> .....	x
<b>Chapter 1. Motivation and Overview</b> .....	1
<b>Chapter 2. Engineering the Red Clover Necrotic Mosaic Virus as the Biological Nanocarrier for Drug Delivery</b> .....	8
2.1 Biological Nanocarrier for Drug Delivery .....	8
2.2 Biology of Red clover necrotic mosaic virus .....	10
2.3 Cargo Encapsulation by Self-assembly of RCNMV .....	12
2.4 Small Molecules Loading: Creating Active Plant Viral Nanoparticles .....	14
2.5 Feasibility of Fiber Incorporation with PVNs.....	17
2.6 References .....	21
<b>Chapter 3. Loading and Release Mechanism of RCNMV Derived Plant Viral Nanoparticles for Drug delivery of Doxorubicin</b> .....	26
Abstract.....	26
3.1 Introduction .....	27
3.2 Results and Discussion.....	32
3.2.1 Electrokinetic behavior of RCNMV during PVN <sup>Dox</sup> formulation.....	32
3.2.2 Infusion of Dox into RCNMV as a function of pre-treating parameters .....	37
3.2.3 <i>In vitro</i> release of Dox from PVN <sup>Dox</sup> .....	41
3.2.4 Release kinetics and mechanism studies.....	45
3.3 Conclusions .....	48
3.4 Experimental .....	50
3.4.1 Materials .....	50
3.4.2 RCNMV propagation and purification .....	50
3.4.3 Infusion of Dox into RCNMV capsid.....	51
3.4.4 Electrokinetic and DLS measurements of RCNMV and PVN <sup>Dox</sup> .....	52
3.4.5 <i>In vitro</i> Dox release from PVN <sup>Dox</sup> .....	53
3.4.6 Statistical Analysis.....	54
3.5 References .....	54
3.6 Supporting Information.....	58
<b>Chapter 4. Development of Abamectin Loaded Plant Viral Nanoparticle for Efficacious Nematode Control</b> .....	65
Abstract.....	65
4.1 Introduction .....	69
4.2 Experimental .....	69
4.2.1 Materials .....	69

4.2.2	Infusion of Abm into RCNMV capsid.....	69
4.2.3	Physical characterization of PVN <sup>Abm</sup> .....	70
4.2.4	Quantitation of Abm in PVN <sup>Abm</sup> by HPLC.....	71
4.2.5	<i>In vitro</i> Release profiles of PVN <sup>Abm</sup> .....	72
4.2.6	Bioavailability of PVN <sup>Abm</sup> to <i>C. elegans</i> nematodes.....	73
4.2.7	Soil mobility of PVN <sup>Abm/Rho</sup> and free ABM/Rho.....	73
4.2.8	Crop protection of PVN <sup>Abm</sup> to plant parasitic nematode-infected tomato plants.....	74
4.3	Results and Discussion.....	75
4.3.1	Infusion of Abm into RCNMV and Characterization.....	75
4.3.2	Quantitation of Abm in PVN <sup>Abm</sup> by HPLC.....	76
4.3.3	<i>In vitro</i> release profiles.....	80
4.3.4	Bioavailability of PVN <sup>Abm</sup> to <i>C. elegans</i> nematode.....	82
4.3.5	Improved soil mobility of Abm by PVN carrier.....	83
4.3.6	Improved nematicide performance of Abm in soil by PVN carrier.....	84
4.4	Conclusion.....	87
4.5	References.....	88
<b>Chapter 5. Nematicide Loaded Lignocellulosic Matrices for Crop Protection.....</b>		<b>92</b>
	Abstract.....	92
5.1	Introduction.....	93
5.2	Experimental.....	96
5.2.1	Materials.....	96
5.2.2	Formation of lignocellulosic matrices and characterization.....	96
5.2.3	Chemical compositions of lignocellulosic matrix.....	97
5.2.4	Physical properties of lignocellulosic matrix.....	98
5.2.5	Loading nematicide into lignocellulosic matrices and surface characterization.....	99
5.2.6	<i>In vitro</i> released bioavailability of Abm-loaded lignocellulosic matrices to <i>C. elegans</i> nematode.....	100
5.2.7	Crop protection of Abm-loaded lignocellulosic matrices to plant parasitic nematode-infected tomato plants.....	101
5.3	Results and Discussion.....	102
5.3.1	Chemical characterization of lignocellulosic matrices by FTIR and XPS.....	102
5.3.2	Physical properties and XRD crystallinity of lignocellulosic matrices.....	107
5.3.3	Surface characterization of Abm-loaded lignocellulosic matrices.....	110
5.3.4	<i>In vitro</i> released bioassay of Abm-loaded lignocellulosic matrices.....	113
5.3.5	Crop protection of Abm-loaded lignocellulosic matrices.....	115
5.4	Conclusion.....	117
5.5	References.....	118

<b>Chapter 6. Plan Viral Nanoparticle Loaded Lignocellulosic Matrices for Active Delivery.....</b>	<b>126</b>
Abstract.....	126
6.1 Introduction.....	127
6.2 Experimental.....	128
6.2.1 Materials.....	128
6.2.2 Non-chemical incorporation of PVN and lignocellulosic matrices.....	128
6.2.3 Characterization of PVN-loaded lignocellulose matrices.....	129
6.2.4 <i>In vitro</i> release profiles of PVN <sup>Rho</sup> -loaded lignocellulosic matrices.....	130
6.2.5 Bioavailability of PVN <sup>Abm</sup> -loaded lignocellulosic matrices.....	130
6.3 Results and Discussion.....	131
6.3.1 Characterization of PVN-loaded lignocellulosic matrices by contact angle, SEM and EDS.....	131
6.3.2 Release behaviour of PVN from supporting nonwoven matrices.....	137
6.3.3 Bioavailability of PVN <sup>Abm</sup> to <i>C. elegans</i> nematode.....	138
6.3.4 Crop protection of PVN <sup>Abm</sup> -loaded lignocellulosic matrices.....	140
6.4 Conclusion.....	141
6.5 Reference.....	142
<b>Chapter 7. Summary and Outlook.....</b>	<b>143</b>
7.1 Summary.....	143
7.2 Recommendations for Future Work.....	146
7.2.1 Chemical conjugation of loading cargo into interior capsid of PVN.....	146
7.2.2 Additional fibrous materials for PVN incorporation.....	148
7.2.3 Chemical Conjugation of PVNs into polymeric matrices.....	150
1) <i>NHS/EDC Reaction of PVN-(NH<sub>2</sub>)<sub>x</sub> and Polymeric Matrix.</i> .....	151
2) <i>Thiol-maleimide Reaction of PVN-(SH)<sub>x</sub> and Polymeric Matrix.</i> .....	152
7.3 Reference.....	153

## LIST OF TABLES

<b>Table 2.1</b> Number of loading molecules released per RCNMV capsid after EDTA treatment at pH 10 and pH 8. ....	16
<b>Table 3.1</b> Loading properties of PVN <sup>Dox</sup> suspensions formulated at pH 7.5 in different buffer systems and EDTA concentrations. ....	39
<b>Table 3.2</b> Dox release rate, $k_H$ ( $h^{-1/2}$ ) and coefficient of Determination, $R^2$ , from fitting <i>in vitro</i> Dox release data to the Higuchi equation.....	46
<b>Table 3.3</b> Electrophoretic mobility and hydrodynamic diameter for PVN <sup>Dox</sup> in different buffer systems and pH before and after release of Dox. PVN <sup>Dox</sup> was formulated in Tris buffer at pH 7.5 with 20 mM EDTA.....	47
<b>Table 4.1</b> Loading properties of PVN <sup>Abm</sup> suspensions formulated at phosphate buffer pH 7.5 with different EDTA concentrations. ....	79
<b>Table 4.2</b> Crop protection results of Abm and PVN <sup>Abm</sup> to tomato seedlings infected with <i>Meloidogyne hapla</i> root knot nematode (RKN) in greenhouse. ....	87
<b>Table 5.1</b> Chemical composition analysis for abaca, banana, softwood and softwood-hardwood lignocellulosic matrices via I. Fourier transfer infrared spectroscopy (FTIR) and II. X-ray spectroscopy (XPS). ....	104
<b>Table 5.2</b> Chemical and physical properties of different lignocellulosic matrices .....	108
<b>Table 5.3</b> Advancing contact angle ( $\theta_{adv}$ ), receding contact angle ( $\theta_{rec}$ ) and contact hysteresis ( $CAH$ ) tested via a modified Wilhelmy plate method for untreated and Abm-loaded lignocellulosic matrices.....	113
<b>Table 5.4</b> Crop protection results of free Abm and Abm-loaded lignocellulosic matrices to tomato plants infected with <i>Meloidogyne hapla</i> nematode in greenhouse. ....	116
<b>Table 6.1</b> Mortality of <i>C. elegans</i> nematodes dosed at lethal concentration with free Abm and PVN <sup>Abm</sup> in the suspension or loaded on the lignocellulose matrices via physisorption.....	139
<b>Table 6.2</b> Crop protection results of PVN <sup>Abm</sup> and PVN <sup>Abm</sup> -loaded lignocellulosic matrices to tomato plants infected with <i>Meloidogyne hapla</i> nematode in greenhouse. ....	140

## LIST OF FIGURES

<p><b>Figure 2.1</b> <i>Red clover necrotic mosaic virus</i> (RCNMV). (A) Symptoms of <i>Nicotiana clevelandii</i> inoculated with RCNMV; (B) Structure of RCNMV observed by transmission electron microscopy; (C) 3D reconstructions of RCNMV at a resolution of 8.5Å. ....</p>	11
<p><b>Figure 2.2</b> RCNMV structure determined by cryo-EM reconstruction dynamic transitions of RCNMV. Units of 3 CP subunits rotate to open a pore that can be used for release of drugs. Left panel are images of the virion and a trimer of CPs in the closed confirmation and the right panel when divalent cation removed clearly show in a pore at the center of the CP trimer. ....</p>	12
<p><b>Figure 2.3</b> Schematic of nanoparticles encapsulated by RCNMV capsid proteins. (A) Conjugation of nanoparticle with RNA-2 analog; (B) Full-length RNA-1 hybridizes with RNA-2 analog to form an artificial OAS; (C) The artificial OAS orientates the assembly of capsid proteins; (D) Formation of virus-like particle (VLP) with the encapsulated nanoparticle. ....</p>	14
<p><b>Figure 2.4</b> Schematic of depletion and re-addition of divalent ions to infuse small molecules into RCNMV capsid. ....</p>	15
<p><b>Figure 2.5</b> Schematic of processes for incorporating PVN in nanofiber matrices. In the direct processing method (I), the PVN<sup>active</sup> are electrospun in situ with the polymer solution. In the immersion process (II), the nanofiber matrices are dipped into a specific volume and concentration of PVN<sup>active</sup> particles.<sup>[44]</sup> ....</p>	17
<p><b>Figure 2.6</b> Cumulative doxorubicin release over time of PLA nanofiber matrices combined with PVN<sup>dox</sup> (■) or free doxorubicin (□) where PLA was combined with the active a) post mat fabrication (dipping method) and b) prior to electrospinning (co-spinning method) and of 70:30 PLA:PEO nanofiber matrices with PVN<sup>dox</sup> (●) or free doxorubicin (○) where PLA:PEO was combined with the active c) post mat fabrication (dipping method) and d) prior to electrospinning (co-spinning method). ....</p>	19
<p><b>Figure 3.1</b> Illustration of our hypothesis for slow and fast release of doxorubicin from plant viral nanoparticles (PVN) as dictated by loading formulation; a) the combination of phosphate buffer and chelating agent (EDTA) at pH 7.4 will result in negative phosphate ions competing with the negatively charged protein residues of the virion to bind with Dox (+), potentially resulting in PVN<sup>Dox</sup> with high level of surface bound Dox, whereas b) when Tris buffer replaces phosphate buffer in the same loading formulation, the positive (CH<sub>2</sub>OH)<sub>3</sub>CNH<sub>3</sub>(+) ions will repel Dox (+) to reduce surface binding on the virion, thereby facilitating the infusion of Dox into the interior capsid to form PVN<sup>Dox</sup> with low surface bound Dox. ....</p>	31

<b>Figure 3.2</b> Illustration of the hydrodynamic flow in electrophoretic analysis if RCNMV is in a) the pore-closed position that results in a semi-permeable virus particle disrupting the current streamlines whereas in b) the pore-open condition results in a fully permeable virus particle where the current streamlines are essentially parallel through the particle. Electrostatic interactions between the viral capsid and Dox during cargo infusion are controlled by 1) buffer system, 2) buffer pH and 3) concentration of chelating agent (EDTA).....	35
<b>Figure 3.3</b> Cumulative Dox release in sodium acetate buffer at pH 5.2 for a) free Dox (★), b) PVN <sup>Dox</sup> formulated in phosphate buffer pH 7.5 with EDTA concentration at 0 mM (■), 5 mM (▲), and 20 mM (●), and c) PVN <sup>Dox</sup> formulated in Tris buffer pH 7.5 with EDTA concentrations at 5 mM (Δ) and 20 mM (○). The Tris formulation at 0 mM EDTA had negligible Dox release due to minimal Dox loading amount in PVN <sup>Dox</sup> (data not shown). The lines are guides for the eye. ....	42
<b>Figure 3.4</b> pH- and ion- responsive Dox release from PVN <sup>Dox</sup> formulated at pH 7.5 with 20mM EDTA in either a) phosphate buffer (closed symbols) or b) Tris buffer (open symbols). The pH for release buffer was 5.2 (●,○), 7.4 (■,□), and 9.0 (★, ☆). For pH 7.4, 20 mM EDTA (▲, Δ) was added to accelerate the Dox release by pore formation.....	44
<b>Figure 3.5S</b> Native RCNMV a) electrophoretic mobility and b) hydrodynamic diameter as a function of buffer pH.....	58
<b>Figure 3.6S</b> Characterization via a) transmission electron microscopy for native RCNMV, PVN <sup>Dox</sup> in sodium acetate buffer pH 5.2, and PVN <sup>Dox</sup> after release of Dox in PBS pH 7.4; b) UV/Visible absorption and fluorescence spectra for RCNMV (0.25 mg ml <sup>-1</sup> ), PVN <sup>Dox</sup> (0.5 mg ml <sup>-1</sup> ), and free Dox at equivalent concentrated of 34 μg ml <sup>-1</sup> .....	61
<b>Figure 3.7S</b> Higuchi plots of Dox cumulative release ( $M_t/M_\infty$ ) against square root hour ( $h^{1/2}$ ) for PVN <sup>Dox</sup> formulated at pH 7.5 with 20 mM EDTA in either a) phosphate buffer (closed symbols) or b) Tris buffer (open symbols). The pH for release buffer was 5.2 (●,○), 7.4 (■,□), and 9.0 (★, ☆). For pH 7.4, 20 mM EDTA (▲, Δ) was added to accelerate the release rate by pore formation.....	63
<b>Figure 4.1</b> Characterization of native RCNMV and corresponding plant viral nanoparticle via transmission electron microscopy for a) RCNMV prior to loading, b) after loading with Abm (PVN <sup>Abm</sup> ); Size distribution as measured by dynamic light scattering for hydrodynamic diameter ( $d_H$ ) and polydispersity index (PDI) of c) RCNMV and d) PVN <sup>Abm</sup> . * All RCNMV and PVN <sup>Abm</sup> were measured in sodium acetate buffer pH 5.2.....	76

<b>Figure 4.2</b> Structures of abamectin (mixture of $\geq 80\%$ B <sub>1a</sub> homolog and $\leq 20\%$ B <sub>1b</sub> homolog) and its fluorescent derivatives .....	77
<b>Figure 4.3</b> HPLC assay for quantitation of Abm in PVN <sup>Abm</sup> . HPLC chromatograms of a) standard Abm solution at concentration of 40 $\mu\text{g/ml}$ , b) PVN <sup>Abm</sup> and c) native RCNMV via fluorescence detector at excitation wavelength of 365 nm and emission wavelength of 470 nm; d) HPLC calibration curve based on the standard concentrations versus the peak area around the elution time of 3.8 minutes. ....	78
<b>Figure 4.4</b> Cumulative Abm release over time for a) free Abm dialyzed in acetate buffer pH 5.2 (★) and b) PVN <sup>Abm</sup> dialyzed in acetate buffer pH 5.2 (▲) and M9 buffer pH 7.4 (■) .....	81
<b>Figure 4.5</b> Agarose gel electrophoresis of native RCNMV, PVN <sup>Abm</sup> , and released PVN <sup>Abm</sup> in M9 buffer pH 7.4 after different times of release. Gel were visualized under UV light after ethidium bromide staining. ....	82
<b>Figure 4.6</b> Characterization of soil mobility for a) Abm/Rho mixture and b) PVN <sup>Abm/Rho</sup> and in the potting soil and sandy loam soil via the fluorescence intensity of Rho molecules and the bioavailability of Abm molecules to cause <i>C. elegans</i> nematodes to be mobilized (■), impaired (■) and immobilized (■). ....	84
<b>Figure 4.7</b> Evaluation of root system for a) uninfected tomato seedling; b) <i>Meloidogyne hapla</i> root knot nematode (RKN) infected tomato seedling; c) RKN-infected tomato seedlings treated with free Abm and d) RKN-infected tomato seedling treated with PVN <sup>Abm</sup> . All plants were growth in greenhouse for 5-weeks after treatment. ....	86
<b>Figure 5.1</b> Fourier transfer infrared spectroscopy (FTIR) analysis for abaca, banana, softwood and softwood-hardwood lignocellulosic matrices. FITR spectra of all matrices showed the peak patterns in the fingerprint region between 2000 $\text{cm}^{-1}$ and 700 $\text{cm}^{-1}$ , where the region of 1690 – 1550 $\text{cm}^{-1}$ is related to aromatic skeletal vibration from lignin component and the region of 1090 – 922 $\text{cm}^{-1}$ is related to C-O stretching from cellulose and hemicellulose content. ....	103
<b>Figure 5.2</b> X-ray spectroscopy (XPS) of a. low resolution survey scan and b. high resolution scan of carbon signal (C <sub>1s</sub> ) for abaca, banana, softwood and softwood-hardwood lignocellulosic matrices. Only O <sub>1s</sub> and O <sub>1s</sub> peaks were detected in XPS survey spectra for all matrices. C <sub>1s</sub> of all matrix can be resolved into three peaks: C <sub>1</sub> at binding energy (BE) of 285.0 eV, C <sub>2</sub> at BE of 286.5 eV and C <sub>3</sub> at BE of 288.1 eV .....	106
<b>Figure 5.3</b> X-ray diffraction (XRD) for abaca, gampi, banana, softwood and softwood-hardwood lignocellulosic matrices. All matrices showed the similar XRD	

diffractogram where a peak at  $23^\circ$  refers to crystalline plane (002) in matrices and a broad peak at  $\sim 16^\circ$  refers to the amorphous regions of matrices.....110

**Figure 5.4** Dynamic contact angle goniometer measurements for banana fiber and Abm-loaded banana fiber matrices. The loading concentration of Abm on the matrix was  $32.5 \text{ ug m}^{-2}$ . The measurement for abaca, gampi, softwood, softwood/hardwood fiber matrices were negligible due to immediate drop absorption. The insert show photographs of water droplet on a) untreated banana matrix and b) Abm-loaded banana matrix.....111

**Figure 5.5** *In vitro* bioassay to determine the mortality of *C. elegans* nematodes via a) time-dependent release and b) cycle-dependent release from Abm-loaded abaca (★), banana (●), softwood (■), and softwood/hardwood (▲) lignocellulosic matrices. The loading concentration of Abm on the matrix was  $32.5 \text{ ug m}^{-2}$ .....114

**Figure 6.1** Contact angle goniometer measurement for a) banana lignocellulosic matrix before and after loading with  $\text{PVN}^{\text{Abm}}$  at the concentration of  $0.3 \text{ mg cm}^{-2}$ ; b) softwood lignocellulosic matrix after loading with  $\text{PVN}^{\text{Abm}}$  at the concentration of  $0.6 \text{ mg cm}^{-2}$ . The measurement for softwood matrix before loading were negligible due to immediate drop absorption. The insert show photographs of water droplet on banana matrix i) before loading and ii) after  $\text{PVN}^{\text{Abm}}$  loading; and iii) softwood matrix after  $\text{PVN}^{\text{Abm}}$  loading at the contact time of zero.....133

**Figure 6.2** Field emission scanning electron microscope (FE-SEM) micrographs of a) and b) untreated banana lignocellulosic matrix at magnification of 4kX and 10kX; b) and d)  $\text{PVN}^{\text{Abm}}$  – loaded banana lignocellulosic matrix at magnification of 4kX and 10kX. \* $\text{PVN}^{\text{Abm}}$  were loaded on the matrix at the concentration of  $0.3 \text{ mg cm}^{-2}$ . .....135

**Figure 6.3** Variable pressure scanning electron microscopy (SEM) micrographs and corresponding Energy dispersive X-ray spectroscopy (EDS) for a) and b) untreated banana lignocellulosic matrix; b) and d)  $\text{PVN}^{\text{Abm}}$ -loaded banana lignocellulosic matrix. \* $\text{PVN}^{\text{Abm}}$  were loaded on the matrix at the concentration of  $0.3 \text{ mg cm}^{-2}$ . .....136

**Figure 6.4** Release of a) Free Rhodamine and b)  $\text{PVN}^{\text{Rhodamine}}$  after physisorbed on different lignocellulosic matrices: abaca (★), banana (●), softwood (■) and softwood-hardwood (▲). The number represents the percent of total release for each fibrous matrix.....138

**Figure 7.1** Schematic of chemical conjugation of lysine residues of RCNMV capsid with cysteine-terminated peptide via a cross-linker of sSMCC. ....148

**Figure 7.2** Laser confocal microscope images of a) electrospun PEO matrix and b) co-electrospun PEO matrix with ethidium bromide-infused PVN ( $\text{PVN}^{\text{EtBr}}$ ); Images of

PVN<sup>EtBr</sup>-PEO and PEO electrospun matrices under c) white light and d) VU light. The fluorescence emitted from PVN<sup>EtBr</sup>-PEO matrix indicated that PVN<sup>EtBr</sup> were uniformly incorporated into PEO fibers by co-electrospinning. Both matrices were electrospun at the voltage of 12 kV, flow rate of 5ul/min and distance of 16cm. ....150

**Figure 7.3** Schematic of NHS/EDC reaction for reacting the lysines of PVN capsid with a cellulose matrix. ....151

**Figure 7.4** Schematic of thio-maleimide reaction for tethering the PVN capsid to a cellulose matrix. ....152

## Chapter 1. Motivation and Overview

Nanotechnology is maturing as a discipline with broad applications in materials as well as an increasing spectrum of applications for the life sciences. Drug formulation and drug delivery is a specific biological application that has early-on adopted nanotechnology approaches.<sup>[1]</sup> It is well known that the efficacy of nano-scale active delivery system depends upon i) stabilized active ingredients; ii) effective targeting to intended delivery sites; and iii) controlled release of the active ingredients tailored for the specific application. The first nanocarrier for drug delivery was made of amphiphilic lipids, which achieved a stable entrapment of drugs with reduced leakage.<sup>[2]</sup> The developments of controlled-release drug delivery were not demonstrated until the use of polymeric nanoparticles or combination with polymers.<sup>[3]</sup> The drug release kinetics can be precisely controlled by the polymer's physicochemical properties. These engineered nanocarriers, however, still have some limitations for efficacious drug delivery such as low loading efficiency, lack of targeted delivery, and poor ability to control the size distribution.<sup>[4]</sup> Recently, the potentials of plant viral nanoparticles (PVNs) have drawn tremendous attention for “smart” active delivery systems due to their monodisperse, well-defined robust structures to carry active ingredients, and a polyvalent ligand-display surface to bind with biological moieties for cell targeting.<sup>[5]</sup> More importantly, they are typically non-pathogenic and non-infectious in humans.<sup>[6]</sup> However, the cargo release from PVNs is dependent on their inherent structural dynamics; thereby, it offers limited material platforms for tailoring the release of active ingredients. As a result, there is a *critical need* to build the tunable release properties in a PVN-based delivery system for highly efficacious and versatile

applications. Lack of a tunable release function is an urgent problem for PVN delivery application as the release rates influence the distribution and efficacy of active ingredients for any given application.

Besides the field of medicine, the efficacious and controlled release strategy for active ingredient, such as pesticides and nutrients, is also in high demand for the agricultural market. For example, nematode infestation of cash crops will cause an excess of \$157 billion in worldwide crop damage annually; further straining global food security<sup>[7, 8]</sup>. It is estimated that the current market for nematicides is between \$700 million and \$1 billion each year worldwide<sup>[8]</sup>. An analysis of the economic impact of nematodes and growers' decision-making indicates that, given effective and safe alternatives, the nematicide market could grow to over \$3 billion annually in the near future<sup>[9]</sup>. However, relatively few measures exist for controlling nematode infestation that are regarded as environmentally friendly, cost efficient and safe. It is not unreasonable to think that the reductions in world food production attributed to nematode infestation might have a greater impact on humans than direct infection by human parasites. Achieving safe and effective nematode control is a key part of a crucial movement toward environmentally sustainable agriculture. Towards that goal, the objective of this Ph.D. dissertation is to develop a hybrid active-delivery matrix comprising PVNs and polymeric fibrous materials to enable efficacious delivery and tunable release of nematicides. *The rationale* for incorporation of PVNs into fibrous matrices is that it would allow for a combination of benefits imparted from each component and the interactions between them. The active ingredients would be protected by PVN encapsulation until reaching the delivery

site. The fibrous matrix 1) makes PVNs easy to handle, and 2) provides additional release mechanisms for improved delivery per application.

The PVN system in this study is derived from a *Red clover necrotic mosaic virus* (RCNMV), a plant virus belonging to the *Dianthovirus* genus in the *Tombusviridae* family.<sup>[10]</sup> The previous work on structural characterization and nanotechnological utilization of RCNMV is described in Chapter 2 of this Dissertation. RCNMV consists of the robust exterior protein shell and the interior genomic nucleic acids, which arranges to form a 17 nm-diameter empty space in the RCNMV capsid.<sup>[11]</sup> This inner space and its unique response to divalent cation depletion and re-addition enable RCNMV capsid to be a nano-carrier to load and protect the foreign active cargo through the pore formation mechanism. Previous studies demonstrated the successful infusion of either a positive or neutral charged small molecules into the RCNMV capsid.<sup>[12]</sup> Chapter 3 of this Dissertation further explores the infusion loading and subsequent release mechanism of RCNMV capsid using a cancer therapeutic drug, doxorubicin (Dox), as a model loading molecule. By controlling the net charge of RCNMV's outer surface and the accessibility of RCNMV's interior cavity, we demonstrate tunable release profiles of Dox-loaded PVN via manipulation of the Dox loading capacity and Dox binding locations (external surface-binding or internal capsid-encapsulation) with the RCNMV capsid. In addition, the Dox-loaded PVN remains the same structural dynamics as native RCNMV, which enables the pH- and ion- responsive release of loaded cargo in a given environment.

In Chapter 4 of this Dissertation, we translates the findings of PVN in therapeutic release of medicinal drugs to the delivery of agro-chemicals for crop protection, especially in plant

parasite nematode (PPN) control. A biological nematicide, abamectin (Abm) is encapsulated by RCNMV capsid to address tAbm's drawback of a limited zone of root protection due to its high potential to bind to soil particles preventing its mobility or distribution throughout the soil.<sup>[13]</sup> The encapsulation by the PVN carrier also could improve the Abm's stability as well as isolate the toxicity of the nematicide from the end-user. Abm-loaded PVN enables the controlled release of loaded Abm, with similar bioavailability to the nematodes as free Abm, yet the surface chemistry of the PVN carrier significantly increases the mobility of Abm within the soil. As a result, Abm-loaded PVN enhances the nematicide performance of Abm in crop protection.

Another approach to improve the Abm's efficacy in PPN control is to incorporate it into the lignocellulosic fibrous matrices, which is described in Chapter 5 of this Dissertation. Lignocellulosic materials, such as wood, grass, and agricultural and forest residues, are the most abundant renewable resources on the planet, with approximately 200 billion tons produced annually in the world.<sup>[14]</sup> Therefore, the use of lignocellulosic natural fiber instead of synthetic polymeric fiber is an environmentally and economically sound choice. This nematicide-fibrous matrix strategy is also a simple and inexpensive method, which allows for widespread distribution of crop protection agent without interfering in smallholder farming practices. Tailorable release of Abm from the supporting matrix is achieved by varying chemical compositions (cellulose, hemicellulose and lignin), surface chemistry, and physical properties of the lignocellulosic materials. The sustainable release of Abm is enabled by additional interaction between Abm molecule and lignin compounds in banana lignocellulosic matrix further enhancing the PPN control.

To make full use of the previous two approaches for PPN control, Chapter 6 of this Dissertation describes an additional tunable release function for PVN-based delivery systems by integrating the Abm loaded-PVN within the lignocellulosic matrix. This hybrid delivery system is anticipated to combine the advantages of PVNs and fibrous matrix for creating an innovative “smart” delivery system for carrying active ingredients. The PVN can be reversibly opened to load the active ingredients within its hollow core and then closed for stable delivery and subsequent triggered release. The outer surface of PVN can be programmed to recognize a specific cell surface receptor by covalently ligating binding moieties including sugars and peptides, which is considered as the future work for this dissertation. Finally, the supporting polymeric matrix will improve PVN’s stability and provide an additional release mechanism for active ingredients that can be tuned as a function of material composition, porosity and mechanical properties.

Our work on manipulating the tailorable release of small molecules by incorporating PVN and fibrous matrices always has room for continued understanding, validation and new applications. The fact that we have successfully demonstrated the potential for PVN-matrix system to be applied in continued scientific advances opens the door for continued research and collaboration across different disciplines.

## References

- [1] S.C. Hock, Y.M. Ying, C.L. Wah, A review of the current scientific and regulatory status of nanomedicines and the challenges ahead, *PDA Journal of Pharmaceutical Science and Technology*, 65 (2011) 177-195.
- [2] A.D. Bangham, M.M. Standish, J.C. Watkins, Diffusion of univalent ions across the lamellae of swollen phospholipids, *J. Mol. Biol.*, 13 (1965) 238-IN227.
- [3] R. Langer, J. Folkman, Polymers for the sustained release of proteins and other macromolecules, *Nature*, 263 (1976) 797-800.
- [4] F. Alexis, E.M. Pridgen, R. Langer, O.C. Farokhzad, Nanoparticle technologies for cancer therapy, *Handbook of experimental pharmacology*, (2010) 55-86.
- [5] Y. Ren, S. Wong, L. Lim, Application of Plant Viruses as Nano Drug Delivery Systems, *Pharmaceutical research*, 27 (2010) 2509-2513.
- [6] P. Singh, M.J. Gonzalez, M. Manchester, Viruses and their uses in nanotechnology, *Drug Development Research*, 67 (2006) 23-41.
- [7] P. Abad, J. Gouzy, J. Aury, P. Castagnone-Sereno, E. Danchin, E. Deleury, L. Perfus-Barbeoch, V. Anthouard, F. Artiguenave, V. Blok, M. Caillaud, P. Coutinho, C. Dasilva, F. De Luca, F. Deau, M. Esquibet, T. Flutre, J. Goldstone, N. Hamamouch, T. Hewezi, O. Jaillon, C. Jubin, P. Leonetti, M. Magliano, T. Maier, G. Markov, P. McVeigh, G. Pesole, J. Poulain, M. Robinson-Rechavi, E. Sallet, B. Ségurens, D. Steinbach, T. Tytgat, E. Ugarte, C. van Ghelder, P. Veronico, T. Baum, M. Blaxter, T. Bleve-Zacheo, E. Davis, J. Ewbank, B. Favery, E. Grenier, B. Henrissat, J. Jones, V. Laudet, A. Maule, H. Quesneville, M. Rosso, T. Schiex, G.

Smant, J. Weissenbach, P. Wincker, Genome sequence of the metazoan plant-parasitic nematode *Meloidogyne incognita*, *Nature Biotechnology*, 26 (2008) 909-915.

[8] Global Nematicide Market: Market Analysis and Opportunities, Agriculture/Specialty Pesticides, Kline & Company 3rd Edition, (2012).

[9] World Agricultural Pesticides Markets, Freedonia, (2012) 458.

[10] Z. Xiong, S.A. Lommel, The complete nucleotide sequence and genome organization of red clover necrotic mosaic virus RNA-1, *Virology*, 171 (1989) 543-554.

[11] M.B. Sherman, R.H. Guenther, F. Tama, T.L. Sit, C.L. Brooks, A.M. Mikhailov, E.V. Orlova, T.S. Baker, S.A. Lommel, Removal of divalent cations induces structural transitions in red clover necrotic mosaic virus, revealing a potential mechanism for RNA release, *J. Virol.*, 80 (2006) 10395-10406.

[12] L. Loo, R.H. Guenther, S.A. Lommel, S. Franzen, Infusion of dye molecules into Red clover necrotic mosaic virus, *Chem Commun (Camb)*, (2008) 88-90.

[13] A.C. Chukwudebe, W.F. Feely, T.J. Burnett, L.S. Crouch, P.G. Wislocki, Uptake of Emamectin Benzoate Residues from Soil by Rotational Crops, *Journal of Agricultural and Food Chemistry*, 44 (1996) 4015-4021.

[14] Y.H.P. Zhang, Reviving the carbohydrate economy via multi-product lignocellulose biorefineries, *J Ind Microbiol Biotechnol*, 35 (2008) 367-375.

## Chapter 2. Engineering the Red Clover Necrotic Mosaic Virus as the Biological Nanocarrier for Drug Delivery

### 2.1 Biological Nanocarrier for Drug Delivery

Nature has created a variety of biological protein cages with diverse sizes ranged from ~10 nm to over a micron. In general, the biological nanocarrier developed for drug delivery can be bacteriophages, plant viruses or animal viruses.<sup>[1-3]</sup> These protein cages can undergo reversible conformational changes, such as swelling, disassembly, and reassembly; providing a platform to encapsulate foreign molecules within the well-defined cages. To do this, a major approach is derived from the self-assembly of the protein capsid. For instance, the protein capsid of *Hibiscus chlorotic ringspot virus* (HCRSV) was studied to package the anticancer drug, doxorubicin. The small positive-charged doxorubicin molecules were attracted by a polyprotic acid (200 kDa) to form a negatively-charged complex (PC-Dox). Then PC-Dox complex acted as a nucleus to initiate an *in vitro* assembly of HCRSV protein subunits to form an icosahedral cage encapsulating doxorubicin.<sup>[4]</sup> Using a similar approach, many other biological cages have been exploited for cargo encapsulation, which includes ferritins<sup>[5]</sup>, small heat shock protein (sHsp)<sup>[6]</sup>, *Human polyomavirus JC virus* (JCV)<sup>[7]</sup>, *Cowpea chlorotic mottle virus* (CCMV)<sup>[8]</sup>, MS2 bacteriophage<sup>[9]</sup>, to name a few. In addition, CCMV capsid demonstrated another approach for cargo encapsulation based on reversible pore opening (~2 nm) triggered by a change in pH. At a pH greater than 6.5, the precursor ions of tungstate ( $WO_4^{2-}$ ) were infused into CCMV capsid through its open pores. Upon lowering the pH of the

virus solution to 5.0, the ions crystallized to form a large ammonium salt ( $\text{H}_2\text{W}_{12}\text{O}_{42}^{10-}$ ) within the capsid. At this point, the protein cage was reversed to a closed non-swollen conformation.<sup>[10]</sup>

Targeted delivery is a critical factor for efficient drug delivery that could lower the drug dosage and reduce toxicity to nonspecific tissues. Mammalian virus-derived nanocarriers have inherent targeting to human cells, which would compete with plant viruses or bacteriophages of engineered targeting peptides for specific delivery.<sup>[11]</sup> The development of plant virus- or bacteriophage- derived nanocarriers has gained more attention recently due to their simple production, easy *in vitro* assembly, and more importantly, do not demonstrate pathogenic or infectious properties to humans. The external surface of protein capsid consists of different repetitive functional groups such as glutamate, aspartate, arginine, cysteine or lysine. These functional groups offer the binding sites for a wide range of chemical and biological moieties; addressable carbocylates<sup>[12]</sup>, thiols<sup>[13]</sup>, antibodies<sup>[14]</sup>, and receptor-binding peptides<sup>[15]</sup> are present on biological nanocarrier for specific cellular targets. Besides chemical derivation, genetic mutations were also studied to allow direct expression of receptor-binding domains or sequences on the capsid.<sup>[16, 17]</sup> After specific targeting, the controlled release of encapsulated cargo was mainly reported by capsid disassembly upon an ion or pH transition. In contrast, the synthetic nanocarriers demonstrate more approaches to control molecule release through changes in physiological environment such as temperature<sup>[18]</sup>, pH<sup>[19]</sup>, reductive or oxidative state<sup>[20, 21]</sup>, or via an enzymatic activity<sup>[22]</sup>. Hence, exploiting more methods to trigger the cargo release from biological nanocarrier such as manipulating capsid structural dynamics or complementary tailored release by composite materials enhances their overall functionality.

In this Ph.D. dissertation, we will develop an active ingredient-loaded plant viral nanoparticles (PVNs) derived from *Red clover necrotic mosaic virus* (RCNMV). The RCNMV capsid has evolved to package and protect the viral genome against the harsh environment in soils, demonstrating a robust structure for cargo encapsulation. This virus is equipped with a natural pH and ion sensor that enables it to open channels for RNA genome release in particular conditions of the cytosol. This sensitivity of RCNMV is a unique advantage for drug delivery applications. Based on this advantage, the availability of RCNMV has been explored as a promising nano-vessel for cancer targeting.<sup>[23]</sup>

## 2.2 Biology of Red clover necrotic mosaic virus

*Red clover necrotic mosaic virus* (RCNMV) is a plant virus belonging to the *Dianthovirus* genus and the family of *Tombusviridae*.<sup>[24]</sup> It is a soil-borne virus that can infect plants through the roots without a biological vector or by physical inoculation. However, it is noninfectious toward other organisms and presents no biological hazard. When infected or inoculated, the virus produces necrotic and mosaic symptoms on the infected leaves (**Figure 2.1a**). The RCNMV can be extracted from infected plants in the yield of 80 ~ 200 mg/kg of leaves via a previously published purification protocol.<sup>[25]</sup>

RCNMV is an icosahedral virus with an outer diameter of approximately 36 nm (**Figure 2.1b**). The RCNMV genome consists of two positive-sense, single-stranded RNAs: a 3.6 kb RNA-1 which encodes viral polymerase and capsid protein (CP), and a 1.5kb RNA-2 which is code for the virus movement protein.<sup>[26]</sup> One copy each of RNA-1 and RNA-2 or four copies of RNA-2 are packaged into a single protein shell comprising 180 chemically identical CP

subunits (37 kDa).<sup>[27]</sup> These CP subunits are arranged in triangulation number  $T = 3$  symmetry and form three different conformation proteins (A, B, and C). Each CP subunit is made up of

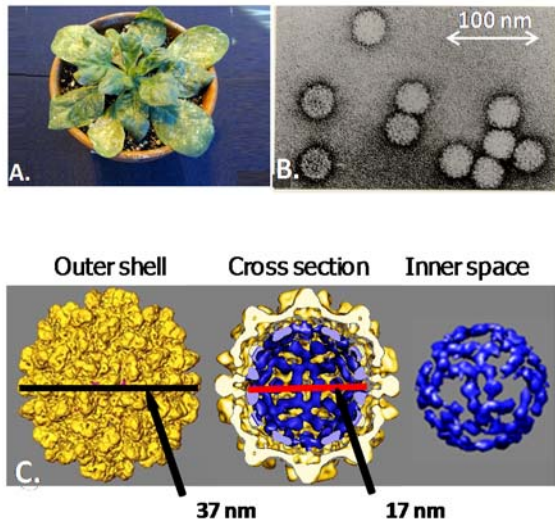


**Figure 2.1** *Red clover necrotic mosaic virus* (RCNMV). (A) Symptoms of *Nicotiana clevelandii* inoculated with RCNMV; (B) Structure of RCNMV observed by transmission electron microscopy; (C) 3D reconstructions of RCNMV at a resolution of 8.5Å.

three domains: the RNA-interacting (R), shell (S), and protruding (P) domains. The R domain contains several basic amino acids and extends inside to neutralize the RNA genome. The S and P domains constitute the outer layer of RCNMV virion, where S domains are entangled to

form the capsid shell (~3 nm) and P domains of neighboring CP subunits form 90 distinct protrusions (~3.7 nm) above the capsid shell.

Within the RCNMV capsid, the portion of genomic RNAs and amino termini of CP subunits are ordered and organized in  $T = 1$  symmetry, which produces an inner, dodecahedral cage with a diameter of 17 nm (**Figure 2.1c**).<sup>[28]</sup> This 17nm-diameter inner space provides a nanoscale space to load and protect the foreign active cargo for intended delivery.

The integrity and structure of RCNMV capsid is pH- and divalent ion-dependence. The diameter of RCNMV virion increases from 36 nm to 49 nm as the pH changes from 6.5 to 8, and its capsid shell is fully disassembled at  $\text{pH} > 9$ .<sup>[29]</sup> Divalent ions are fundamental structures

of RCNMV virion, which include  $390 \pm 30$   $\text{Ca}^{2+}$  ions located at the capsid and  $420 \pm 30$   $\text{Mg}^{2+}$  ions bound to RNA genome in the capsid interior. When RCNMV is in both low (nM)  $\text{Ca}^{2+}$  and  $\text{Mg}^{2+}$  environment, the 11-13Å diameter channels are formed on the capsid surface due to loss of divalent ions associated with virions.<sup>[28]</sup> These channels extend into the interior of the virion and allow for the release of viral RNA into the cytosol of infected cells.

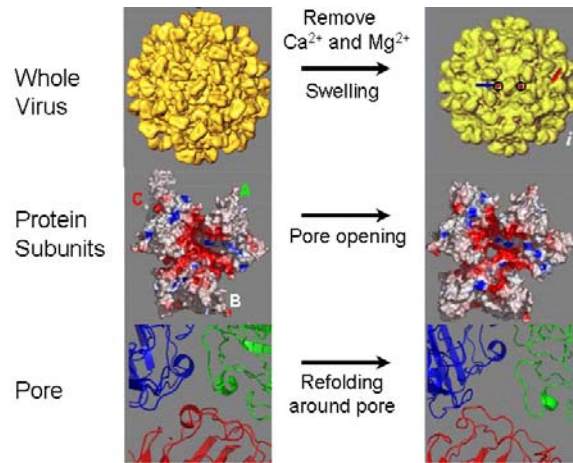


**Figure 2.2** RCNMV structure determined by cryo-EM reconstruction dynamic transitions of RCNMV.<sup>[28]</sup> Units of 3 CP subunits rotate to open a pore that can be used for release of drugs. Left panel are images of the virion and a trimer of CPs in the closed confirmation and the right panel when divalent cation removed clearly show in a pore at the center of the CP trimer.

**Figure 2.2** shows both open and closed forms. Under conditions of high (mM)  $\text{Ca}^{2+}$  and  $\text{Mg}^{2+}$ , the RCNMV capsid is in the closed form and extremely stable over a wide range of solution conditions. The open form can be induced *in vitro* by the addition of the divalent ion chelator, ethylene diamine tetraacetic acid (EDTA). *These open channels on RCNMV capsid can be used to infuse small molecules into the virion.*

### 2.3 Cargo Encapsulation by Self-assembly of RCNMV

Like other viral capsids, the self-assembly properties of RCNMV have been exploited first to package foreign cargo within its capsid. For native RCNMV, the genomic RNA1-RNA2 complex, known as the origin of assembly (OAS), can orientate the self-assembly of capsid

protein (CP) subunits to form an enclosed protein shell. Based on this mechanism, the *in vitro* assembly of RCNMV CPs has been developed for cargo encapsulations<sup>[29]</sup> **Figure 2.3** illustrates a 20-nucleotide RNA-2 analog tethered to a loading cargo that then hybridizes with a full length RNA-1 to form an artificial OAS. This foreign cargo presenting the OAS nucleates the self-assembly of CPs and ultimately creates a viral-like particle (VLP) with the encapsulated cargo. By this approach, quantum dots, gold nanoparticles and CoFe<sub>2</sub>O<sub>4</sub> nanoparticles in the diameter range of 3-15 nm have been successfully incorporated to form RCNMV VLPs. These cargo-encapsulated VLPs were homogenous in size (~32.8 nm), independent of the composition and sizes of encapsulated particles. An attempt to encapsulate particles with diameters larger than 17 nm failed to yield VLPs, which is consistent with the presence of a 17 nm cavity in the RCNMV capsid. Several small dye molecules were also proposed to package within RCNMV capsid by *in vitro* assembly, which yielded the VLPs with the diameter of ~23.7 nm.<sup>[30]</sup> However, the loading capacity for most small molecules in VLP is very low, which might be caused by lack of affinity with OAS and the smaller volume of VLP compared with native RCNMV. To solve this problem, another infusion protocol was developed for small molecules loading as presented in the following section.

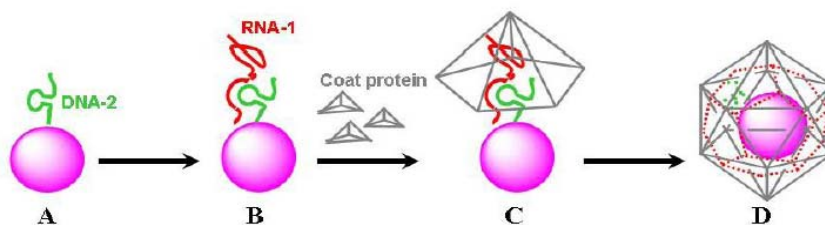


**Figure 2.3** Schematic of nanoparticles encapsulated by RCNMV capsid proteins.<sup>[29]</sup> (A) Conjugation of nanoparticle with RNA-2 analog; (B) Full-length RNA-1 hybridizes with RNA-2 analog to form an artificial OAS; (C) The artificial OAS orientates the assembly of capsid proteins; (D) Formation of virus-like particle (VLP) with the encapsulated nanoparticle.

## 2.4 Small Molecules Loading: Creating Active Plant Viral Nanoparticles

The infusion process for small molecules loading in RCNMV exploits a natural mechanism employed by the virus to release its genome upon entry into a newly infected cell. As illustrated in **Figure 2.4**,  $\text{Ca}^{2+}$  and  $\text{Mg}^{2+}$  ions associated with RCNMV are chelated by EDTA solution at pH 8, followed by exposure to a high concentration of small molecules. This treatment opens the surface pores to facilitate molecule infusion within the capsid. Encapsulation of molecules is completed when the pores are closed by re-addition of  $\text{Ca}^{2+}$  ions. The extra un-infused molecules are removed via a size exclusive column. **The resulting modified virus with loaded molecules is termed as plant viral nanoparticle (PVN).** Dynamic light scattering (DLS) and transmission electron microscopy (TEM) analysis indicated that PVN preserved similar morphology and diameter ( $\sim 34.5 \pm 3.7$ ) as the native RCNMV.<sup>[31]</sup>

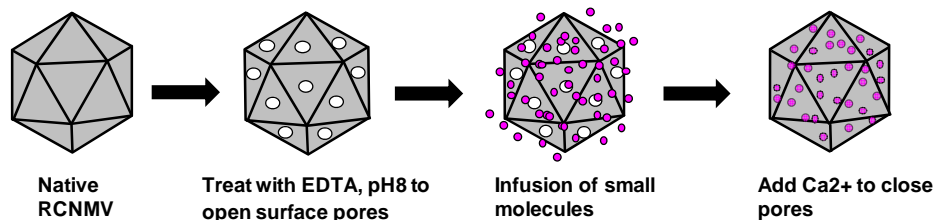


**Figure 2.4** Schematic of depletion and re-addition of divalent ions to infuse small molecules into RCNMV capsid.

Molecular infusion was tested using three dyes, rhodamine (+ charge), luminarosine (neutral), fluorescein (- charge). The results indicated that electrostatic interactions between molecules and the viral genome played a major role in the loading properties. PVNs infused with rhodamine (PVN<sup>Rho</sup>) and luminarosine (PVN<sup>Lum</sup>) have a similar loading capacity of ~79 molecules per virus, but the loading efficiency of PVN<sup>Rho</sup> is much higher than PVN<sup>Lum</sup>, which is probably due to the higher electrostatic interaction between positive rhodamine and the viral genome. Conversely, fluorescein cannot infuse into viral capsid due to the electrostatic repulsion between its negative charge and anionic viral genome. Additionally, an effective anticancer drug, doxorubicin, it is presumed that it will intercalate into the duplexed portions of the genomic RNA of RCNMV. Its strong binding affinity with the capsid yielded PVN<sup>Dox</sup> with a high loading capacity of ~1000 molecules/virus. *However, there is no evidence demonstrating that all loaded molecules were encapsulated in the PVN rather than conjugated on the surface.* With the aims of this proposal we seek to differentiate the level of molecules on the PVN surface versus the inside of the capsid. At the end of the proposed work, we expect to elucidate the mechanism of the binding kinetics for these two capsid locations for model compounds. Ideally, we anticipate we will be able to appropriately characterize the affinity

behavior of a given small molecule to predict its expected release profile once loaded into the capsid.

Formulated PVNs undergo a structural transition in response to changes in pH and divalent-ion concentration similar to the native RCNMV. Loo et al. demonstrated that this trait enables controllable cargo release upon the re-open of pores on PVNs by adding an EDTA chelating agent and a change in pH from 5.5 to 8. As a result, there was a 10% release of loaded rhodamine and luminarosin, but negligible release for doxorubicin when exposed to EDTA at pH 8 (**Table 2.1**).<sup>[31]</sup> In their experiment, the loaded PVNs were treated by an EDTA, pH8 solution with a volume ratio of 1:1, which could not induce a significant chemical potential for loading molecules to diffuse out of viral capsid, especially for doxorobucin due to its high affinity with genomic RNA. The total release of loading molecules was demonstrated by disassembly of PVNs upon raising the EDTA solution to pH 10 (**Table 2.1**). To fully manipulate the release behavior of PVNs for intended delivery, *one specific aim* of this proposal is to systematically study the controlled release of molecules from PVNs encompassing the two known triggers that create capsid structural transitions: solution pH and concentration of divalent ions.

**Table 2.1** Number of loading molecules released per RCNMV capsid after EDTA treatment at pH 10 and pH 8.<sup>[31]</sup>

Dye	Charge	Initial Load at pH 5	EDTA pH 8 <sup>a</sup>	EDTA pH 10 <sup>b</sup>
Rhodamine	+	83 ± 10	6 ± 4	83 ± 10
Luminarosine	n/a	76 ± 5	7 ± 3	76 ± 5
Doxorubicin	+	4300 ± 1300	<1	4300 ± 1300

<sup>a</sup>)Surface pores reopened (without virus disruption) to diffuse molecules from the capsid.<sup>b</sup>)Virus disassembled to release infused molecules.

## 2.5 Feasibility of Fiber Incorporation with PVNs

Recent research has shown the successful incorporation of doxorubicin-loaded PVNs (PVN<sup>Dox</sup>) into electrospun fiber matrix via two approaches: 1) direct processing by co-spinning and 2) post physisorption by immersion of the matrix into the PVN solutions (see **Figure 2.5**).<sup>[32]</sup> A nanofiber matrix with

PVN<sup>Dox</sup> was hypothesized to have both the triggered release profile imparted from the PVN and controlled release properties by the polymeric fibrous matrix. To determine the impact of polymer chemistry on the release kinetics of Dox, the study evaluated a hydrophobic polymer (poly(lactic acid) (PLA)) and a more hydrophilic polymer system (poly(lactic acid) (PLA) mixed with

poly(ethylene oxide) (PLA:PEO). As can be shown in **Figure 2.6**, therapeutic release of Dox from PVN functionalized matrix was dictated by material composition and incorporation methods. PLA matrices had a slightly lower release profile than the PLA:PEO matrices, which was likely attributed to the more hydrophilic nature of PEO as compared to PLA. Both of the co-spun matrices (**Figure 2.6b,d**) had significantly lower release profiles as compared to their

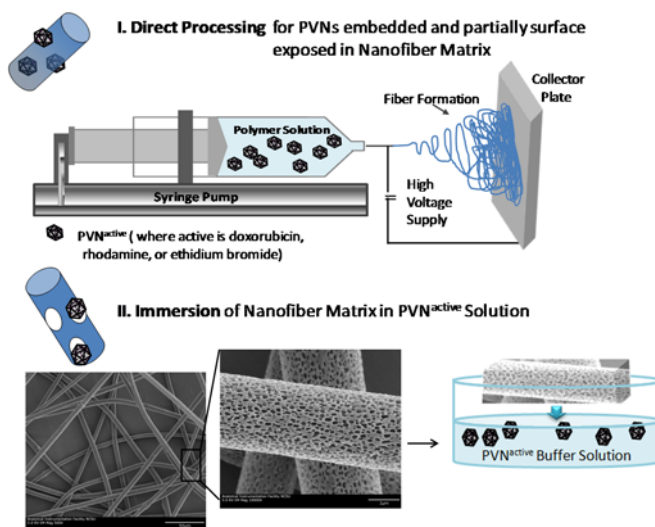


**Figure 2.5** Schematic of processes for incorporating PVN in nanofiber matrices. In the direct processing method (I), the PVN<sup>active</sup> are electrospun in situ with the polymer solution. In the immersion process (II), the nanofiber matrices are dipped into a specific volume and concentration of PVN<sup>active</sup> particles.<sup>[32]</sup>

physisorbed sample counterparts (**Figure 2.6a,c**) regardless of the molecule loaded, PVN<sup>Dox</sup> or free Dox. In all cases, near-equilibrium in Dox concentration between the release media and the nanofiber matrix was reached within about 1 day after immersing into fresh PBS. The greatest release amount of Dox was for the physisorbed PLA:PEO\_Dox specimens where 98% of the initial load was recovered. In addition, there was a large disparity in cumulative release between the physisorbed PLA:PEO matrices for PVN<sup>Dox</sup> versus free Dox ( $\Delta$  % release equal to 64%). This large difference between active ingredients was not realized for the more hydrophobic PLA matrices where 68% of Dox was released for free Dox and 40% release for PVN<sup>Dox</sup>.

The release from the PVN and a polymer matrix was expected to have a 2-phase profile; 1) the drug is released from the virus and 2) diffuses through a polymer matrix. In this study, a single phase release for the immersed samples, the release from the viral nanoparticles themselves, was determined as the viral nanoparticles were lodged into the cavities of the porous fibers. As mentioned previously, the triggered release of PVN encapsulated molecules comes from a change in environmental Ca<sup>2+</sup> and Mg<sup>2+</sup> concentrations and pH value where all the pores are expected to be open for drug release. In the experiments for the data in **Figure 2.6**, all known stimuli-factors were held constant at a physiologically relevant pH (7.2). At this pH, it is suspected the ion pairs on the capsid surface are disrupted allowing for nanoparticle swelling which facilitates diffusion of the loaded active. However, such release behavior of loaded Dox from PVN-fiber matrix is not clearly understood in the study. The free Dox in the polymer matrix and PVN<sup>Dox</sup> in polymer matrix were all fitted into the pseudo-first order kinetic release mechanism ( $R^2 > 0.97$ ). Therefore, with the objective of fabricating an effective hybrid

PVN matrix delivery system, *another specific aim* in this proposal is to elucidate the release mechanism of small molecules from active fiber matrix as a function of material interaction with loaded PVNs.

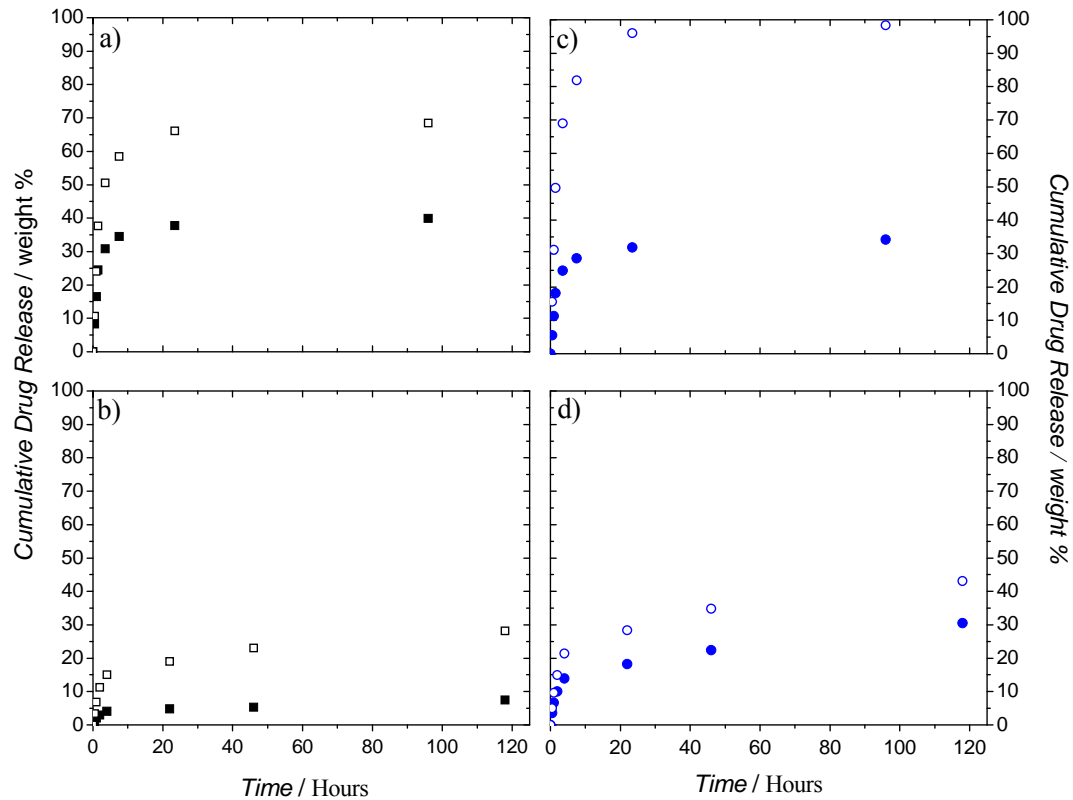


**Figure 2.6** Cumulative doxorubicin release over time of PLA nanofiber matrices combined with PVN<sup>dox</sup> (■) or free doxorubicin (□) where PLA was combined with the active a) post mat fabrication (dipping method) and b) prior to electrospinning (co-spinning method) and of 70:30 PLA:PEO nanofiber matrices with PVN<sup>dox</sup> (●) or free doxorubicin (○) where PLA:PEO was combined with the active c) post mat fabrication (dipping method) and d) prior to electrospinning (co-spinning method).<sup>[32]</sup>

Chemical conjugation of viral capsid onto solid substrate demonstrates another method for PVN-polymeric matrix incorporation. This is contributed to the reactive amino acid residues on the external surface of viral capsid, such as lysine, cysteine and glutamate. These

functional groups are well studied and used to bioconjugate coupling with chemical and biological moieties for specific cellular targets.<sup>[33]</sup> However, most recently, an emerging interest is to employ these functional groups to chemically tether viral capsids on the substrate because the nanoscale topographical features of viral capsids have great potential in applications of electronics, sensing and biomedicine. For example, bacteriophage M13 capsids were grafted onto a film with glutaraldehyde coupling reagent for cell regeneration.<sup>[34]</sup> Genetic modified cysteine-present CPMV and *tobacco mosaic virus* (TMV) were chemoselective assembled on the substrate via a thiol-maleimide reaction<sup>[35-37]</sup>. In this proposal, to expand the applications of our hybrid PVN-matrix system, *one specific aim* is to chemically conjugate cargo-loaded RCNMV PVNs onto a polymeric matrix, and more importantly to define its influence with respect to tunable release profiles of loading cargo. The exterior surface of RCNMV capsid presents both lysine and cysteine amino acid residues that are amenable to be functionalized. The previous study illustrated that surface lysines of PVN<sup>Dox</sup> were conjugated with the cysteine terminated CD46 targeting peptides via a coupling reagent of succinimidyl-4-(N-maleimidomethyl) cyclohexane-1-carboxylate (SMCC).<sup>[38, 39]</sup> Moreover, the results indicated that although PVN<sup>Dox</sup>-CD46 shown higher cytotoxicity as compared to non-labeled PVN<sup>Dox</sup> and free doxorubicin drugs, its cytotoxicity behavior was not nearly as well defined as in a typical dose response curve.<sup>[38]</sup> We speculate that this phenomenon is related to tailored release mechanism of PVN<sup>Dox</sup> after chemical modification. To clarify it, the results of the proposed work are expected to answer the following questions:

- What is the active ingredient release mechanism of small molecules from PVNs?

- Can we further manipulate the release through material interactions of PVN capsids with a polymer matrix?
- How does the loading efficiency and release differ when PVN is manipulated in chemical structure via tethering or grafting onto a polymer matrix

## 2.6 References

- [1] Y. Ma, R.J.M. Nolte, J.J.L.M. Cornelissen, Virus-based nanocarriers for drug delivery, *Adv. Drug Delivery Rev.*, 64 (2012) 811-825.
- [2] C. Bergsdorf, C. Beyer, V. Umansky, M. Werr, M. Sapp, Highly efficient transport of carboxyfluorescein diacetate succinimidyl ester into COS7 cells using human papillomavirus-like particles, *FEBS Lett.*, 536 (2003) 120-124.
- [3] S. Bhattacharya, B. Mazumber, Virosomes: A Novel Strategy for Drug Delivery and Targeting, *BioPharm International* 24 (2011) pS9.
- [4] Y. Ren, S.M. Wong, L.Y. Lim, Folic Acid-Conjugated Protein Cages of a Plant Virus: A Novel Delivery Platform for Doxorubicin, *Bioconjugate Chem.*, 18 (2007) 836-843.
- [5] M. Uchida, M.L. Flenniken, M. Allen, D.A. Willits, B.E. Crowley, S. Brumfield, A.F. Willis, L. Jackiw, M. Jutila, M.J. Young, T. Douglas, Targeting of Cancer Cells with Ferrimagnetic Ferritin Cage Nanoparticles, *Journal of the American Chemical Society*, 128 (2006) 16626-16633.
- [6] M.L. Flenniken, L.O. Liepold, B.E. Crowley, D.A. Willits, M.J. Young, T. Douglas, Selective attachment and release of a chemotherapeutic agent from the interior of a protein cage architecture, *Chemical Communications*, 0 (2005) 447-449.

- [7] C. Goldmann, N. Stolte, T. Nisslein, G. Hunsmann, W. Lüke, H. Petry, Packaging of small molecules into VP1-virus-like particles of the human polyomavirus JC virus, *J. Virol. Methods*, 90 (2000) 85-90.
- [8] J.M. Johnson, D.A. Willits, M.J. Young, A. Zlotnick, Interaction with Capsid Protein Alters RNA Structure and the Pathway for In Vitro Assembly of Cowpea Chlorotic Mottle Virus, *Journal of Molecular Biology*, 335 (2004) 455-464.
- [9] C.E. Ashley, E.C. Carnes, G.K. Phillips, P.N. Durfee, M.D. Buley, C.A. Lino, D.P. Padilla, B. Phillips, M.B. Carter, C.L. Willman, C.J. Brinker, J.d.C. Caldeira, B. Chackerian, W. Wharton, D.S. Peabody, Cell-Specific Delivery of Diverse Cargos by Bacteriophage MS2 Virus-like Particles, *ACS Nano*, 5 (2011) 5729-5745.
- [10] O.L. Lars, R. Jennifer, A. Mark, O. Luke, Y. Mark, D. Trevor, Structural transitions in Cowpea chlorotic mottle virus (CCMV), *Physical Biology*, 2 (2005) S166.
- [11] R.L. Garcea, L. Gissmann, Virus-like particles as vaccines and vessels for the delivery of small molecules, *Curr. Opin. Biotechnol.*, 15 (2004) 513-517.
- [12] N.F. Steinmetz, G.P. Lomonosoff, D.J. Evans, Cowpea Mosaic Virus for Material Fabrication: Addressable Carboxylate Groups on a Programmable Nanoscaffold, *Langmuir*, 22 (2006) 3488-3490.
- [13] N.F. Steinmetz, D.J. Evans, G.P. Lomonosoff, Chemical Introduction of Reactive Thiols Into a Viral Nanoscaffold: A Method that Avoids Virus Aggregation, *ChemBioChem*, 8 (2007) 1131-1136.
- [14] K.E. Sapsford, C.M. Soto, A.S. Blum, A. Chatterji, T. Lin, J.E. Johnson, F.S. Ligler, B.R. Ratna, A cowpea mosaic virus nanoscaffold for multiplexed antibody conjugation: Application as an immunoassay tracer, *Biosensors and Bioelectronics*, 21 (2006) 1668-1673.
- [15] A. Chatterji, W. Ochoa, L. Shamieh, S.P. Salakian, S.M. Wong, G. Clinton, P. Ghosh, T. Lin, J.E. Johnson, Chemical Conjugation of Heterologous Proteins on the Surface of Cowpea Mosaic Virus, *Bioconjugate Chem.*, 15 (2004) 807-813.

- [16] G.P. Lomonossoff, J.E. Johnson, Use of macromolecular assemblies as expression systems for peptides and synthetic vaccines, *Curr. Opin. Struct. Biol.*, 6 (1996) 176-182.
- [17] Joelson T, Akerblom L, Oxelfelt P, Strandberg B, Tomenius K, M. T.J., Presentation of a foreign peptide on the surface of tomato bushy stunt virus, *J. Gen. Virol.*, 78 (1997) 1213-1217.
- [18] H. Chen, Y. Gu, Y. Hub, Z. Qian, Characterization of pH- and temperature-sensitive hydrogel nanoparticles for controlled drug release, *PDA journal of pharmaceutical science and technology / PDA*, 61 (2007) 303-313.
- [19] J.-Z. Du, X.-J. Du, C.-Q. Mao, J. Wang, Tailor-Made Dual pH-Sensitive Polymer–Doxorubicin Nanoparticles for Efficient Anticancer Drug Delivery, *Journal of the American Chemical Society*, 133 (2011) 17560-17563.
- [20] G. Saito, J.A. Swanson, K.D. Lee, Drug delivery strategy utilizing conjugation via reversible disulfide linkages: role and site of cellular reducing activities, *Advanced drug delivery reviews*, 55 (2003) 199-215.
- [21] C.D. Vo, G. Kilcher, N. Tirelli, Polymers and Sulfur: what are Organic Polysulfides Good For? Preparative Strategies and Biological Applications, *Macromolecular Rapid Communications*, 30 (2009) 299-315.
- [22] R. de la Rica, D. Aili, M.M. Stevens, Enzyme-responsive nanoparticles for drug release and diagnostics, *Advanced drug delivery reviews*, 64 (2012) 967-978.
- [23] S. Franzen, S.A. Lommel, Targeting cancer with 'smart bombs': equipping plant virus nanoparticles for a 'seek and destroy' mission, *Nanomedicine (Lond)*, 4 (2009) 575-588.
- [24] Z. Xiong, S.A. Lommel, The complete nucleotide sequence and genome organization of red clover necrotic mosaic virus RNA-1, *Virology*, 171 (1989) 543-554.
- [25] D. Lockney, S. Franzen, S. Lommel, Viruses as nanomaterials for drug delivery, *Methods Mol. Biol.*, 726 (2011) 207-221.

- [26] Z. Xiong, K.H. Kim, D. Giesman-Cookmeyer, S.A. Lommel, The roles of the red clover necrotic mosaic virus capsid and cell-to-cell movement proteins in systemic infection, *Virology*, 192 (1993) 27-32.
- [27] V.R. Basnayake, T.L. Sit, S.A. Lommel, The genomic RNA packaging scheme of Red clover necrotic mosaic virus, *Virology*, 345 (2006) 532-539.
- [28] M.B. Sherman, R.H. Guenther, F. Tama, T.L. Sit, C.L. Brooks, A.M. Mikhailov, E.V. Orlova, T.S. Baker, S.A. Lommel, Removal of divalent cations induces structural transitions in red clover necrotic mosaic virus, revealing a potential mechanism for RNA release, *J. Virol.*, 80 (2006) 10395-10406.
- [29] L. Loo, R.H. Guenther, S.A. Lommel, S. Franzen, Encapsulation of nanoparticles by red clover necrotic mosaic virus, *J. Am. Chem. Soc.*, 129 (2007) 11111-11117.
- [30] L.N. Loo, Development of Red clover necrotic mosaic virus as a Multifunctional Nanoparticle, in: Department of Chemistry, North Carolina State University, 2007, pp. 67-68.
- [31] L. Loo, R.H. Guenther, S.A. Lommel, S. Franzen, Infusion of dye molecules into Red clover necrotic mosaic virus, *Chem. Commun. (Cambridge, U. K.)*, (2008) 88-90.
- [32] S. Honarbakhsh, R.H. Guenther, J.A. Willoughby, S.A. Lommel, B. Pourdeyhimi, Polymeric Systems Incorporating Plant Viral Nanoparticles for Tailored Release of Therapeutics, *Adv. Healthcare Mater.*, (2013).
- [33] E.M. Sletten, C.R. Bertozzi, Bioorthogonal Chemistry: Fishing for Selectivity in a Sea of Functionality, *Angewandte Chemie International Edition*, 48 (2009) 6974-6998.
- [34] L. Wu, L.A. Lee, Z. Niu, S. Ghoshroy, Q. Wang, Visualizing Cell Extracellular Matrix (ECM) Deposited by Cells Cultured on Aligned Bacteriophage M13 Thin Films, *Langmuir*, 27 (2011) 9490-9496.
- [35] N.F. Steinmetz, G. Calder, G.P. Lomonosoff, D.J. Evans, Plant Viral Capsids as Nanobuilding Blocks: Construction of Arrays on Solid Supports, *Langmuir*, 22 (2006) 10032-10037.

- [36] C.L. Cheung, J.A. Camarero, B.W. Woods, T. Lin, J.E. Johnson, J.J. De Yoreo, Fabrication of Assembled Virus Nanostructures on Templates of Chemoselective Linkers Formed by Scanning Probe Nanolithography, *J. Am. Chem. Soc.*, 125 (2003) 6848-6849.
- [37] N.F. Steinmetz, K.C. Findlay, T.R. Noel, R. Parker, G.P. Lomonosoff, D.J. Evans, Layer-By-Layer Assembly of Viral Nanoparticles and Polyelectrolytes: The Film Architecture is Different for Spheres Versus Rods, *ChemBioChem*, 9 (2008) 1662-1670.
- [38] D.M. Lockney, R.N. Guenther, L. Loo, W. Overton, R. Antonelli, J. Clark, M. Hu, C. Luft, S.A. Lommel, S. Franzen, The Red clover necrotic mosaic virus capsid as a multifunctional cell targeting plant viral nanoparticle, *Bioconjug Chem*, 22 (2011) 67-73.
- [39] R. Wang, D.M. Lockney, M.B. Goshe, S. Franzen, Mass spectrometric detection of targeting peptide bioconjugation to Red clover necrotic mosaic virus, *Bioconjug Chem*, 22 (2011) 1970-1982.

### **Chapter 3. Loading and Release Mechanism of RCNMV Derived Plant Viral Nanoparticles for Drug delivery of Doxorubicin**

#### **Abstract:**

We present detailed studies on the loading and release mechanism of the *Red clover necrotic mosaic virus* (RCNMV) derived plant viral nanoparticle (PVN) for controlled delivery of the anticancer drug, doxorubicin (Dox). Previous studies demonstrated that RCNMV's structure and unique response to divalent cation depletion and re-addition enables Dox infusion to the viral capsid through a pore formation mechanism. However, by controlling the net charge of RCNMV outer surface and accessibility of RCNMV interior cavity, we show the tunable release profiles of PVN via manipulation of the Dox loading capacity and binding locations (external surface-binding or internal capsid-encapsulation) with the RCNMV capsid. This was determined with electrokinetic characterization of RCNMV as a function of pre-treating parameters during PVN formulations. Bimodal release kinetics is achieved via a rapid release of surface-Dox followed by a slow release of encapsulated Dox. Moreover, the rate of Dox release and the amount of released Dox increases with an increase in environmental pH or a decrease in concentration of divalent cations. This pH-responsive Dox release from PVN is controlled by Fickian diffusion kinetics where the release rate is dependent on the location of the bound or loaded active molecule. In summary, we describe a methodology to derive Dox-loaded PVNs with two approaches of controllable release; one is imparted by formulation

conditions and another is driven by the capsid's pH- and ion- responsive functions in a given environment.

### 3.1 Introduction

Nanotechnology is maturing as a discipline with broad applications in materials as well as an increasing spectrum of applications for the life sciences. Drug formulation and drug delivery is a specific biological application that has early-on adopted nanotechnological approaches.<sup>[1]</sup> Potential drug nanocarriers are being extensively studied representing a spectrum material platforms including liposomes,<sup>[2]</sup> dendrimers,<sup>[3]</sup> polymeric nanoparticles such as micelles,<sup>[4]</sup> hydrogels,<sup>[5]</sup> and biological nanocarriers.<sup>[6]</sup> Each of these systems has its advantages and disadvantages regarding the versatile applications and requirements for therapeutic drug delivery. For example, polymer nanoparticles can be made from an array of materials and are easily manipulated, but tend to have limited biocompatibility.<sup>[7]</sup> Dendrimers exhibit excellent bioavailability, but lack sufficient colloidal stability in solution.<sup>[8]</sup> Other issues include low loading efficiency, lack of targeted delivery and controlled release, and poor control over the size distribution of carriers.<sup>[9]</sup> For exploring an ideal therapeutic nanocarrier, biological protein cages or viral capsids have drawn great attention recently, due to their benefits of inherent self-assembly, homogenous size distribution, well-defined structures and functional binding sites.<sup>[10]</sup> More importantly, most of these biological materials are typically not human pathogens and less likely to induce acute pro-inflammatory cytokines during *in vivo* studies.<sup>[11]</sup>

Nature has created a variety of biological protein cages with diverse sizes ranging from ~ 10 nm to over a micron in diameter or length with distinctive shapes such as icosahedrons, spheres or tubes. In general, the biological nanoparticles developed for drug delivery comprise

bacteriophages, plant viruses or animal viruses.<sup>[10, 12]</sup> These protein cages can undergo reversible conformational changes, such as swelling, disassembly, and reassembly; providing a platform to encapsulate foreign molecules within the protein cages. For instance, Ren et al. demonstrated the disassembly and *in vitro* self-assembly of protein capsids from *Hibiscus chlorotic ringspot virus* and also the packaging the anticancer drug, doxorubicin (Dox), within its protein capsid.<sup>[13]</sup> Using a similar approach, many other biological cages have been successfully developed for cargo encapsulation including ferritins,<sup>[14]</sup> small heat shock protein,<sup>[15]</sup> *Cowpea chlorotic mottle virus* (CCMV),<sup>[16]</sup> MS2 bacteriophage,<sup>[17]</sup> and the E2 component of pyruvate dehydrogenase<sup>[18]</sup> to name a few. For this *in vitro* self-assembly approach, however, the small molecule encapsulation efficiency was very low. In addition, the protein subunits comprising the biological cages must be derived from a chemical derivation or genetic mutation to enable binding with loading molecules. Moreover, in case of the virus examples, the *in vitro* assembled viral capsids lack the complete genomic nucleic acids, which contribute to their poor nanocarrier stability for drug delivery.

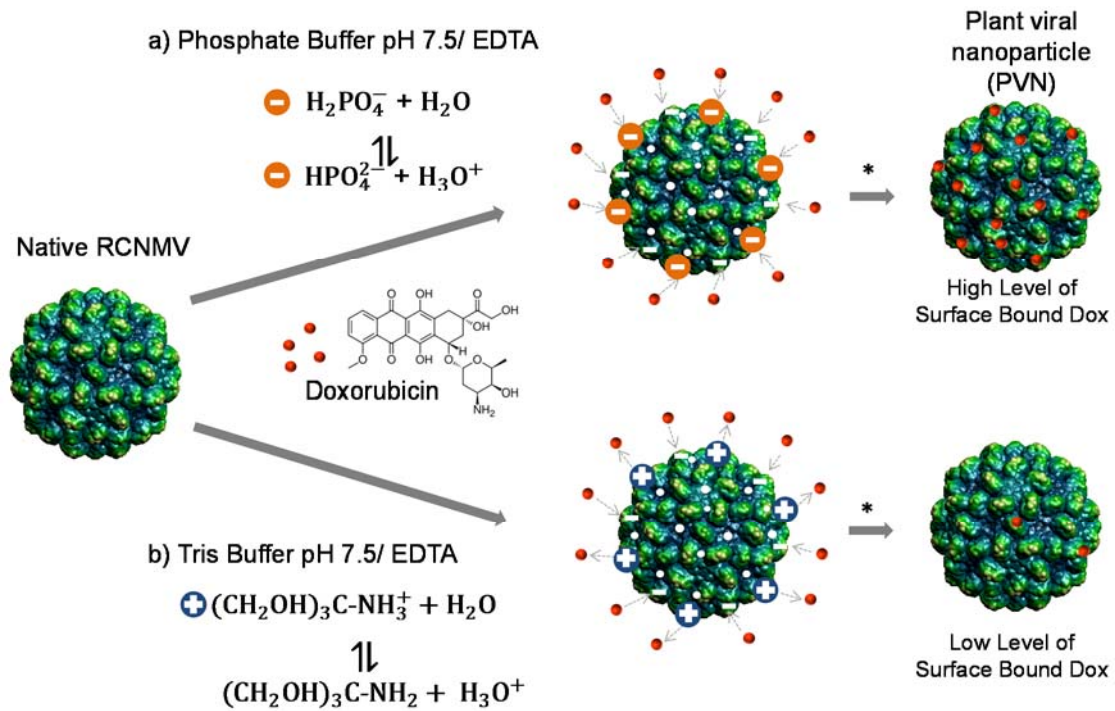
Most recently, we and others have demonstrated the infusion of small molecules into plant a virus-based nanoparticle via the reversible opening of pores in viral capsid.<sup>[19]</sup> The plant viral nanoparticle (PVN) we use in this study is derived from *Red clover necrotic mosaic virus* (RCNMV), a plant virus belonging to the *Dianthovirus* genus in the *Tombusviridae* family.<sup>[20]</sup> The RCNMV capsid measures 36 nm in diameter and comprises 180 copies of a single 38 kDa capsid protein subunit arranged in an icosahedral symmetry with a triangulation number  $T = 3$ .<sup>[20]</sup> Within the RCNMV capsid, the genomic RNAs and a portion of the amino termini of the capsid protein subunits are ordered and organized into an internal cage with a  $T = 1$

symmetry, yielding an approximate 17 nm diameter inner cavity. We posit that this inner cavity serves as a cargo-hold for loaded small molecule foreign cargo.<sup>[21]</sup> The previous study showed that the RCNMV capsid can reorient to form sixty 11-13 Å diameter pores extending through the capsid surface upon extraction of bound divalent cations.<sup>[21]</sup> These open pores extend along the quasi-threefold axis creating channels into the interior cavity of the virus. This capsid open-pore state provides a strategy for encapsulating small molecules by infusion. Our previous studies demonstrated the successful infusion of dye molecules, with either a positive or neutral charge, into the RCNMV capsid,<sup>[19a]</sup> chemical conjugation of cargo-infused RCNMV capsids with targeting peptides,<sup>[22]</sup> and incorporation of cargo-infused RCNMV capsids within nanofibrous matrices via electrospinning.<sup>[23]</sup> Other reported virus-based nanoparticles based on this infusion method include CCMV,<sup>[19b]</sup> *Cucumber mosaic virus*,<sup>[19c]</sup> and *Cowpea mosaic virus*.<sup>[19d]</sup> All of these studies assumed that the infusion of small molecules throughout the open pores would be driven by their electrostatic interaction with the negatively charged genomic nucleic acids packaged within virus; however, none of the research quantitatively measured this electrostatic interaction and/ or studied the influence of electrostatic interactions on the loading and release properties of small molecules within those virus-based protein cages.

In this study, we exploit the infusion loading and release mechanism of the RCNMV capsid using Dox as a model-loading molecule. As a weak amphipathic base with a pKa of 8.3, Dox is a positively charged molecule in physiological fluids due to protonation of its amino groups.<sup>[24]</sup> Dox also strongly intercalates into duplexed DNAs and RNAs due to the presence of flat aromatic rings in its structure.<sup>[25]</sup> Moreover, upon RCNMV capsid pore formation, the outer surface of the viral capsid surrounding these pores become predominantly negatively

charged.<sup>[21]</sup> Therefore, we hypothesized that infusion of Dox into the RCNMV follows a 2-step process where 1) Dox is attracted to the outer surface of RCNMV due to electrostatic interactions followed by 2) the formation of a RCNMV RNA-Dox intercalated complex within the RCNMV capsid. One specific aim of this study is to manipulate the RCNMV's electrostatic interaction with Dox by pre-treating RCNMV under different conditions (e.g. pH, buffer system, concentration of divalent ions) prior to loading with Dox. The change in the charge and the altered RCNMV structure dynamics in different pre-treating conditions were characterized by its electrokinetic behaviors, whose results were related to the RCNMV-Dox loading properties to understanding the loading mechanism. For instance, we found that the type of buffer used during Dox infusion alters the charge on RCNMV outer surface, which in turn dictates the loading location of Dox in or on the viral capsid. As illustrated in **Figure 3.1**, at pH 7.5 phosphate buffer (monobasic and dibasic sodium phosphates) is negatively charged whereas Tris buffer (tris(hydroxymethyl)aminomethane and hydrochloric acid) is positively charged, therefore the net charge of buffer associated-virions in suspension will be different for each buffer type. Prior to loading Dox, RCNMV in phosphate buffer would induce a higher negatively charged capsid surface (**Figure 3.1a**) as compared to RCNMV in Tris buffer (**Figure 3.1b**) at pH 7.5. This higher negatively charged capsid surface possess a higher affinity to electrostatically attract positive-charged Dox during loading, resulting in a Dox-loaded plant viral nanoparticle (PVN<sup>Dox</sup>) with a high level of surface bound Dox. In contrast, the cationic ions of Tris buffer on the capsid surface would repel Dox from the RCNMV surface to facilitate the infusion of Dox into the interior capsid. As a result, the Tris buffer limits the surface bound Dox to facilitate the formulation of PVN<sup>Dox</sup> with a high level of Dox encapsulation. To further

support our hypothesis, we determined the release mechanism of Dox from PVN<sup>Dox</sup> as the degree of Dox-RCNMV association (encapsulation or surface-bound) imparted by its formulation conditions, as well as the influence of its releasing environments (pH or ion concentration).



\* Close pores with addition of  $\text{Ca}^{2+}$  and  $\text{Mg}^{2+}$ , purify to remove excess/unbound Dox

**Figure 3.1** Illustration of our hypothesis for slow and fast release of doxorubicin from plant viral nanoparticles (PVN) as dictated by loading formulation; a) the combination of phosphate buffer and chelating agent (EDTA) at pH 7.4 will result in negative phosphate ions competing with the negatively charged protein residues of the virion to bind with Dox (+), potentially resulting in PVN<sup>Dox</sup> with high level of surface bound Dox, whereas b) when Tris buffer replaces phosphate buffer in the same loading formulation, the positive  $(\text{CH}_2\text{OH})_3\text{CNH}_3^+$  ions will repel Dox (+) to reduce surface binding on the virion, thereby facilitating the infusion of Dox into the interior capsid to form PVN<sup>Dox</sup> with low surface bound Dox. The encapsulated Dox and surface bound Dox result in slow and fast release of Dox from PVN. The Red clover necrotic mosaic virus (RCNMV) image was downloaded from <http://viperdb.scripps.edu/>.

## 3.2 Results and Discussion

### 3.2.1 Electrokinetic behavior of RCNMV during PVN<sup>Dox</sup> formulation

We have previously shown that when RCNMV was pre-treated with EDTA (ethylenediaminetetraacetic acid) to chelate divalent ions ( $Mg^{2+}$  &  $Ca^{2+}$ ) from RCNMV, a “pore-open” condition of the viral capsid was induced allowing the successful subsequent infusion of Dox molecules.<sup>[19a,21]</sup> To systematically characterize this infusion mechanism, we formulated PVN<sup>Dox</sup> in a 2-step process, where step 1 is to pre-treat RCNMV in different conditions to vary its charge and structural dynamics, and step 2 is to add Dox to allow loading/infusing into RCNMV capsid. The pre-treating parameters for RCNMV are 1) buffer pH, 2) buffer type and 3) amount of the chelating agent. The net charge of RCNMV in different pretreatment conditions was characterized via its corresponding electrokinetic behaviors. Electrophoresis, or the motion of dispersed particles under a uniform electric field, is commonly quantified for colloidal systems by a measureable parameter, electrophoretic (EP) mobility.<sup>[26]</sup> However, unlike the electrokinetic theories that are strictly valid for hard colloidal objects, viral capsids are regarded as a soft colloid comprising permeable concentric layers where the EP mobility are dependent not only on the contributed charge from each layer of the viral capsid (external capsid shell layer, inner RNA-protein bound layer or inner RNA layers), but also on the hydrodynamic flow permeation within the RNA-protein bound layer and bulk RNA layer of the virus.<sup>[27]</sup> For example, **Figure 3.2** illustrates the hydrodynamic flow around or through a soft colloid particle such as a virus when subjected to an electric field. If RCNMV is in the pore-closed condition, it is considered only semi-permeable and the current

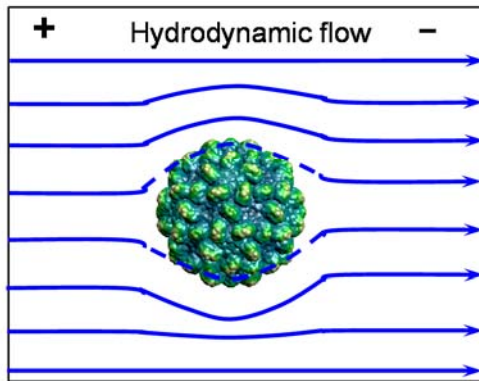
streamlines upon an approaching capsid shell are partially disrupted (**Figure 3.2a**). As a result, the EP mobility of RCNMV, referring to the velocity of a charged particle in a unit electric field, is only affected by the charge of its external protein shell.<sup>[27b]</sup> In contrast, the state of fully permeable viral capsid, where the RCNMV capsid is in pore-open condition, would allow for a continuum in the hydrodynamic flow resulting in essential parallel current streamlines through the virus core (**Figure 3.2b**). In this state, the EP mobility of RCNMV would be dictated by the net charge from the protein shell and the virus' nucleic acids, as well as the full penetration flow that induces a polarization field within and around the virus to retard its motion in the electric field.<sup>[27b]</sup> In this study, we utilized an electrokinetic technique and soft colloid theories to study the change in the net charge of the RCNMV capsid, ultimately changing the flow permeation into the viral capsid, to understand loading condition dependencies.

#### *A) Influence of buffer pH*

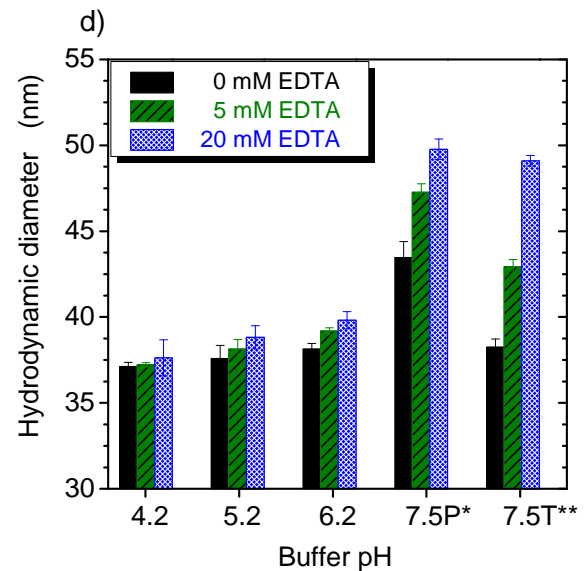
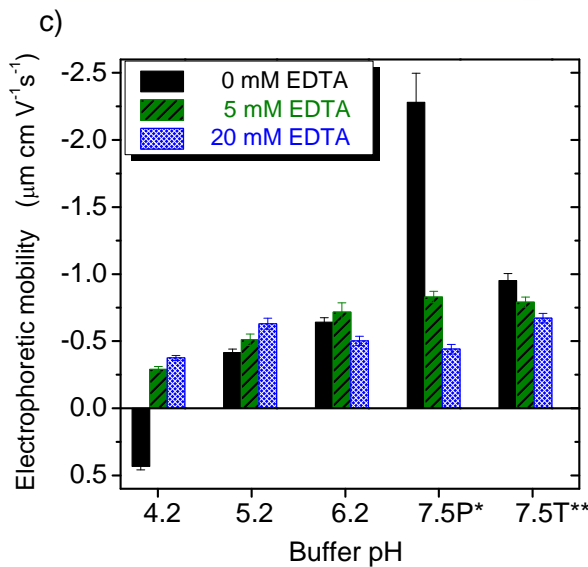
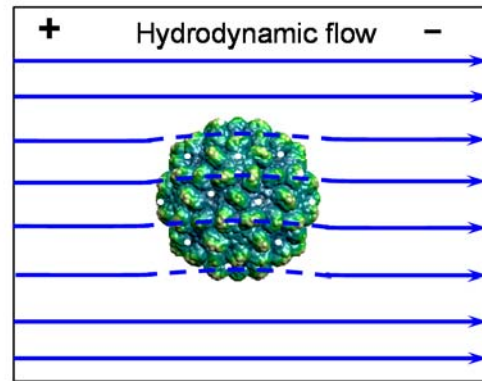
EP mobility of RCNMV measured at different pH values (pH 4.2, pH 5.2, pH 6.2, pH 7.5) and EDTA concentration (0 mM, 5 mM, 20 mM) are shown in **Figure 3.2c**. Since our previous studies confirmed that the “pore-open” condition of the viral capsid was induced only with EDTA treatment at pH 6.5,<sup>[21]</sup> we infer that RCNMV is semipermeable to hydrodynamic flow when there is no EDTA in the solution (as illustrated in **Figure 3.2a**). The results show that without EDTA chelation, EP mobility of RCNMV has a positive value in sodium acetate buffer pH 4.2, which transitioned to a more negative EP mobility value with increasing pH. This is indicative of a negatively charged protein shell resulting from the deprotonation of protein

residues on RCNMV at higher pH, as the isoelectric point of RCNMV, defined by the pH value where the net charge of the viral capsid is zero (EP mobility = 0),<sup>[28]</sup> is approximately 4.3 (See **Figure 3.5S** in supporting information). This result suggests that RCNMV can be electrostatically attracted to the positively charged Dox (pKa = 8.3) at pH > 4.3. Moreover, RCNMV demonstrated a significant increase in hydrodynamic diameter ( $d_H$ ) from  $37.1 \pm 0.2$  nm at pH 4.2 in sodium acetate buffer to  $43.5 \pm 0.9$  nm at pH 7.5 in phosphate buffer (**Figure 3.2d**); this difference is attributed to a large electrostatic repulsion between neighboring acid residues on protein shell after deprotonation as well as the thickness increase in the hydrodynamic layer of the virion in phosphate buffer.<sup>[29]</sup>

a) Semipermeable through protein capsid



b) Fully permeable through viral particle



\*Phosphate buffer system at pH 7.5

\*\*Tris buffer system at pH 7.5

**Figure 3.2** Illustration of the hydrodynamic flow in electrophoretic analysis if RCNMV is in a) the pore-closed position that results in a semi-permeable virus particle disrupting the current streamlines whereas in b) the pore-open condition results in a fully permeable virus particle where the current streamlines are essentially parallel through the particle. Electrostatic interactions between the viral capsid and Dox during cargo infusion are controlled by 1) buffer system, 2) buffer pH and 3) concentration of chelating agent (EDTA). These variables dictate RCNMV's c) electrophoretic (EP) mobility, and d) hydrodynamic diameter as a function of buffer pH (4.2, 5.2, 6.2 & 7.5), phosphate buffer or Tris buffer, and EDTA concentration (0 mM, 5 mM & 20 mM). The Red clover necrotic mosaic virus (RCNVM) image was downloaded from <http://viperd.b.scripps.edu/>.

### *B) Influence of buffer type*

EP mobility and the hydrodynamic diameter of RCNMV were further characterized in sodium phosphate and Tris buffers with the same pH (7.5) and molarity (20mM). As shown in **Figure 3.2c**, phosphate buffer induced a larger RCNMV EP mobility as compared to Tris buffer in the absence of EDTA. This indicates that when RCNMV is suspended in phosphate buffer, the RCNMV protein shell is more negatively charged. The specific ions of each buffer system seem to alter the net charge of RCNMV protein shell and correspondingly RCNMV EP mobility even through the buffers are the same pH (7.5) and ionic strength.<sup>[30]</sup> At pH 7.5, the dissociation equilibrium in phosphate buffer occurs between the anions of  $\text{H}_2\text{PO}_4^-$  and  $\text{HPO}_4^{2-}$ , whereas the dissociation equilibrium in Tris buffer occurs between cations of  $\text{Tris-NH}_3^+$  and neutral species of  $\text{Tris-NH}_2$ . It appears that the anionic phosphate buffer species associate with suspended RCNMV giving rise to a more negatively charged protein shell and therefore a greater mobility in the electric field. The electrostatic repulsions among these negatively charged residues on the RCNMV protein shell also induce the increase in hydrodynamic size of the viral capsid ( $d_H = 43.5 \pm 0.9$  nm). In contrast, the Tris buffer cations neutralize these negatively charged protein residues, which led to a less negatively charged protein shell and a stable non-swelling viral capsid ( $d_H = 38.3 \pm 0.5$  nm).

### *C) Influence of EDTA concentration*

Addition of EDTA varied the EP mobility of RCNMV at different pH values. At lower pH (4.2 and 5.2), increasing the EDTA concentration gave rise to increased RCNMV EP mobility (**Figure 3.2a**) indicating a formation of a more negatively charged RCNMV due to

EDTA chelation of divalent cations ( $\text{Ca}^{2+}$  &  $\text{Mg}^{2+}$ ) from the viral capsid. The RCNMV hydrodynamic size at pH 4.2 and 5.2 only slightly changed with the EDTA (**Figure 3.2d**) indicating a relatively stable capsid structure. However, the opposite trend was observed at higher pH 7.5 in both phosphate and Tris buffers, where the RCNMV EP mobility decreased with an increase in EDTA concentration (**Figure 3.2c**). This observation suggests a large flow permeation into the capsid interior after EDTA addition (as illustrated in **Figure 3.2b**), allowing access to the internal nucleic acids region. This access induces a polarization field within and around the RCNMV retarding its motion in the electric field.<sup>[27b]</sup> This characteristic high flow permeability indicates the formation of open-pores within the RCNMV capsid by EDTA chelation.<sup>[21]</sup> At the same time, the RCNMV capsid swelled to a hydrodynamic diameter of  $\sim 49.5$  nm after addition of 20 mM EDTA in both phosphate and Tris buffers at pH 7.5 (**Figure 3.2d**). The increased intramolecular repulsion with resultant pore formation are responsible for the structural swelling of viral particles.<sup>[29, 31]</sup>

### 3.2.2 Infusion of Dox into RCNMV as a function of pre-treating parameters

After pretreating RCNMV in different conditions as mentioned in previous section, the same amount of free Dox molecules were added to the RCNMV suspension to allow the infusion of Dox into viral capsid. We denote our samples as  $\text{B}^{\#D}\text{-PVN}^{\text{Dox}}$  where B is the buffer type (P for phosphate or T for Tris), #D is the EDTA concentration in mM. For example, a phosphate buffer formulation with 5 mM EDTA would be denoted  $\text{P}^{5D}\text{-PVN}^{\text{Dox}}$ . All formulated  $\text{PVN}^{\text{Dox}}$  were stabilized to the “pore-closed” condition by post-treatment maintenance in pH 5.2 buffer after purification to remove unbound or excess Dox prior to characterization and *in*

*vitro* release studies. The physical characterization of PVN<sup>Dox</sup> was conducted by TEM, UV-visible spectroscopy and fluorescent spectroscopy to ensure the integrity of the viral capsid and successful Dox loading (See **Figure 3.6S** in supporting information).

To study the loading properties for each formulation conditions, the amount of Dox infused/bound to RCNMV were measured by its unique absorption peak at 480 nm, while the concentration of PVN<sup>Dox</sup> capsid were determined by absorbance at 260 nm. The load capacity (LC) of PVN<sup>Dox</sup>, reported as the number of Dox molecules associated with each viral capsid, and load efficiency (LE), the percentage of the Dox loaded with respect to the initial amount of Dox added to the loading preparation, are listed in **Table 3.1** Loading properties of PVNDox suspensions formulated at pH 7.5 in different buffer systems and EDTA concentrations. Even without EDTA in RCNMV pre-treatment pH 7.5, Dox was present associated with the formulated PVN; indicating a probable surface association between Dox and the RCNMV capsid. This presence of surface-bound Dox on the PVN was also suggested by TEM imaging (See **Figure 3.6S** in supporting information). RCNMV suspended in phosphate buffer as compared to Tris buffer shows a much higher tendency to “surface bind” Dox (420 Dox/virion and LE = 12.8% for P<sup>0</sup>-PVN<sup>Dox</sup> as compared to 39 Dox/virion and LE = 1.2% for T<sup>0</sup>-PVN<sup>Dox</sup>). This finding is consistent with previous results of higher negative EP mobility for phosphate buffer-treated RCNMV. However, a very little amount of Dox was loaded into RCNMV (less than 1 Dox/virion) at lower buffer pH (data not shown) due to less electrostatic interaction between viral capsid and Dox. Adding 5 mM EDTA in pH 7.5 buffers significantly increased the Dox loading, yet the loading properties in the two buffer systems were still significantly different ( $p < 0.01$ ) as evident by a difference in the LC of 880 Dox/virion (LE = 26.8%) for

P<sup>5D</sup>-PVN<sup>Dox</sup> and 339 Dox/virion (LE = 10.3%) for T<sup>5D</sup>-PVN<sup>Dox</sup>. Increasing EDTA concentration to 20 mM further facilitated the Dox loading, which led to near equivalency of Dox loading in both buffer systems: 1270 Dox/virion (LE = 38.6%) in phosphate buffer and 1175 Dox/virion (LE = 35.7%) in Tris buffer ( $p > 0.05$ ). This nearly equivalent Dox loading is attributed to sufficient chelation of Ca<sup>2+</sup> and Mg<sup>2+</sup> for RCNMV to induce the formation of open-pores as well as the swollen viral capsid. Consistent with our electrokinetic results, the RCNMV pre-treated at pH 7.5 with EDTA in either phosphate or Tris buffers allows Dox to permeate into the capsid interior and associate with the RCNMV nucleic acids to form a RCNMV RNAs-Dox intercalated complex within PVN. While in theory, 5 mM EDTA would chelate all the divalent cations bound to the RCNMV capsid, the Dox loading results suggested that excess EDTA should be used during drug infusion to facilitate the formation of a “pore-open” state allowing for the maximum encapsulation of Dox into the viral capsid creating the PVN.

**Table 3.1** Loading properties of PVN<sup>Dox</sup> suspensions formulated at pH 7.5 in different buffer systems and EDTA concentrations.

PVN <sup>Dox</sup> Formulations	Dox Load <sup>a)</sup> ( $\mu$ g)		Load Capacity <sup>b)</sup> (Dox /virion)		Load Efficiency <sup>c)</sup> (%)	
	Phosphate	Tris	Phosphate	Tris	Phosphate	Tris
no/ EDTA	24.3	2.4	420	39	12.8	1.2
5 mM EDTA	51.0 $\pm$ 3.5	19.6 $\pm$ 3.0	880 $\pm$ 87	339 $\pm$ 53	26.8 $\pm$ 2.6	10.3 $\pm$ 1.6
20 mM EDTA	73.5 $\pm$ 2.5	68.0 $\pm$ 1.0	1270 $\pm$ 90	1175 $\pm$ 17	38.6 $\pm$ 2.7	35.7 $\pm$ 0.5

<sup>a)</sup>Amount of Dox ( $\mu$ g) loaded in 1 mg PVN<sup>Dox</sup>; <sup>b)</sup>Load capacity (LC) reported as the number of Dox associated with each viral capsid; <sup>c)</sup> Load efficiency (LE) reported as the percentage of the Dox loaded to the initial amount of Dox added to the loading preparation

Previous studies indicate that there are approximately  $\sim 390$   $\text{Ca}^{2+}$  ions located within protein shell of each RCNMV capsid.<sup>[21]</sup> Upon chelation of these  $\text{Ca}^{2+}$  ions after the addition of EDTA to the RCNMV suspension, it is presumed that the calcium-binding residues within the protein shells are accessible to bind with positively charged Dox. This would result in a portion of loaded Dox within the protein shell of RCNMV rather than encapsulation in the viral capsid's internal cavity. Therefore, we speculate that the high amount of Dox ( $\sim 1200$  Dox/virion) loaded to RCNMV in pH 7.5 buffer with 20 mM EDTA is attributed to three sites: 1) acidic residues on the outer surface of protein shell, 2) calcium-binding residues within the protein shell and 3) RNAs in the core of the viral capsid. Understanding the influence of pre-treating parameters (e.g. pH, buffer type and EDTA) on RCNMV provides a strategy to manipulate the electrostatic interaction between the viral capsid and Dox. As a result, we can control loading locations of Dox in RCNMV to tailor the rate of Dox release. For instance, as illustrated in **Figure 3.1**, RCNMV pre-treated in phosphate buffer pH 7.5 with enough EDTA would induce a “pore-open” viral capsid with a higher negatively charged capsid surface (**Figure 3.1a**) due to deprotonation of protein residues as well as phosphate buffer's anionic ions ( $\text{H}_2\text{PO}_4^-/\text{HPO}_4^{2-}$ ). This higher negatively charged surface would possess a higher affinity to electrostatically attract positive-charged Dox during loading; potentially reducing the Dox infusion into the interior capsid thus producing  $\text{PVN}^{\text{Dox}}$  with a high level of surface bound Dox. In contrast, when Tris buffer replaces phosphate buffer, its cationic ions of  $(\text{CH}_2\text{OH})_3\text{CNH}_3^+$  on the capsid surface will repel Dox to reduce surface binding on RCNMV capsid, thereby facilitating the infusion of Dox into the interior capsid. As a result, it produces  $\text{PVN}^{\text{Dox}}$  comprising a high level of Dox encapsulation while maintaining a low level of surface

bound Dox. Moreover, varying EDTA concentration can control the Dox loading capacity as shown in **Table 3.1**. Whether Dox is encapsulated or surface bound on the virion would dictate the release profiles of Dox from PVN<sup>Dox</sup> as described in the next section.

### **3.2.3 *In vitro* release of Dox from PVN<sup>Dox</sup>**

The *in vitro* cumulative release of Dox from PVN<sup>Dox</sup> was investigated in acidic conditions (sodium acetate buffer pH 5.2), alkaline conditions (dibasic sodium phosphate buffer pH 9.0), and physiological conditions (phosphate buffered saline, PBS pH 7.4) with and without EDTA stimuli. The impact of formulating PVN<sup>Dox</sup> at various EDTA and buffer pre-treatment conditions in terms of release profiles was characterized in the release buffer at pH 5.2; a condition where the PVN<sup>Dox</sup> is in the pore-closed state and the encapsulated Dox should be protected in the RCNMV capsid. Comparing the release profile of free Dox with the release profile of P<sup>0</sup>-PVN<sup>Dox</sup> (PVN<sup>Dox</sup> formulated without EDTA in phosphate buffer) shows a 100% cumulative release of Dox within three days when dialyzed against pH 5.2 buffer in each instance (**Figure 3.3a** and **b**). However, the initial release of Dox from P<sup>0</sup>-PVN<sup>Dox</sup> is slightly hindered in comparison to the release of free Dox. As the pre-treatment condition of RCNMV for P<sup>0</sup>-PVN<sup>Dox</sup> lacks the addition of EDTA thus preventing full pore formation, any Dox loaded during in P<sup>0</sup>-PVN<sup>Dox</sup> would be strictly due to a weak surface association between the viral capsid and Dox. According to our electrokinetic results, we attribute this weak surface association to the acidic residues of proteins on the outer capsid surface when RCNMV is dispersed in phosphate buffer. On the other hand, the Dox release rate from the corresponding Tris buffer formulation, T<sup>0</sup>-PVN<sup>Dox</sup>, was below the detection limits.

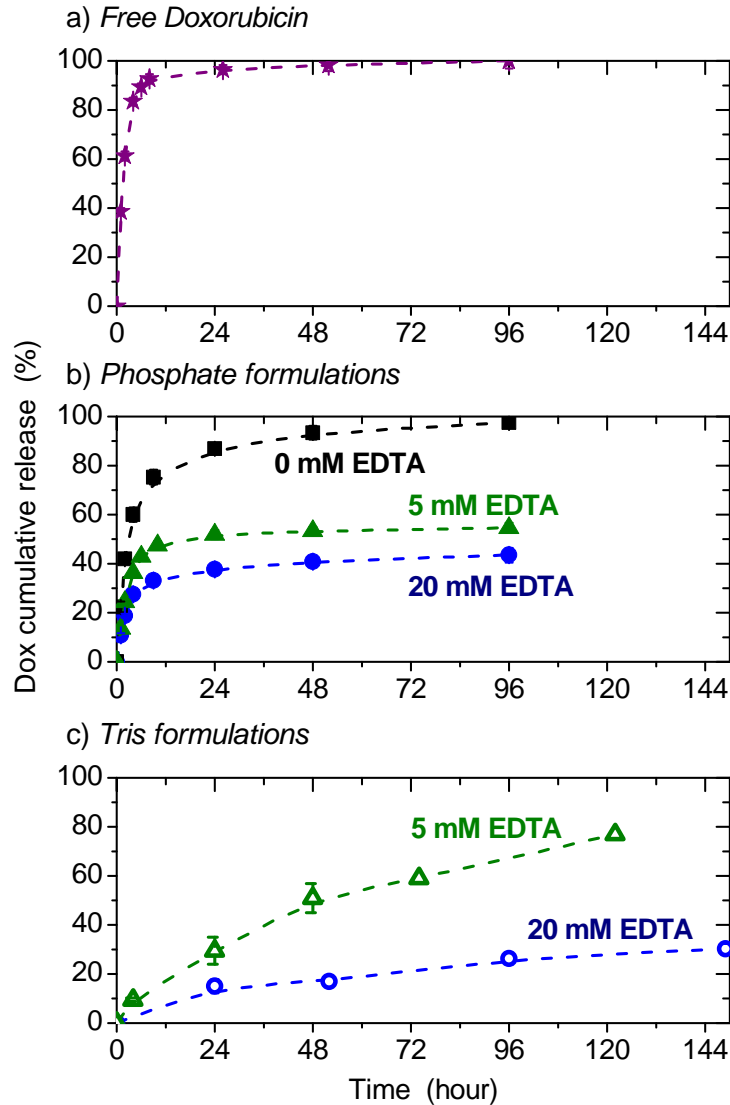


**Figure 3.3** Cumulative Dox release in sodium acetate buffer at pH 5.2 for a) free Dox (★), b) PVN<sup>Dox</sup> formulated in phosphate buffer pH 7.5 with EDTA concentration at 0 mM (■), 5 mM (▲), and 20 mM (●), and c) PVN<sup>Dox</sup> formulated in Tris buffer pH 7.5 with EDTA concentrations at 5 mM (△) and 20 mM (○). The Tris formulation at 0 mM EDTA had negligible Dox release due to minimal Dox loading amount in PVN<sup>Dox</sup> (data not shown). The lines are guides for the eye.

PVN<sup>Dox</sup> prepared with EDTA reagent in phosphate buffer exhibited the bimodal release kinetics, indicative of two levels of binding strength between the viral capsid and Dox. The initial rapid release within the first nine hours may be attributed to surface bound Dox at the

acidic or calcium binding sites, whereas the second and slower release behavior suggests a stronger binding affinity (intercalation) between Dox and the genomic RNAs within the PVN (**Figure 3.3b**). We also observe that increasing the EDTA concentration during loading leads to a decrease in the initial rapid release from  $\sim 47\%$  ( $P^{5D}$ -PVN<sup>Dox</sup>) to  $\sim 33\%$  ( $P^{20D}$ -PVN<sup>Dox</sup>) when released in pH 5.2 buffer. It confirmed our assumption that the EDTA concentration in the RCNMV pretreatment would change the accessibility of the interior virus capsid to the Dox, thereby altering its resultant locations within or on the viral nanoparticle. However, as shown in **Figure 3.3c**, there was no significant burst release from Tris buffer-formulated PVN<sup>Dox</sup> in pH 5.2 medium. A 32% of the loaded Dox demonstrated a slow and sustainable release over 6 days from  $T^{20D}$ -PVN<sup>Dox</sup> prepared in Tris buffer with 20 mM EDTA; providing evidence of a reduced amount of surface-bound Dox. We also observe a relative fast release of Dox from  $T^{5D}$ -PVN<sup>Dox</sup> formulated in Tris buffer with 5 mM EDTA. Therefore, by changing the formulation buffer and EDTA concentration, we can tune the locations of Dox associated with the PVN particle to control the release rate of loaded drugs.

The pH- and ion-responsive release profiles of  $P^{20D}$ -PVN<sup>Dox</sup> and  $T^{20D}$ -PVN<sup>Dox</sup> were further characterized in **Figure 3.4**. An increase in the rate and amount of Dox released from PVN<sup>Dox</sup> was obtained for both buffer formulations as the pH increased in the release medium. Upon an increase of pH from 5.2 to 7.4, the burst release in first nine hours was increased from  $\sim 33\%$  to  $\sim 61\%$  for  $P^{20D}$ -PVN<sup>Dox</sup> formulations, and then followed by a slow Dox release region (**Figure 3.4a**). Interestingly, the similar bimodal release profiles were also obtained for  $T^{20D}$ -PVN<sup>Dox</sup> when released in pH 7.4 PBS buffer (**Figure 3.4b**), where  $\sim 61\%$  of Dox was released within the first 24 hours, and subsequently, a plateau in the cumulative release was reached in

the slow release region. We hypothesize that this slower release behavior is due to the electrostatic attraction of Dox to the RCNMV RNA in the interior of the capsid, which is equal to the Dox diffusivity to the viral capsid's outer surface. Therefore, addition of 20 mM EDTA in pH 7.4 PBS increases the Dox diffusivity to the viral capsid's outer surface by inducing a more negatively charged outer surface and open pores within the capsid.<sup>[21]</sup> Our results show that this was indeed the case as greater than 92% of the loaded Dox from P<sup>20D</sup>- or T<sup>20D</sup>-PVN<sup>Dox</sup> was released within a 24-hour period with EDTA addition to the release medium. Finally, in a pH 9 release buffer, approximately 95% cumulative release of Dox from PVN<sup>Dox</sup> was achieved after 24 hours for both buffer formulations.

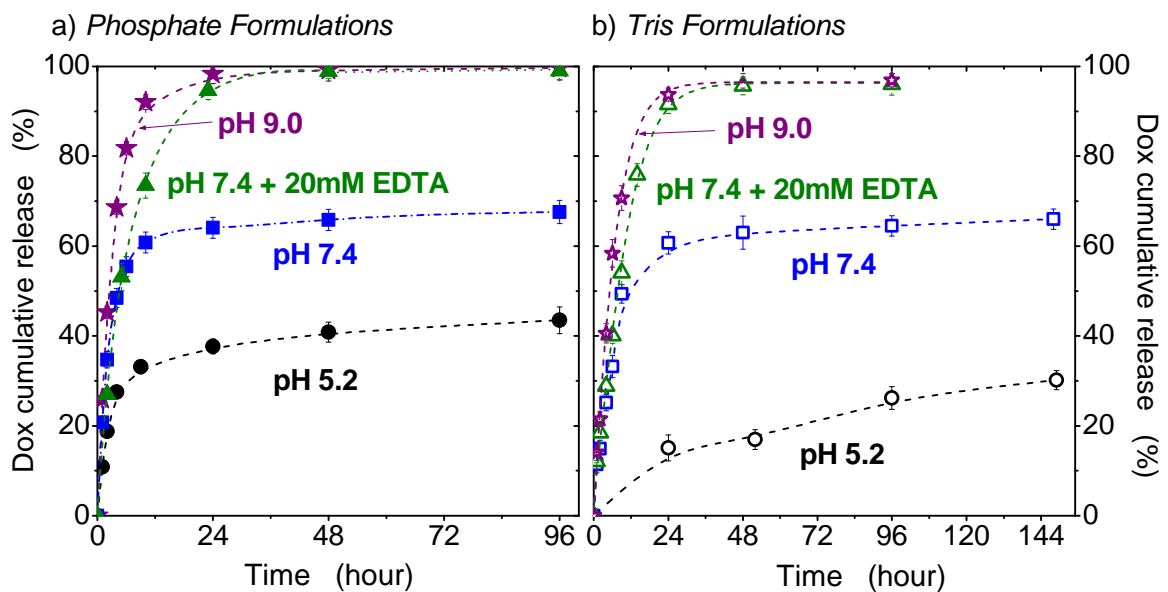


**Figure 3.4** pH- and ion- responsive Dox release from PVN<sup>Dox</sup> formulated at pH 7.5 with 20mM EDTA in either a) phosphate buffer (closed symbols) or b) Tris buffer (open symbols). The pH for release buffer was 5.2 (●,○), 7.4 (■,□), and 9.0 (★,☆). For pH 7.4, 20 mM EDTA (▲,△) was added to accelerate the Dox release by pore formation. The lines are guides for the eye.

### 3.2.4 Release kinetics and mechanism studies

We fit the *in vitro* release data to the Higuchi equation by plotting Dox cumulative release against the square root of release time. A linear relationship for both P<sup>20D</sup>-PVN<sup>Dox</sup> and T<sup>20D</sup>-PVN<sup>Dox</sup> formulations at different pH release conditions was present until the Dox cumulative release reached a plateau region (See **Figure 3.7S** in supporting information). This release behavior suggests that PVN<sup>Dox</sup> is employed as a matrix diffusion-controlled system for delivery of accessible Dox,<sup>[32]</sup> even though the accessibility of loaded Dox in PVN<sup>Dox</sup> is varied upon the loading locations and structural dynamics of PVN particles in the release environments. In other words, the Dox release from PVN<sup>Dox</sup> occurs by the usual molecule diffusion of Dox due to a chemical potential gradient, rather than the degradation or erosion of the PVN particle. Based on this mechanism of drug transport, we hypothesize that three steps determine the drug release rate from PVN: 1) Dox diffuses from the interior of the viral capsid (bulk RNA and RNA-protein bound regions) to the outer protein shell, 2) Dox diffuses through the outer protein shell and 3) Dox releases from the protein shell's outer surface. As listed in **Table 3.2**, the rate constants,  $k_H$ , calculated from the slope of Higuchi plots, indicates faster release kinetics for P<sup>20D</sup>-PVN<sup>Dox</sup> in all releasing conditions as compared to T<sup>20D</sup>-PVN<sup>Dox</sup>. This result quantitatively confirmed that a higher portion of the Dox resides outside and/or within RCNMV's protein shell if PVN<sup>Dox</sup> is formulated in phosphate buffer. The largest discrepancy in release rates occurred when PVN<sup>Dox</sup> was released at pH 5.2 (pore-closed state). In this case, T<sup>20D</sup>-PVN<sup>Dox</sup> demonstrated a substantially slower release of Dox with a rate of 0.026 h<sup>-1/2</sup> over six days. We attribute this low diffusion to the probable location of Dox residing in the interior region of RCNMV. This rate is an order of magnitude lower than P<sup>20D</sup>-PVN<sup>Dox</sup>, which

displayed a fast release of the protein shell-located Dox at a rate of  $0.120 \text{ h}^{-1/2}$  over the first nine hours. Additionally, the  $k_H$  values increased as pH increased in magnitude in the following order for both buffer formulations: acidic pH 5.2 condition < physiological pH 7.4 environment < physiological pH 7.4 with 20 mM EDTA < alkaline condition of pH 9.

**Table 3.2** Dox release rate,  $k_H$  ( $\text{h}^{-1/2}$ ) and coefficient of Determination,  $R^2$ , from fitting *in vitro* Dox release data to the Higuchi equation.

Release buffer	PVN <sup>Dox</sup> -phosphate formulation <sup>+</sup>		PVN <sup>Dox</sup> -Tris formulation <sup>+</sup>	
	$k_H$ ( $\text{h}^{-1/2}$ )	$R^2$	$k_H$ ( $\text{h}^{-1/2}$ )	$R^2$
pH 5.2	0.120	0.986	0.026	0.990
pH 7.4	0.220	0.993	0.133	0.988
pH 7.4 + 20mM EDTA	0.265	0.978	0.233	0.983
pH 9.0	0.387	0.988	0.298	0.985

<sup>+</sup>PVN formulated at pH 7.5 with 20 mM EDTA in respective buffer systems, phosphate or Tris.

Electrokinetic analysis showed that, as the same as the native RCNMV, EP mobility of PVN<sup>Dox</sup> was increased in magnitude as pH increased (**Table 3.3**); indicating the formation of more negatively charged viral particles upon pH increase. Therefore, this pH-responsive release behavior of PVN<sup>Dox</sup> is attributed by the deprotonation of viral protein residues as the environmental pH increased. The increase in negatively charged residues could attract the diffusion of the positively charged Dox to the outer surface of protein shell. The highest release rate of  $0.387 \text{ h}^{-1/2}$  was achieved with P<sup>20D</sup>-PVN<sup>Dox</sup> being released in pH 9 buffer. Addition of EDTA in pH 7.4 buffer also accelerated the Dox release ( $k_H = 0.265 \text{ h}^{-1/2}$  and  $0.233 \text{ h}^{-1/2}$  for phosphate and Tris formulations); as EDTA induces the open-pore state for the capsid thereby facilitating Dox diffusion throughout the protein shell. These release kinetics' results indicate

that formulated PVN<sup>Dox</sup> possesses the same structural transition dependencies on pH and divalent cation concentration as native RCNMV. This trait imparts a controllable release capability to encapsulate molecules from the PVN upon the structural swelling of the capsid protein or re-opening of its pores.

**Table 3.3** Electrophoretic mobility and hydrodynamic diameter for PVN<sup>Dox</sup> in different buffer systems and pH before and after release of Dox. PVN<sup>Dox</sup> was formulated in Tris buffer at pH 7.5 with 20 mM EDTA.

Release Mediums	pH	Electrophoretic mobility ( $\mu\text{m cm V}^{-1} \text{s}^{-1}$ )		Hydrodynamic diameter (nm)	
		Before release	After release	Before release	After release
<i>I. Sodium Acetate</i>					
	4.2	0.43 ± 0.02	-	42.1 ± 1.2	-
	4.6	-0.05 ± 0.01	-	43.5 ± 1.2	-
	5.2	-0.35 ± 0.01	-0.22 ± 0.01	42.3 ± 2.0	37.3 ± 0.8
	6.2	-0.66 ± 0.03	-	39.9 ± 1.8	-
<i>II. Phosphate Buffered Saline, PBS</i>					
	7.4	-0.94 ± 0.03	-1.01 ± 0.04	47.9 ± 1.6	48.7 ± 1.7
+ 20 mM EDTA	7.4	-0.74 ± 0.01	-0.95 ± 0.08	42.0 ± 1.8	33.5 ± 0.7
<i>III. Sodium Phosphate</i>					
	9.0	-1.13 ± 0.03	-0.95 ± 0.05	45.8 ± 1.1	42.1 ± 1.4

To further validate its diffusion-controlled mechanism, the morphology and particle size of PVN<sup>Dox</sup> after *in vitro* release studies were measured by TEM and DLS. All released PVN<sup>Dox</sup> demonstrated the particle integrity in TEM images (see **Figure 3.6S** in supporting information). DLS analysis revealed little or no change in particle size of PVN<sup>Dox</sup> after releasing in different pH conditions. As listed in **Table 3.3**, the hydrodynamic diameter of T<sup>20D</sup>-PVN<sup>Dox</sup> decreased slightly from 42.3 nm to 37.3 nm in pH 5.2 release buffer, and from 45.8 nm to 42.1 nm in pH 9.0 release buffer ( $p < 0.5$ ). This decrease in particle size could be

attributed to the release of surface-bound Dox on PVN<sup>Dox</sup>, rather than surface or bulk erosion of viral particles as the hydrodynamic diameter for native RCNMV is  $\sim 37.6$  nm measured in pH 5.2 (**Figure 3.2d**). No significant change in particle size of T<sup>20D</sup>-PVN<sup>Dox</sup> was observed after releasing in pH 7.4 PBS buffer ( $p > 0.5$ ). These results support the assumption for a release mechanism where the release of Dox from PVN<sup>Dox</sup> under different pH conditions is solely controlled by Fickian diffusion kinetics. However, once a 20 mM EDTA was added to the pH 7.4 PBS buffer, a significant size reduction to  $33.5 \pm 0.74$  nm in hydrodynamic diameter was detected ( $p < 0.01$ ); indicating a disassembly of viral capsid during Dox release, in addition to the diffusion-controlled transport delivery of Dox. Therefore, in the physiological environment with very low concentrations of divalent cations, the Dox molecules are likely released from PVN<sup>Dox</sup> by both diffusion- and erosion- controlled mechanisms. As far as the clinical application is concerned, the Ca<sup>2+</sup> concentration in blood is in the millimolar range, which would be high enough to protect the integrity of PVN<sup>Dox</sup> capsids. Once inside the targeted cells, the concentration of Ca<sup>2+</sup> is low which would trigger the fast release of encapsulated Dox by opening the pores as well as gradually disassembling the viral particles. However, for high-dosage drug delivery to targeted sites, it would be favorable if the diffusion rate of encapsulated Dox throughout PVN<sup>Dox</sup> could be reduced by additional engineering techniques such as surface coating with a biodegradable polymer.

### 3.3 Conclusions

In this study, RCNMV-derived PVN with pH- and ion- sensitive functions have been characterized for therapeutic controlled delivery of Dox in terms of its loading and release

mechanisms. The influence of the electrostatic interaction of Dox with the RCNMV capsid on the loading properties of resultant PVN<sup>Dox</sup> was determined by examining electrokinetic features of the viral capsid as a function of loading parameters (e.g. buffer system, pH or EDTA concentrations). At a low pH (from 4.2 to 6.2), the net charge of the RCNMV capsid was not negative enough to induce the infusion of positively charged Dox resulting in low loading of Dox into viral capsid. The maximum loading of PVN<sup>Dox</sup> at ~ 1200 Dox per virion was achieved by inducing the higher negatively charged RCNMV capsid at pH 7.5 buffer together with induction of fully flow permeation to the interior of the viral capsid by formation of open pores using EDTA as a chelating agent. The nature of the loading buffer provides opportunities for tuning the location of Dox binding, thus it is possible to tailor the corresponding rates of Dox release. Anionic species ( $\text{H}_2\text{PO}_4^-/\text{HPO}_4^{2-}$ ) of phosphate buffer induce a more negatively charged outer capsid surface, thus a higher affinity for surface binding with Dox is achieved. In contrast, the cationic ions ( $\text{Tris-NH}_3^+$ ) in Tris buffer will compete with Dox to bind with the negatively charged sites on the viral capsid, thereby effectively reducing the amount of surface-bound Dox. The locations of Dox within and on the viral capsid were predominantly manifested in the release profiles of PVN<sup>Dox</sup>. An initial rapid release by surface-bound Dox was demonstrated followed by a very slow release due to the stronger binding affinity of encapsulated Dox within the viral capsid. Furthermore, the release behavior of PVN<sup>Dox</sup> in different releasing environments was studied thoroughly. It was found that formulated PVN<sup>Dox</sup> underwent the same structural transitions as the native RCNMV at various pH and divalent cation concentrations. This trait enables pH- and ion- responsive controlled release of loaded drug from PVN. The rate of release and amount of released drug both increased as pH of the

release medium was increased or the concentration of divalent cation was decreased. Mathematical modeling of drug release kinetics indicated that the PVN<sup>Dox</sup> system approaches a matrix diffusion-controlled release mechanism described by Fickian diffusion at acidic, alkaline or physiological environments, while it showed the combination of diffusion- and erosion- controlled mechanisms when released in physiological environments with very low concentrations of divalent cations.

### **3.4 Experimental**

#### **3.4.1 Materials**

Doxorubicin hydrochloride (Dox) was purchased from Tocris Bioscience (Bristol UK), and dissolved in dimethyl sulfoxide (DMSO) anhydrous to make a solution stock at 20 mg ml<sup>-1</sup>. Monobasic sodium phosphate, dibasic sodium phosphate, tris(hydroxymethyl) aminomethane, hydrochloric acid, phosphate buffered saline (PBS), calcium chloride, DMSO, sodium dodecyl sulfate (SDS) and acetonitrile were obtained from Fisher Scientific. Ethylenediaminetetraacetic acid (EDTA) and sodium acetate was purchased from EMD Millipore. Proteinase K buffered aqueous glycerol solution was obtained from Sigma. Uranyl acetate was purchased from Electron Microscopy Sciences.

#### **3.4.2 RCNMV propagation and purification**

*Nicotiana clevelandi* plants (4 to 6 weeks old) were rub-inoculated with RCNMV RNA transcripts<sup>[33]</sup> and maintained in a greenhouse at 20 to 24 °C. After 7 – 10 days of propagation, the infected leaves were harvested and the virions were purified as previously described.<sup>[34]</sup>

The typical yield obtained was approximately 8 to 20 mg of pure RCNMV from 100g of infected leaf tissue. The concentration of virus was determined by absorbance measurement at 260 nm with an extinction coefficient (1 cm light path) of 6.46.<sup>[21]</sup> A pure virus preparation has an A260 nm: A280 nm absorbance ratio of 1.63 ~1.69. Native RCNMV was stored in 20 mM sodium phosphate buffer pH 7.2 at 4°C before use to preserve its integrity over an extended period of 6 months.

### **3.4.3 Infusion of Dox into RCNMV capsid**

Dox was infused into RCNMV capsids via a reversible pore opening mechanism.<sup>[19a]</sup> RCNMV suspensions were adjusted to a concentration of 3 mg/ml in either 20 mM sodium phosphate buffer or Tris buffer at different pH values (pH 4.2, pH 5.2, pH 6.2 or pH 7.5) and subsequently adjusted to varying EDTA concentrations (0 mM, 5 mM or 20 mM). The suspensions were equilibrated for 1 hour to induce the pore-open condition on the exterior of the virus capsid prior to loading Dox.<sup>[21]</sup> Next, a 4 mg/ml Dox solution was added at a molar ratio of 3300:1 Dox to virions (the molecular weight of RCNMV is  $1 \times 10^7$  g mol<sup>-1</sup>) and then gently mixed overnight to allow the infusion of Dox to completion. At the end of the infusion period, 25 mM CaCl<sub>2</sub> was added, the pH lowered by addition of 0.2 M sodium acetate buffer pH 5.2 and incubated for an additional 30 minutes to close the pores on the viral capsid. Excess Dox molecules were removed by running the loaded RCNMVs through a size exclusion column (NAP<sup>TM</sup> 10 columns, GE Healthcare) several times, and Dox-loaded PVNs were collected in 0.2 M sodium acetate buffer pH 5.2. The concentration of PVN<sup>Dox</sup> was measured with a NanoDrop 1000 Spectrophotometer at 260 nm. The loading amount of Dox in PVN<sup>Dox</sup>

were determined by the UV-visible spectra (Synergy HT microplate reader, BioTek) at wavelength of 480 nm with the extinctive coefficient from a calibration curve established by standard Dox concentrations. The loading capacity (LC) reported as the number of Dox molecules associated with each viral capsid and loading efficiency (LE) represented as the percentage of the Dox loaded with respect to the initial amount of Dox added to the loading preparation were calculated as follows:

$$LC = (weight_{Dox\ loaded}/weight_{PVN}) \times (mw_{PVN}/mw_{Dox}) \quad (1)$$

$$LE = (weight_{Dox\ loaded}/weight_{total\ of\ add\ Dox}) \times 100\% \quad (2)$$

where  $mw_{PVN}$  and  $mw_{Dox}$  are the molecular weights of the viral capsid at  $1 \times 10^7$  g mol<sup>-1</sup> and Dox at 579.29 g mol<sup>-1</sup>, respectively.

#### 3.4.4 Electrokinetic and DLS measurements of RCNMV and PVN<sup>Dox</sup>

Electrophoretic (EP) mobility and hydrodynamic diameter of RCNMV and PVN<sup>Dox</sup> were studied as a function of pH (4.2, 5.2, 6.2 and 7.5), EDTA concentration (0 mM, 5 mM and 20 mM) and buffer system (sodium phosphate or Tris buffer) using a Zetasizer Nano ZS instrument (Malvern Instruments). The different buffer systems were used to obtain a range of pH solutions for probing the electrokinetics. The molarity for all buffers was kept at 20 mM to ensure consistent ion strength amongst solutions. For electrokinetic analysis, aliquots of sample were held in a universal dip cell kit (ZEN1002, Malvern Instruments). The EP mobility refers to the velocity of a charged particle in a unit electric field, which is measured by frequency shift of scattered light under laser Doppler electrophoresis.<sup>[35]</sup> The hydrodynamic diameters of RCNMV and PVN<sup>Dox</sup> were determined by dynamic light scattering (DLS). The

measurements were conducted in a 4.5 ml disposable cuvette, where the Brownian motion of molecules in solution were detected by the fluctuations of the scattering intensity and then correlated to hydrodynamic size via the Stokes-Einstein equation.<sup>[35]</sup> The particle concentration was 0.2 mg ml<sup>-1</sup> for all measurements.

#### **3.4.5 *In vitro* Dox release from PVN<sup>Dox</sup>**

A dialysis-based assay<sup>[36]</sup> was carried out to study the *in vitro* release performance of Dox molecules from PVN<sup>Dox</sup>. A 500 µl PVN<sup>Dox</sup> suspension or free Dox at equivalent concentrations was injected into a dialysis bag with a MWCO of 3.5–5 kDa (Spectra/Por<sup>®</sup> Micro Floate-A-lyzer, Spectrum Laboratories, Inc.). The dialysis bag was immersed in 200 ml release medium containing either sodium acetate buffer (20 mM, pH 5.2), phosphate-buffered saline (PBS, 20mM, pH 7.4), sodium phosphate buffer (20 mM, pH 9.0) or PBS buffer with 20 mM EDTA. The concentration of Dox that remained in the dialysis bag at set intervals was measured by the absorbance spectra at 480 nm. Fresh release medium was replaced after every 4 hours to maintain a constant sink condition. Data is reported as the average percentage of Dox cumulative release for samples in triplicate.

For a quantitative determination of Dox release kinetics from PVN<sup>Dox</sup>, it was assumed that Dox molecules were homogenously dispersed within the PVN<sup>Dox</sup> and the diffusion coefficient of Dox through the PVN does not change during release. The *in vitro* Dox cumulative release data was fit to an exponential relation for Fickian diffusion of a drug from spherical polymeric devices, the Higuchi equation<sup>[37]</sup>:

$$\frac{M_t}{M_\infty} = k_H \sqrt{t} \quad (k_H = \frac{4}{l} \sqrt{\frac{D}{\pi}}) \quad (3)$$

where  $M_t/M_\infty$  is the cumulative drug release,  $k_H$  is the Higuchi release rate constant which is affected by the layer thickness of polymer barrier,  $l$ , and the diffusion coefficient of drug,  $D$ .

### 3.4.6 Statistical Analysis

Data were expressed in terms of mean value and standard deviation and were analyzed using Student's t-test. Data were considered as being significantly different for  $p$  values  $< 0.05$ .

## 3.5 References

- [1] S. C. Hock, Y. M. Ying and C. L. Wah, *PDA Journal of Pharmaceutical Science and Technology* **2011**, 65, 177.
- [2] W. T. Al-Jamal and K. Kostarelos, *Acc. Chem. Res.* **2011**, 44, 1094.
- [3] M. Najlah and A. D'Emanuele, *Curr. Opin. Drug Discovery Dev.* **2007**, 10, 756.
- [4] a) E. M. Pridgen, R. Langer and O. C. Farokhzad, *Nanomedicine (Lond)* **2007**, 2, 669; b) H. M. Aliabadi, M. Shahin, D. R. Brocks and A. Lavasanifar, *Clinical Pharmacokinetics* **2008**, 47, 619.
- [5] G. Huang, J. Gao, Z. Hu, J. V. St John, B. C. Ponder and D. Moro, *J Control Release* **2004**, 94, 303.
- [6] A. MaHam, Z. Tang, H. Wu, J. Wang and Y. Lin, *Small* **2009**, 5, 1706.
- [7] A. Wilczewska, K. Niemirowicz, K. Markiewicz and H. Car, *Pharmacol. Rep.* **2012**, 64, 1020.

- [8] F. Alexis, E. Pridgen, R. Langer and O. Farokhzad in *Nanoparticle Technologies for Cancer Therapy*, Vol. 197 (Ed. M. Schäfer-Korting), Springer Berlin Heidelberg, **2010**, pp. 55.
- [9] F. Alexis, E. M. Pridgen, R. Langer and O. C. Farokhzad, *Handbook of experimental pharmacology* **2010**, 55.
- [10] a) Y. Ren, S. Wong and L. Lim, *Pharm. Res.* **2010**, 27, 2509; b) Y. Ma, R. J. M. Nolte and J. J. L. M. Cornelissen, *Adv. Drug Delivery Rev.* **2012**, 64, 811; c) S. Bhattacharya and B. Mazumber, *BioPharm International* **2011**, 24, pS9.
- [11] P. Singh, M. J. Gonzalez and M. Manchester, *Drug Dev. Res.* **2006**, 67, 23.
- [12] C. Bergsdorf, C. Beyer, V. Umansky, M. Werr and M. Sapp, *FEBS Lett.* **2003**, 536, 120.
- [13] Y. Ren, S. M. Wong and L.-Y. Lim, *Bioconjugate Chem.* **2007**, 18, 836.
- [14] M. Uchida, M. L. Flenniken, M. Allen, D. A. Willits, B. E. Crowley, S. Brumfield, A. F. Willis, L. Jackiw, M. Jutila, M. J. Young and T. Douglas, *J. Am. Chem. Soc.* **2006**, 128, 16626.
- [15] M. L. Flenniken, L. O. Liepold, B. E. Crowley, D. A. Willits, M. J. Young and T. Douglas, *Chemical Communications* **2005**, 0, 447.
- [16] J. M. Johnson, D. A. Willits, M. J. Young and A. Zlotnick, *J. Mol. Biol.* **2004**, 335, 455.
- [17] C. E. Ashley, E. C. Carnes, G. K. Phillips, P. N. Durfee, M. D. Buley, C. A. Lino, D. P. Padilla, B. Phillips, M. B. Carter, C. L. Willman, C. J. Brinker, J. d. C. Caldeira, B. Chackerian, W. Wharton and D. S. Peabody, *ACS Nano* **2011**, 5, 5729.
- [18] D. Ren, F. Kratz and S. W. Wang, *Small* **2011**, 7, 1051.
- [19] a) L. Loo, R. H. Guenther, S. A. Lommel and S. Franzen, *Chem Commun (Camb)* **2008**, 88; b) O. L. Lars, R. Jennifer, A. Mark, O. Luke, Y. Mark and D. Trevor, *Phys. Biol.* **2005**, 2, S166; c) Q. Zeng, H. Wen, Q. Wen, X. Chen, Y. Wang, W. Xuan, J. Liang and S. Wan,

*Biomaterials* **2013**, *34*, 4632; d) I. Yildiz, K. L. Lee, K. Chen, S. Shukla and N. F. Steinmetz, *J. Controlled Release*.

[20] Z. Xiong and S. A. Lommel, *Virology* **1989**, *171*, 543.

[21] M. B. Sherman, R. H. Guenther, F. Tama, T. L. Sit, C. L. Brooks, A. M. Mikhailov, E. V. Orlova, T. S. Baker and S. A. Lommel, *J. Virol.* **2006**, *80*, 10395.

[22] a) D. M. Lockney, R. N. Guenther, L. Loo, W. Overton, R. Antonelli, J. Clark, M. Hu, C. Luft, S. A. Lommel and S. Franzen, *Bioconjug Chem* **2011**, *22*, 67; b) R. Wang, D. M. Lockney, M. B. Goshe and S. Franzen, *Bioconjug Chem* **2011**, *22*, 1970.

[23] S. Honarbakhsh, R. H. Guenther, J. A. Willoughby, S. A. Lommel and B. Pourdeyhimi, *Adv. Healthcare Mater.* **2013**.

[24] S. Lv, M. Li, Z. Tang, W. Song, H. Sun, H. Liu and X. Chen, *Acta Biomaterialia*.

[25] a) H. Simphins, L. F. Pearlman and L. M. Thompson, *Cancer Research* **1984**, *44*, 613; b) J. Cummings, A. Bartoszek and J. F. Smyth, *Analytical Biochemistry* **1991**, *194*, 146.

[26] a) Z. Adamczyk, M. Nattich, M. Wasilewska and M. Zaucha, *Adv. Colloid Interface Sci.* **2011**, *168*, 3; b) C. Zhao and C. Yang, *Microfluid. Nanofluid.* **2012**, *13*, 179.

[27] a) H. Ohshima, *Curr. Opin. Colloid Interface Sci.* **2013**, *18*, 73; b) J. Langlet, F. Gaboriaud, C. Gantzer and J. F. L. Duval, *Biophys. J.* **2008**, *94*, 3293.

[28] B. Michen and T. Graule, *Journal of Applied Microbiology* **2010**, *109*, 388.

[29] L. Wang, L. C. Lane and D. L. Smith, *Protein Science* **2001**, *10*, 1234.

[30] F. Cugia, M. Monduzzi, B. W. Ninham and A. Salis, *RSC Adv.* **2013**, 5882.

[31] J. A. Speir, S. Munshi, G. Wang, T. S. Baker and J. E. Johnson, *Structure* **1995**, *3*, 63.

- [32] D. Y. Arifin, L. Y. Lee and C.-H. Wang, *Advanced Drug Delivery Reviews* **2006**, 58, 1274.
- [33] Z. G. Xiong and S. A. Lommel, *Virology* **1991**, 182, 388.
- [34] D. Lockney, S. Franzen and S. Lommel, *Methods Mol Biol* **2011**, 726, 207.
- [35] in *Zetasizer Series: Dynamic light scattering and zeta potential*, Vol. Malvern Instruments, **2012**.
- [36] C. Y. Zhang, Y. Q. Yang, T. X. Huang, B. Zhao, X. D. Guo, J. F. Wang and L. J. Zhang, *Biomaterials* **2012**, 33, 6273.
- [37] a) T. Higuchi, *J. Pharm. Sci.* **1963**, 52, 1145; b) M. R. Brophy and P. B. Deasy, *Int. J. Pharm.* **1987**, 37, 41; c) J. Siepmann and N. A. Peppas, *Int. J. Pharm.* **2011**, 418, 6.

### 3.6 Supporting Information

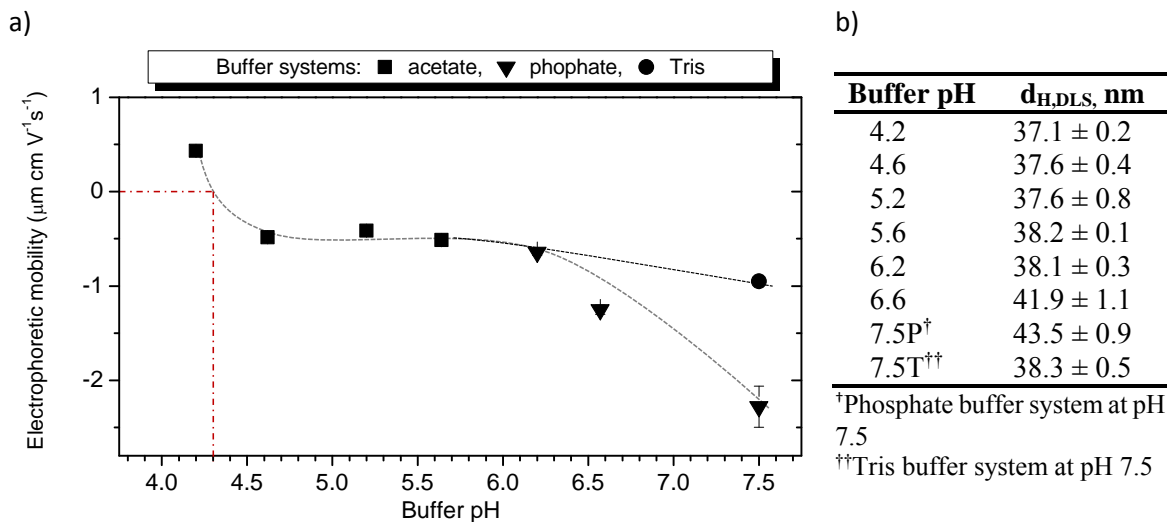


**Figure 3.5S** Native RCNMV a) electrophoretic mobility and b) hydrodynamic diameter as a function of buffer pH. The lines in (a) are presented as guides to the eye.

### Characterization of native RCNMV and PVN<sup>Dox</sup> by TEM, UV/Visible spectroscopy and Fluorescence spectroscopy

#### Methods:

The morphology of native RCNMV and PVN<sup>Dox</sup> was analyzed using TEM with negative staining (JEOL 100S TEM). A 5  $\mu\text{l}$  sample ( $\sim 1 \text{ mg ml}^{-1}$ ) was deposited onto a copper mesh grid (Formvar/Carbon 400 mesh Cu grid, Ted Pella, Inc.) and wicked off after a 20 second immersion using 3MM Whatman filter paper. A 10  $\mu\text{l}$  drop of 2% uranyl acetate solution ( $\text{w v}^{-1}$ ) was applied and removed after 20 seconds. The prepared grid was vacuum dried for 30 minutes and stored in a desiccation chamber before TEM observations.

UV/Visible spectra (240–700 nm wavelength) and fluorescence spectra of native RCNMV, PVN<sup>Dox</sup> and free Dox at equivalent concentrations were analyzed with the aid of a

microplate reader (Synergy HT, BioTek). The fluorescence spectra of free Dox and loaded Dox in PVN at the equivalent concentrations were monitored at an excitation of 480 nm with a corresponding emission recorded between 500–700 nm.

*Results and Discussion:*

As shown in **Figure 3.6Sa**, TEM analysis of PVN<sup>Dox</sup> revealed the capsid integrity of RCNMV, as indicated by the intact geometry of the virus, after infusion with Dox or release of Dox in a physiological environment (phosphate buffered saline, PBS at pH 7.4). In contrast, the surface morphology of PVN<sup>Dox</sup> seems to be altered as compared to the TEM image of the native RCNMV where negatively stained protrusions are apparent on its outer surface. This RCNMV TEM image is consistent with the cryo-EM reconstruction of the RCNMV capsid demonstrating 90 distinct protrusions (approximately 3.7 nm, P domain) from the capsid shell (approximately 3 nm in thickness, S domain). PVN<sup>Dox</sup>, however, shows the absence of these stained protrusions. We speculate that if Dox was surface bound on the protein capsid of RCNMV, this smoother surface morphology could be expected from TEM imaging as Dox would fill the voids between the P-domain protrusions. After the release of Dox from PVN, the negatively stained protrusions are once again apparent on the viral nanoparticles.

PVN<sup>Dox</sup>, native RCNMV, and free Dox at equivalent concentrations were subjected to UV-visible and fluorescence spectroscopy analysis. As illustrated in **Figure 3.6Sb**, both RCNMV and free Dox have an absorbance at 260 nm, whereas the Dox has a unique absorbance at 480 nm. The visible absorption band of PVN<sup>Dox</sup> corresponds to the Dox chromophore becoming broad; in addition, the absorption peak was red-shifted to 490 nm and decreased in intensity due to the intercalation of Dox with virion RNA and the increased

concentration of Dox molecules within its interior.<sup>[1]</sup> Finally, the fluorescence intensity of  $PVN^{Dox}$  was self-quenching compared to similar amounts of the free Dox in solution, which may be attributed to the formation of non-fluorescent dimers because of the close distance between Dox molecules when constrained within the interior of the virion capsid.<sup>[2]</sup> These spectra results support the hypothesis that Dox can infuse into the interior cavity of RCNMV for possible complexation with the virion RNA to provide a mechanism for subsequent tailorable release.

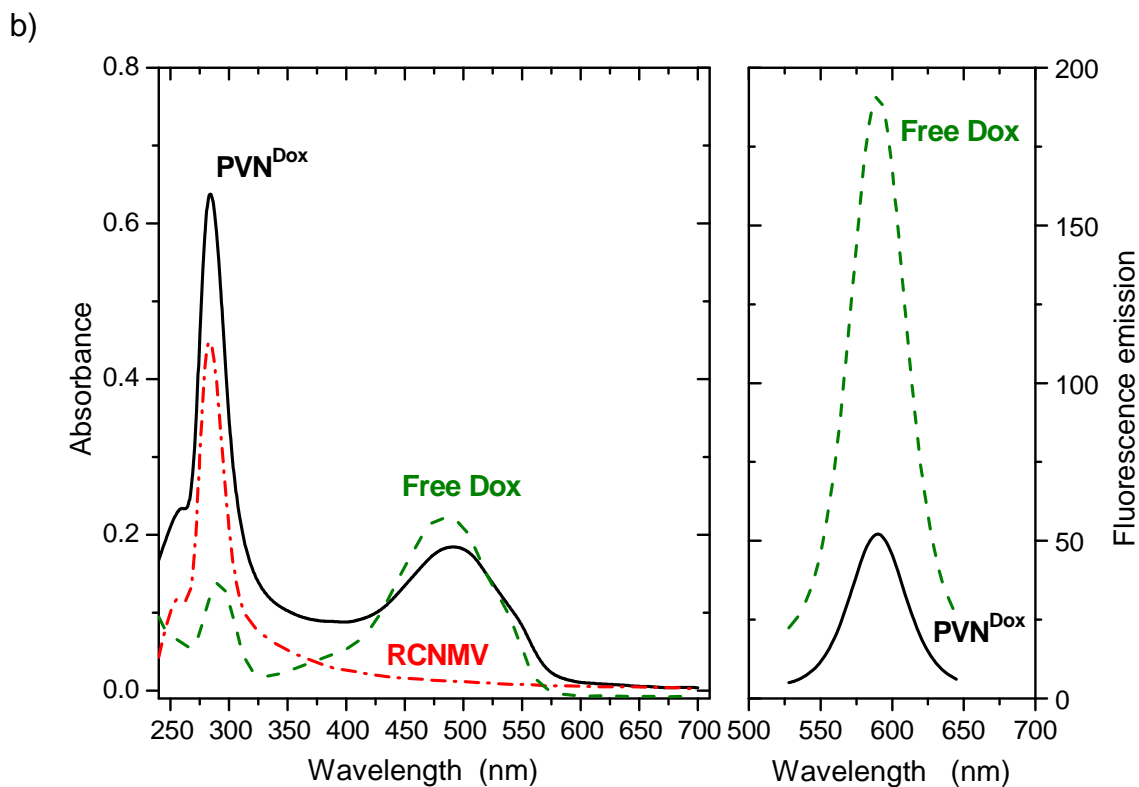
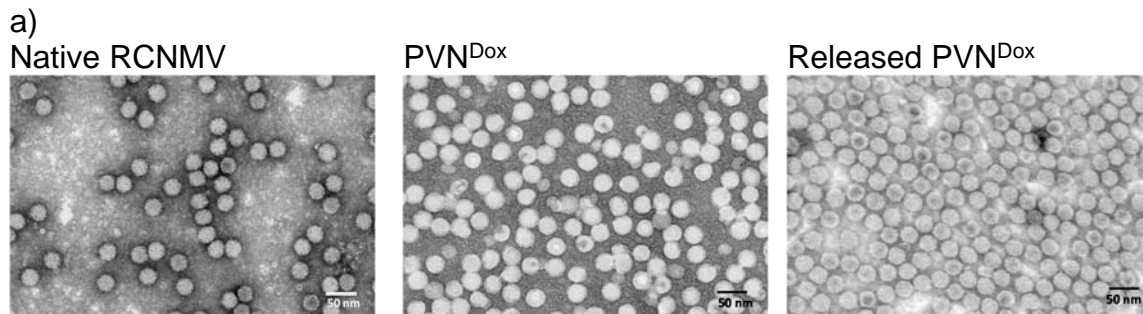


**Figure 3.6S** Characterization via a) transmission electron microscopy for native RCNMV, PVN<sup>Dox</sup> in sodium acetate buffer pH 5.2, and PVN<sup>Dox</sup> after release of Dox in PBS pH 7.4; b) UV/Visible absorption and fluorescence spectra for RCNMV (0.25 mg ml<sup>-1</sup>), PVN<sup>Dox</sup> (0.5 mg ml<sup>-1</sup>), and free Dox at equivalent concentrated of 34 µg ml<sup>-1</sup>.

By fitting the pH-responsive release data into the Higuchi equation, we found that the plots of Dox cumulative release from P<sup>20D</sup>-PVN<sup>Dox</sup> (phosphate formulation) against square root of release time showed a linear relationship in the first 9 hours-release for all release conditions (**Figure 3.7Sa**). After that time, the Dox release reached the plateau region because that amount

of loaded Dox is inaccessible due to the strongly association with genomic RNA within the viral capsid. However, the amounts of accessible or inaccessible loaded Dox were dependent on the structural dynamics of PVN particles in the release environment. Compared to pH 5.2 release medium, the protein shell of PVN particle becomes more negative charged and the structure of the particle is swelling in the pH 7.4 release medium; resulting in more accessible Dox to be diffused out. Although the loaded Dox in  $P^{20D}$ -PVN<sup>Dox</sup> shown fully accessible in pH 7.4 PBS with 20 mM EDTA and pH 9.0 release mediums, the proportion of the released Dox against the square root of release time is approximately linear for the first 80% of cumulative drug release, in agreement with the limitations of the Higuchi model.<sup>[3]</sup> The same observations were shown in the Higuchi linear fitting for the release data of  $T^{20D}$ -PVN<sup>Dox</sup> (**Figure 3.7Sb**. Tris formulation). However, the plateau region of  $T^{20D}$ -PVN<sup>Dox</sup> was achieved after 24-hour release time in pH 7.4 medium. This is because the  $T^{20D}$ -PVN<sup>Dox</sup> consists of the less amount of surface bounded Dox compared to  $P^{20D}$ -PVN<sup>Dox</sup>. The release of  $T^{20D}$ -PVN<sup>Dox</sup> in pH 5.2 medium only shows one of the slow and sustainable release region because the most of loaded Dox were encapsulated within the viral capsid.

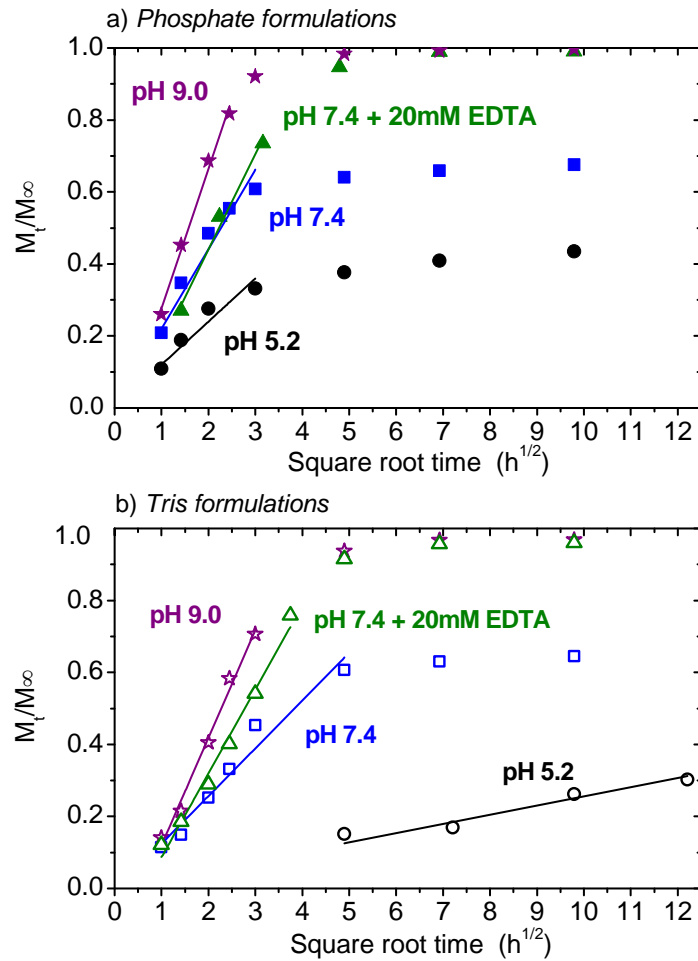


**Figure 3.7S** Higuchi plots of Dox cumulative release ( $M_t/M_\infty$ ) against square root hour ( $h^{1/2}$ ) for PVN<sup>Dox</sup> formulated at pH 7.5 with 20 mM EDTA in either a) phosphate buffer (closed symbols) or b) Tris buffer (open symbols). The pH for release buffer was 5.2 (●,○), 7.4 (■,□), and 9.0 (★,☆). For pH 7.4, 20 mM EDTA (▲,△) was added to accelerate the release rate by pore formation.

## References:

- [1] a) H. Porumb, *Progress in Biophysics and Molecular Biology* **1979**, *34*, 175; b) K. Li, Y. Chen, S. Li, H. G. Nguyen, Z. Niu, S. You, C. M. Mello, X. Lu and Q. Wang, *Bioconjugate Chemistry* **2010**, *21*, 1369.
- [2] a) F. A. de Wolf, M. Maliepaard, F. van Dorsten, I. Berghuis, K. Nicolay and B. de Kruijff, *Biochimica et Biophysica Acta (BBA) - Molecular Basis of Disease* **1990**, *1096*, 67; b) Q. Zeng, H. Wen, Q. Wen, X. Chen, Y. Wang, W. Xuan, J. Liang and S. Wan, *Biomaterials* **2013**, *34*, 4632.
- [3] D. Y. Arifin, L. Y. Lee and C. H. Wang, *Adv. Drug Delivery Rev.* **2006**, *58*, 1274.

## **Chapter 4. Development of Abamectin Loaded Plant Viral Nanoparticle for Efficacious Nematode Control**

### **Abstract:**

In this Chapter, we are translating our “stealth” and targeted drug delivery technology for controlled release of cancer therapeutics into targeted delivery of active agents for crop protection and enhancement. In the case of nematicides, the encapsulation by a smart particle such as our plant viral nanoparticle (PVN) eliminates non-target adverse effects. This ecological bonus prevents killing beneficial organisms in the soil as well as isolates the toxicity of the nematicide from the end-user. A biological nematicide, abamectin (Abm), is successfully infused into a Red clover necrotic mosaic virus (RCNMV)-derived PVN via RCNMV’s structural dynamics of pore formation. The characterization of Abm-loaded PVN (PVN<sup>Abm</sup>) by transmission electron microscopy and dynamic light scattering indicates an intact integrity and morphology of viral capsid as the native RCNMV. The encapsulation of Abm by PVN significantly increases Abm’s soil mobility while remaining its bioavailability against nematodes. As a result, the PVN<sup>Abm</sup> enlarges the zone of protection that limited by free Abm; contributing to the enhanced nematicide performance for plant parasite nematode control.

## 4.1 Introduction

Plant-parasitic nematodes (PPNs) are one of the world's major agricultural pests, causing in excess of \$157 billion in worldwide crop damage annually.<sup>[1]</sup> As these parasitic worms attack crop root systems, they siphon crucial growth nutrients reducing crop yields. The surviving plants also are more vulnerable to secondary infections, drought and other stresses. The vast majority of PPN damage is caused by sedentary endoparasitic forms, in particular, the root-knot nematodes (RKN: *Meloidogyne* spp.) and soybean cyst (*Heterodera glycines*: SCN) and potato cyst (*Globodera* spp.: PCN) nematodes which impact virtually a wide range of crops such as soybeans, potatoes, bananas, cotton, corn, strawberries, and tomatoes to name a few.<sup>[2]</sup>

Relatively few measures exist for controlling PPN infestation despite their large damage potential. Crop rotation is a commonly employed tactic to manage specific PPN species,<sup>[3]</sup> but its overall effectiveness is hampered by the polyspecific nature of most PPN infestations, and may not be economically feasible for many growers. Host resistance is an environmentally and economically sound method to manage selected PPN species, but unfortunately, genetic resistance to PPN is not available for most cultivated crops.<sup>[4]</sup> In addition, traditional methods for plant breeding require 5-10 years to produce a viable variety, however, new nematode control tools are an immediate and critical need. Although these PPN control strategies were reported to reduce nematode infection to some extent, none of them provided the same efficacious and economic benefits as the chemical treatment by nematicides.<sup>[5]</sup> Traditionally, one of the most effective pesticides for PPN control is dependent on highly toxic contact and fumigant nematicides, such as methyl bromide.<sup>[6]</sup> However, the use of these type of pesticides

have been restricted or eliminated due to environmental concern. Another option is the application of pre-planting non-fumigant nematicides, but their repetitive use in crops leads to a loss of efficacy caused by soil microorganisms developing a resistance to them.<sup>[7]</sup> Hence, there is a growing interest in development of a new chemical compounds or control strategies that are both effective and environmentally safer to use.

A biological active ingredient, abamectin (Abm), has drawn great attention to be a promising nematicide for PPN control, whose product was commercialized as a granular or liquid formulation (Avid<sup>®</sup>) and most recently formulated in seed treatment (Avicta<sup>®</sup>) by Syngenta Crop Protection. Abm is a mixture of macrocyclic lactone metabolites ( $\geq 80\%$  avermectin B<sub>1a</sub> and  $\leq 20\%$  avermectin B<sub>1b</sub>) derived from the bacterium *Streptomyces avermitilis* and has been shown to have strong activity against a broad spectrum of nematodes yet is generally regarded as safe for mammals due to its inability to pass the blood-brain barrier.<sup>[8]</sup> Abm acts as PPN control method through direct protein inhibition by binding to the GABA receptors in nerve and muscle cells.<sup>[9]</sup> However, one basic problem that compromises Abm's efficacy is its insolubility in water; hence, high tendency to bind to organic soil particles resulting in very poor movement in the soil.<sup>[10, 11]</sup> These traits create a very limited zone of protection around the developing root system. It has been reported that a large portion of a Abm dose remains with the seed coat, leaving the radical unprotected plant after germination.<sup>[12]</sup> Abm in liquid formulations were also blamed for the minimal root uptake due to its poor mobility in soil.<sup>[13]</sup> In addition, another drawback of Abm as a PPN control nematicide is lack of persistence over time due to its rapid degradation by photo-oxidation.<sup>[14]</sup> As a result, although PPN damage reduction is reported by using Abm formulations, it is generally minor (+/- 50%) and only

marginally economic for lower value crops. Therefore, there is a critical need to resolve the soil mobility issues for Abm compounds to enhance its effectiveness against nematode damage.

In this study, we developed an approach to increase the mobility or distribution of Abm within the soil by incorporating it into a *Red clover necrotic mosaic virus* (RCNMV)-derived plant viral nanoparticle (PVN). The encapsulation by the PVN carrier also could improve the Abm's stability as well as isolate the toxicity of the nematicide from the end-user. RCNMV is a T=3 icosahedral soil-transmitted plant virus with a diameter of 36 nm. The RCNMV capsid consists of 180 copies of the 38 kDa capsid protein (CP) that assembles to package either 1 copy each of a 3.9 kb single-stranded RNA-1 and a 1.5 kb RNA-2 or 4 copies of RNA-2.<sup>[15]</sup> Its inner 17nm-diameter space provides a nanoscale carrier to load and protect the foreign active cargo via the pore formation mechanism for intended delivery.<sup>[16]</sup> In addition, RCNMV is remarkably hardy and can withstand extremes of temperature and pH, organic solvents, nuclease and protease attack. The combination of its inherent structural features and robustness makes it an excellent candidate for the delivery of Abm nematicides within soil. The specific aims of this study were to determine (i) the feasibility of formulating PVN with Abm as a loading compound (PVN<sup>Abm</sup>) and (ii) the retained bioavailability of PVN<sup>Abm</sup> to nematodes as compared to free Abm, and (iii) to evaluate the mobility and nematicide efficacy of PVN<sup>Abm</sup> within the soil.

## 4.2 Experimental

### 4.2.1 Materials

Abamectin (Abm) was purchased from Sigma-Aldrich and dissolved in 90 % (v v<sup>-1</sup>) ethyl alcohol to make a solution stock at 2 mg ml<sup>-1</sup>. Monobasic sodium phosphate, dibasic sodium phosphate, calcium chloride, DMSO, sodium dodecyl sulfate (SDS) and acetonitrile were obtained from Fisher Scientific. Ethylenediaminetetraacetic acid (EDTA) and sodium acetate was purchased from EMD Millipore. Proteinase K buffered aqueous glycerol solution, Rhodamine, N-methylimidazole, Trifluoroacetic anhydride, Acetonitrile anhydrous and M9 buffer powder was obtained from Sigma-Aldrich. Uranyl acetate was purchased from Electron Microscopy Sciences. All chemicals were used as received.

### 4.2.2 Infusion of Abm into RCNMV capsid

RCNMV suspensions were adjusted to a concentration of 6.43 mg ml<sup>-1</sup> in 20 mM sodium phosphate buffer pH 7.5 with 20 mM EDTA or without EDTA. The suspensions were equilibrated for 1 hour to induce the pore-open condition on the exterior of the virus capsid prior to loading Abm. Next, a 2 mg/ml Abm solution was added at a molar ratio of 510:1 Abm to virion (the molecular weight of RCNMV is 1×10<sup>7</sup> g mol<sup>-1</sup>) and then gently mixed overnight to allow the complete infusion of Abm. At the end of the infusion period, 25 mM CaCl<sub>2</sub> was added, the pH lowered by addition of 0.2 M sodium acetate buffer pH 5.2, and incubated for an additional 30 minutes to close the pores on the viral capsid. Excess Abm molecules were removed by running the loaded RCNMV through a size exclusion column (NAP<sup>TM</sup> 10 columns, GE Healthcare), and Abm-loaded RCNMV, named as plant viral nanoparticle (PVN<sup>Abm</sup>), were

collected in 0.2 M sodium acetate buffer pH 5.2. The concentration of PVN<sup>Abm</sup> was measured with a NanoDrop 1000 Spectrophotometer at 260 nm with an extinction coefficient (1 cm light path) of 6.46. PVNs were also dually formulated with Abm and fluorescent dye rhodamine (PVN<sup>Rho/Abm</sup>) to allow for tracking of PVNs in the mobility testing.

#### 4.2.3 Physical characterization of PVN<sup>Abm</sup>

The morphology of native RCNMV and PVN<sup>Abm</sup> was analyzed using TEM with negative staining (JEOL 100S TEM). A 5  $\mu$ l sample ( $\sim$ 1 mg ml<sup>-1</sup>) was deposited onto a copper mesh grid (Formvar/Carbon 400 mesh Cu grid, Ted Pella, Inc.) and wicked off after a 20 second immersion using Whatman filter paper. A 10  $\mu$ l drop of 2% uranyl acetate solution (w v<sup>-1</sup>) was applied and removed after 20 seconds. The prepared grid was vacuum dried for 30 minutes and stored in a desiccation chamber before TEM observations.

Hydrodynamic diameter ( $d_H$ ) of RCNMV and PVN<sup>Abm</sup> was measured in acetate buffer pH 5.2 and M9 buffer pH 7.4 via dynamic light scattering using a Zetasizer Nano ZS instrument (Malvern Instruments). The measurements were conducted in a 4.5 ml disposable cuvette, where the Brownian motion of molecules in solution were detected by the fluctuations of the scattering intensity and then correlated to hydrodynamic size via the Stokes-Einstein equation.<sup>[17]</sup> The particle concentration was 0.2 mg ml<sup>-1</sup> for all measurements.

The integrity of RCNMV and PVN<sup>Abm</sup> were also analyzed by gel electrophoresis. Briefly, a 5  $\mu$ l aliquot of sample was mixed with 1  $\mu$ l of bromophenol blue loading dye (6X), and then run in 1% HEE0 agarose gel in 0.2M sodium acetate buffer pH 5.2 at 40 volt for 2 hours. The gel was stained with 2  $\mu$ g ml<sup>-1</sup> ethidium bromide in 0.2M sodium acetate buffer pH 5.2 and

then destained with deionized (DI) water for 10 minutes before taking image under UV transilluminator (UVP BioImage Systems).

#### 4.2.4 Quantitation of Abm in PVN<sup>Abm</sup> by HPLC

##### *a. Derivatization reaction*

PVN<sup>Abm</sup> was disassembled with 2 mg ml<sup>-1</sup> proteinase K and 2% (w v<sup>-1</sup>) SDS solution to release all loaded Abm. Subsequently, an 80 µl of disassociated mixture and standard Abm solutions at concentration of 100, 40, 20, 10, 2 µg ml<sup>-1</sup> were dried under vacuum for 1 hours until all liquid were evaporated. The dry residues were re-dissolved in 80 µl anhydrous acetonitrile (ACN), and then mixed with 200 µl N-methylimidazole (NMIM) solution in ACN (1:1, v/v). To initiate the derivatization reaction, 200 µl of trifluoroacetic anhydride (TFAA) solution in ACN (1:1, v/v) were added. After 1-minute vortex mixing, a 10 µl aliquot of glacial acetic acid was added into the mixture, which were then placed in a 55 °C water bath for 30 min. The native RCNMV was also disassembled and derivatized as a negative control to test if it interferes with the HPLC assay. All derivatized solutions were transferred to the 2 ml autosampler vials (Agilent Technologies) for HPLC analysis.

##### *b. HPLC procedures, PVN<sup>Abm</sup> loading capacity and loading efficiency*

The HPLC system consisted of an Infinity model 1260 HPLC pump (Model G1312B, Agilent Technologies), a standard autosampler (Model G1329B, Agilent Technologies) and a fluorescence detector (Model G1321B, Agilent Technologies). The separation was carried out on Agilent Poroshell 120 EC-C18 column (3.0 mm x 100 mm, 2.7µm particle size) at a temperature of 40°C. The mobile phase was 95 % ACN (v v<sup>-1</sup>) at the flow rate of 1.00 ml min<sup>-1</sup>,

and the injection volume of sample was 5  $\mu\text{l}$ . The fluorescence detection was set to monitor an excitation wavelength of 365 nm and an emission wavelength of 470 nm. HPLC analysis was conducted within 6 hours to avoid the degradation of the Abm derivatives. The peak areas were plotted against the Abm standard concentrations to establish the calibration curve using the least square linear regression analysis in OriginPro 8.5 data processing software (OriginLab<sup>®</sup>). The amount of loaded Abm in each PVN<sup>Abm</sup> formulation was calculated based on the standard calibration curve, while the concentration of PVN<sup>Abm</sup> was measured with a NanoDrop 1000 Spectrophotometer at 260 nm with an extinction coefficient (1 cm light path) of 6.46.<sup>[18]</sup> The loading capacity (LC) of PVN<sup>Abm</sup> reported as the number of Abm molecules associated with each viral capsid and loading efficiency (LE) represented as the percentage of the Abm loaded with respect to the initial amount of Abm added to the loading preparation were calculated as follows:

$$LC = (\text{weight}_{Abm \text{ loaded}} / \text{weight}_{PVN \text{ capsid}}) \times (mw_{PVN \text{ capsid}} / mw_{Abm}) \quad (1)$$

$$LE = (\text{weight}_{Abm \text{ loaded}} / \text{weight}_{total \text{ of added Abm}}) \times 100\% \quad (2)$$

where  $mw_{virion}$  and  $mw_{Abm}$  are the molecular weights of the virion at  $1 \times 10^7 \text{ g mol}^{-1}$  and Dox at  $837.11 \text{ g mol}^{-1}$ , respectively.

#### 4.2.5 *In vitro* Release profiles of PVN<sup>Abm</sup>

A dialysis-based assay was carried out to study the *in vitro* release performance of Abm molecules from PVN<sup>Abm</sup>. A 180  $\mu\text{l}$  aliquot of PVN<sup>Abm</sup> suspension or free Abm solution at equivalent concentrations was injected into a dialysis bag with a MWCO of 3.5 kDa

(Spectra/Por®, Spectrum Laboratories, Inc.). The dialysis bag was immersed in 10 ml release medium containing either sodium acetate buffer (20 mM, pH 5.2) or M9 buffer (pH 7.4). At set intervals, the PVN<sup>Abm</sup> suspension or free Abm solution were taken out from dialysis bag and the concentration of remaining Abm was determined by derivatization-HPLC methods as described above. Fresh release medium was replaced at every interval to maintain a constant sink condition. The release of PVN<sup>Abm</sup> sample was run in triplicate. The integrity of released PVN<sup>Abm</sup> at different time points was measured by gel electrophoresis.

#### **4.2.6 Bioavailability of PVN<sup>Abm</sup> to *C. elegans* nematodes**

The bioavailability of PVN<sup>Abm</sup> and free Abm was assayed utilizing model nematodes *Caenorhabditis elegans* (*C. elegans*) in the liquid culture as described previously.<sup>[19]</sup> A 5 µl aliquot of PVN<sup>Abm</sup> with the Abm concentrations (1.8 ug ml<sup>-1</sup>, 0.60 ug ml<sup>-1</sup>, 0.20 ug ml<sup>-1</sup>, 0.07 ug ml<sup>-1</sup>), and free Abm at concentrations (2.0 ug ml<sup>-1</sup>, 0.67 ug ml<sup>-1</sup>, 0.22 ug ml<sup>-1</sup>, 0.07 ug ml<sup>-1</sup>) were added to each well of 24-well culture plate, which was subsequently loaded with *C. elegans* nematodes (~ 50 individuals) cultured in 495 µl M9 buffer. After 24-hours incubation at room temperature, the dead nematodes in each well were determined as the loss of mobility and characteristics of a rigid, linear appearance. All experiments were run in triplicate. The LC50 values, representing 50 % lethality at a given concentration of Abm, were reported for free Abm solution and PVN<sup>Abm</sup> suspension.

#### **4.2.7 Soil mobility of PVN<sup>Abm/Rho</sup> and free ABM/Rho**

PVN<sup>Abm/Rho</sup>, dually formulated with Abm and rhodamine dye, was used to allow for tracking the fraction of PVN throughout the soil via fluorescent detection. The soil mobility

test was designed based on Organisation for Economic Cooperation and Development (OECD) guideline for leaching detection in a soil column.<sup>[20]</sup> Briefly, two soil types (sandy loam soil and potting soil) were packed in a plastic column to a height of 4 cm. Subsequently, the soil was saturated with 5 ml DI water. A 300 µl aliquot of PVN<sup>Abm/Rho</sup> or Abm/Rho mixture solution was applied on the top of the soil columns. Next, 24 aliquots of 300 µl DI water were added to elute through the soil column and collected individually a well of a 24-well plate. Each collected fraction was assayed for presence of test sample by measuring 1) fluorescence of Rho at the excitation wavelength of 530 nm and emission wavelength of 530; and 2) bioavailability of Abm to *C. elegans* cultures as described above.

#### **4.2.8 Crop protection of PVN<sup>Abm</sup> to plant parasitic nematode-infected tomato plants**

PVN<sup>Abm</sup> and free Abm were applied to test the prevention of Root knot nematode (RKN) *Meloidogyne hapla* in the 6-ounce foam cup under greenhouse condition. The cups were filled with sandy loam soil and pre-wetted prior to transplanting. Two-week-old tomato seedlings that had uniform growth were selected for planting in the soil-filled cups and dosed with RKN inoculum (5000 eggs in 1 ml per cup) through three holes surrounding the root. Subsequently, a total amount of 0.8 mg Abm in PVN<sup>Abm</sup> suspension or free Abm solution was applied in each plant. Healthy plants without infection were taken as the negative control. The infected plants without Abm treatment were taken as the positive control. Each treatment was run in triplicate, and the plants were watered as needed in the greenhouse. After 5 weeks of RKN inoculation, the roots of plants were harvested and gently washed with tap water. The galling on the root

and the growth of the root were evaluated in each treatment to determine the efficacy of crop protection.

### 4.3 Results and Discussion

#### 4.3.1 Infusion of Abm into RCNMV and Characterization

The previous studies have demonstrated that RCNMV's structure and unique response to divalent cation depletion and re-addition enables positively charged or neutral charged small molecules to infuse into the viral capsid through a pore formation mechanism.<sup>[18, 21]</sup> Using this feature, RCNMV has been developed as a nano-vessel to carry the chemotherapeutic drug, doxorubicin, to fight against cancer.<sup>[22]</sup> In this study, we explored the advantage of RCNMV as a drug delivery system to enable efficacious delivery and tunable release of nematicides for plant-parasitic nematode control in agriculture application. A neutrally charged bio-nematicide, abamectin (Abm), was loaded into RCNMV in phosphate buffer pH 7.5 with 20 mM EDTA treatment to make a Abm-loaded plant viral nanoparticle (PVN<sup>Abm</sup>). TEM imaging of PVN<sup>Abm</sup> (**Figure 4.1a**) displays an intact viral capsid and shows a similar surface morphology on the capsid when compared with that of native RCNMV (**Figure 4.1b**). The hydrodynamic diameter ( $d_H$ ) of PVN<sup>Abm</sup> is 37.6 nm and its polydispersity index of 0.231 are the same as native RCNMV (**Figure 4.1c** and **Figure 4.1d**); confirming that the infusion of Abm did not result in a detectable change in the viral capsid integrity. In our previous study on doxorubicin (Dox)-loaded PVN (PVN<sup>Dox</sup>), a larger  $d_H$  of 42 nm was due to surface-bound Dox on the capsid; whereas for PVN<sup>Abm</sup>, the unchanged  $d_H$  suggests the absence of surface-binding Abm on the viral capsid.

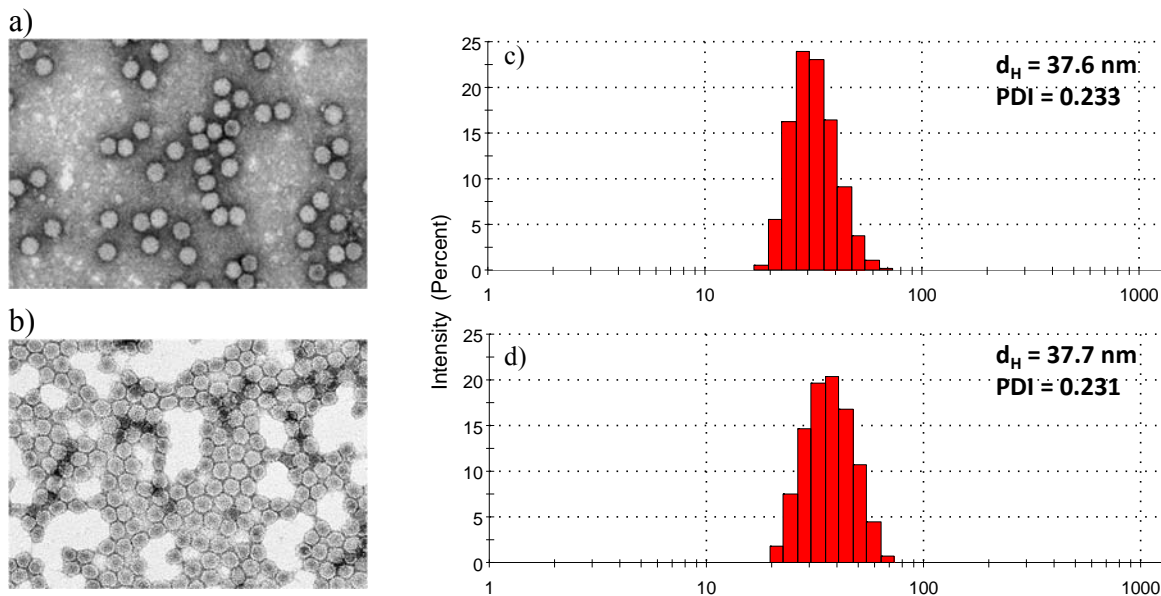


**Figure 4.1** Characterization of native RCNMV and corresponding plant viral nanoparticle via transmission electron microscopy for a) RCNMV prior to loading, b) after loading with Abm ( $PVN^{Abm}$ ); Size distribution as measured by dynamic light scattering for hydrodynamic diameter ( $d_H$ ) and polydispersity index (PDI) of c) RCNMV and d)  $PVN^{Abm}$ . \* All RCNMV and  $PVN^{Abm}$  were measured in sodium acetate buffer pH 5.2.

### 4.3.2 Quantitation of Abm in $PVN^{Abm}$ by HPLC

To quantitatively determine the amount of Abm infused in viral capsid,  $PVN^{Abm}$  was disassembled by proteinase digestion to release all loaded Abm. Subsequently, according to the study by Payne et al.' study,<sup>[23]</sup> the disassembled mixture was subjected to a derivatization reaction to convert Abm compounds to a fluorescent derivatives. As shown in **Figure 4.2**, the mechanism of derivatization reaction is to dehydrate the dihydroxycyclohexane ring of Abm to form an aromatic fluorescent moiety.<sup>[24]</sup> The separation of Abm derivatives was achieved by HPLC with fluorescence detection. The representative chromatogram of Abm derivative from a standard Abm concentration is shown in **Figure 4.3a**. There are two distinctive peaks,

however, only a peak at an elution time of 3.812 minutes responds proportionally to different standard Abm concentrations. The chromatogram of Abm derivative from PVN<sup>Abm</sup> displays a similar pattern as the standard Abm solutions; suggesting that PVN<sup>Abm</sup> capsid have been properly digested and the loaded Abm have been fully recovered (**Figure 4.3b**). In addition, the chromatogram of RCNMV control, that underwent the same dissociation and derivatization reactions as PVN<sup>Abm</sup>, didn't have the feature peak of Abm derivative (**Figure 4.3c**); indicating that digested RCNMV protein subunits and chemical reagents have no interference with this established HPLC assay. The calibration curve for this HPLC assay was linear over the Abm concentration range of 2 – 100 ( $\mu\text{l ml}^{-1}$ ) with a regression coefficient of 3.12 ( $\text{mAU s } \mu\text{g}^{-1} \text{ ml}$ ) and a correlation coefficient of 0.99 (**Figure 4.3d**).

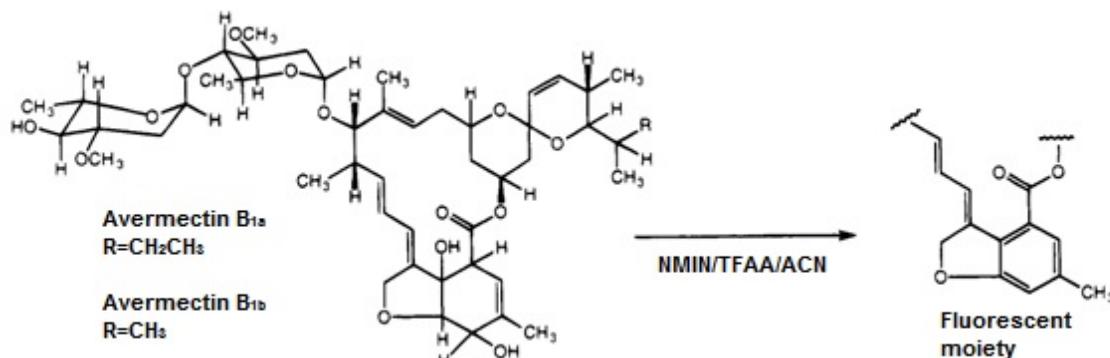


**Figure 4.2** Structures of abamectin (mixture of  $\geq 80\%$  B<sub>1a</sub> homolog and  $\leq 20\%$  B<sub>1b</sub> homolog) and its fluorescent derivatives.<sup>[24]</sup>

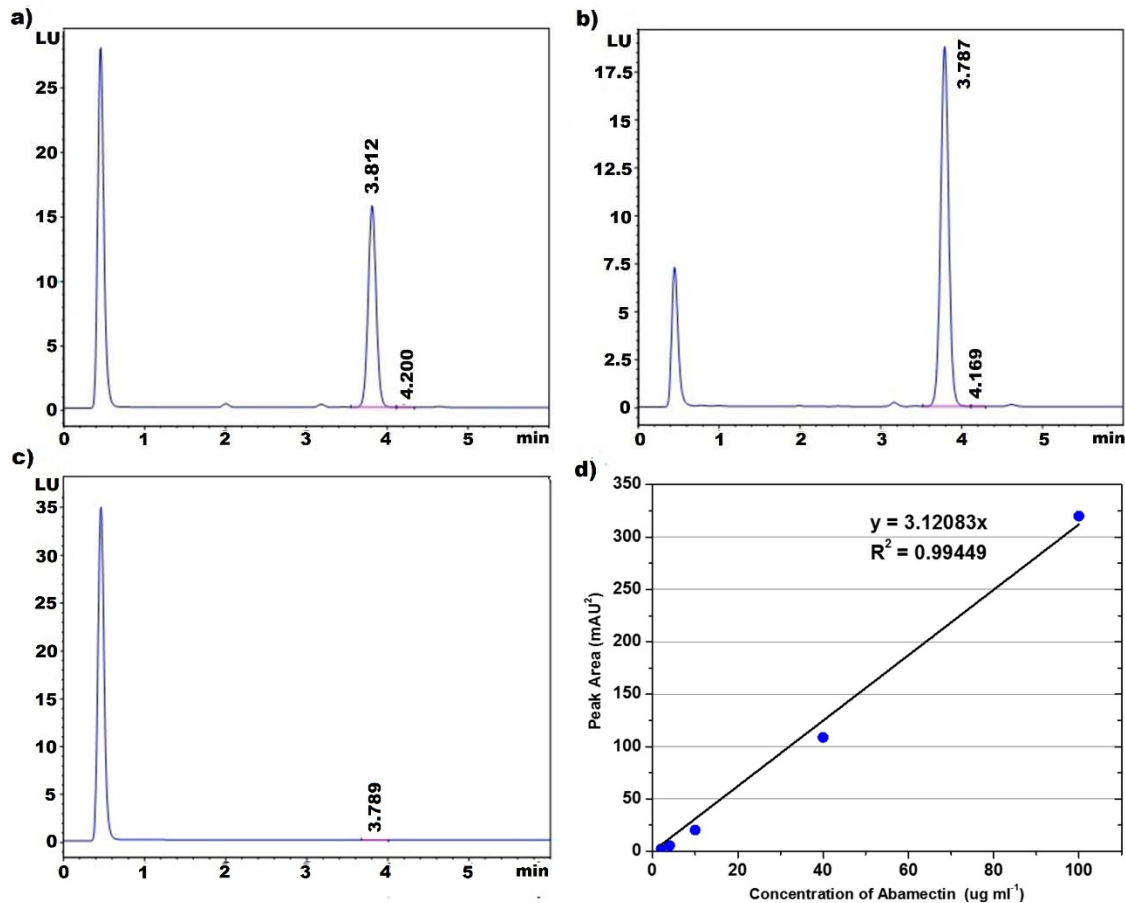


**Figure 4.3** HPLC assay for quantitation of Abm in PVN<sup>Abm</sup>. HPLC chromatograms of a) standard Abm solution at concentration of 40 µg/ml, b) PVN<sup>Abm</sup> and c) native RCNMV via fluorescence detector at excitation wavelength of 365 nm and emission wavelength of 470 nm; d) HPLC calibration curve based on the standard concentrations versus the peak area around the elution time of 3.8 minutes.

By using the established HPLC methods, the loading properties of PVN<sup>Abm</sup> were quantified as listed in **Table 4.1**. For the PVN<sup>Abm</sup> formulated in phosphate buffer pH 7.4 with 20 mM EDTA, there was approximately 37.2 µg of Abm loaded into 1 mg PVN<sup>Abm</sup>, amounting to a loading capacity (LC) of ~177 Abm molecules loaded to each RCNMV capsid. The load efficiency (LE), the percentage of the Abm loaded with respect to the initial amount of Abm added to the loading preparation, was around 34.9 %. To study the possibility of surface-bound

Abm on RCNMV capsid, the PVN<sup>Abm</sup> was also formulated in the same buffer and pH value but without EDTA treatment. Our hypothesis is that the pore-open condition has to be induced by the loss of Ca<sup>2+</sup> and Mg<sup>2+</sup> divalent ions via exposing RCNMV to EDTA as a chelating agent. Therefore, any loading of Abm in the absence of EDTA could be considered as surface-bound molecules with RCNMV capsid. The results indicated that this surface association between Abm and RCNMV capsid is negligible as evident by the PVN<sup>Abm</sup> formulation without EDTA treatment where only ~0.24 µg Abm in 1 mg PVN was loaded, which was equivalent to a LC of less than 1 Abm molecule per RCNMV capsid (**Table 4.1**). Unlike the PVN<sup>Dox</sup> with a certain amount of surface-bound Dox molecules due to the electrostatic interaction between the positively charged Dox and negatively charged RCNMV capsid surface at pH 7.5, the neutral Abm molecules were not likely to be electrostatically attracted onto the capsid surface, but only infused into the RCNMV capsid through the open pores on the capsid. Therefore, we infer that all ~177 Abm molecules were encapsulated within a RCNMV capsid rather than surface binding on the capsid.

**Table 4.1** Loading properties of PVN<sup>Abm</sup> suspensions formulated at phosphate buffer pH 7.5 with different EDTA concentrations.

PVN <sup>Abm</sup> Formulations	Abm Load <sup>a)</sup> (µg)	Load Capacity <sup>b)</sup> (Abm /capsid)	Load Efficiency <sup>c)</sup> (%)
no/ EDTA	0.24 ± 0.03	< 1	–
20 mM EDTA	37.2 ± 1.8	177 ± 9	34.9 ± 1.7

<sup>a)</sup>Amount of abamectin (µg) loaded in 1 mg PVN<sup>Abm</sup>; <sup>b)</sup>Load capacity (LC) reported as the number of abamectin associated with each viral capsid; <sup>c)</sup>Load efficiency (LE) reported as the percentage of the abamectin loaded to the initial amount of abamectin used in preparation.

### 4.3.3 In vitro release profiles

The *in vitro* release performance of PVN<sup>Abm</sup> was investigated in the sodium acetate buffer pH 5.2 and M9 buffer pH 7.4 at room temperature. The pH values were selected to represent the acidic soil condition (pH 5.2) and the physiological condition of nematode (pH 7.4). As shown in **Figure 4.4a**, a 95 % of free Abm was diffused out of the dialysis bag within the first 5 hours. In contrast, the rate of Abm release was considerably retarded by the PVN<sup>Abm</sup> as only 24% and 28% of loaded Abm were released from PVN<sup>Abm</sup> in pH 5.2 and pH 7.4 release mediums, respectively, within 5 hours (**Figure 4.4b**). PVN<sup>Abm</sup> exhibited an initial release of 16% loaded Abm in pH 7.4 medium within the first 1 hour, then gradually release of 96% loaded Abm in following 12 hours. However, in pH 5.2 release medium, no release of PVN<sup>Abm</sup> was detected in the first 1 hour but 91% loaded Abm was still gradually released from PVN<sup>Abm</sup> in 12 hours with a slightly lower rate of release when compared with its release in pH 7.4 medium. Almost complete release of all loaded Abm was achieved for PVN<sup>Abm</sup> in both release mediums within 24 hours. This is because the encapsulated Abm molecules were only physically entrapped by RCNMV capsid rather than strongly associated with RCNMV nucleic acids, such as Dox-RNAs intercalation in PVN<sup>Dox</sup>. As a result, PVN<sup>Abm</sup> displayed a fast and complete release of encapsulated Abm from the capsid due to the chemical potential gradient in the release study. In addition, as shown in **Figure 4.5**, all released PVN<sup>Abm</sup> show the ethidium bromide (EtBr) stained virion bands at the same position as unreleased PVN<sup>Abm</sup> and native RCNMV on the electrophoresis gel, indicating the integrity of PVN<sup>Abm</sup> capsid at all release times.

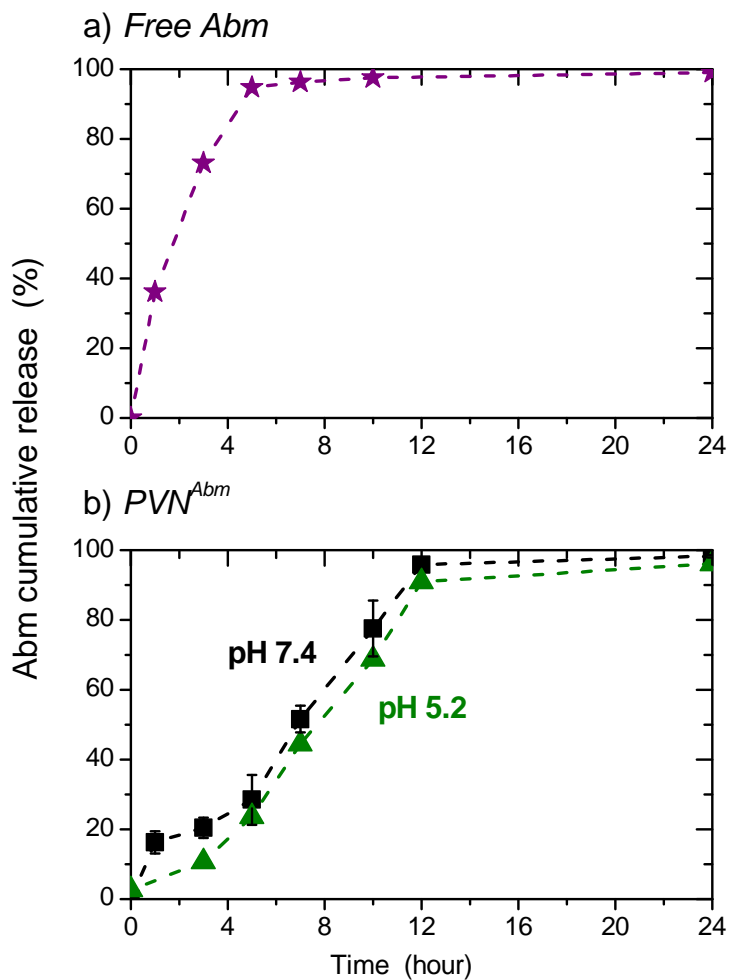


**Figure 4.4** Cumulative Abm release over time for a) free Abm dialyzed in acetate buffer pH 5.2 (★) and b) PVN<sup>Abm</sup> dialyzed in acetate buffer pH 5.2 (▲) and M9 buffer pH 7.4 (■). The lines are guides for the eye.

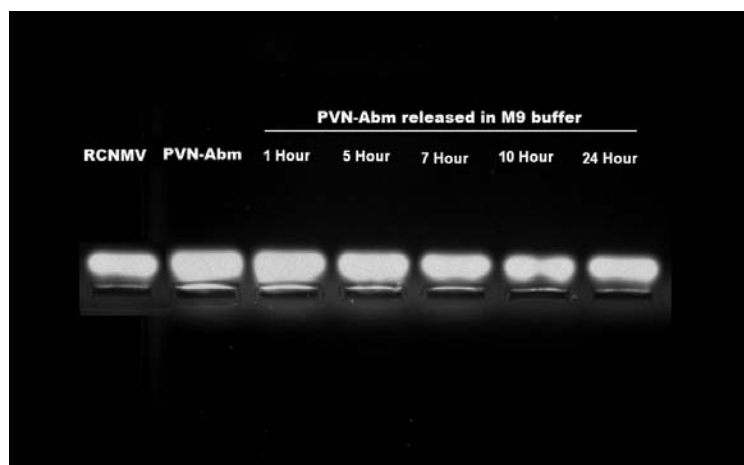


**Figure 4.5** Agarose gel electrophoresis of native RCNMV, PVN<sup>Abm</sup>, and released PVN<sup>Abm</sup> in M9 buffer pH 7.4 after different times of release. Gel were visualized under UV light after ethidium bromide staining.

#### 4.3.4 Bioavailability of PVN<sup>Abm</sup> to *C. elegans* nematode

Bioavailability of PVN<sup>Abm</sup> was evaluated against free Abm in a bioassay utilizing the model nematode *C. elegans* nematode in the liquid culture. Abm acts as a paralytic with exposed nematodes displaying a rigid, linear appearance and a characteristic loss of mobility versus the flexible form and undulating movement exhibited by untreated nematodes. *C. elegans* cultures were directly dosed over a range of concentrations with either free Abm or PVN<sup>Abm</sup>, and assayed as three scales: totally mobilized, impaired (50/50 mobilized/immobilized) and totally immobilized. The result of LC50 values, representing a given concentration of Abm at which the nematodes were impaired, only shows a slight difference between the free Abm (LC50 of  $1.5 \pm 0.4 \times 10^{-7}$  M) and PVN<sup>Abm</sup> (LC 50 of  $1.3 \pm 0.6 \times 10^{-7}$  M). This was consistent with the *in vitro* release result that all Abm were released from

PVN<sup>Abm</sup> in 24 hours and so they have equivalent bioavailability as free Abm in *C. elegans* culture.

#### 4.3.5 Improved soil mobility of Abm by PVN carrier

In order to determine whether the PVN<sup>Abm</sup> carrier was able to mobilize Abm within the soil, RCNMV were dually formulated with Abm and rhodamine (Rho) dye to form the PVN<sup>Abm/Rho</sup>, which provides an additional approach for tracking PVN's mobility through the soil by fluorescence from the loaded Rho. PVN<sup>Abm/Rho</sup> and mixture of free Abm and Rho (Abm/Rho) were applied to the soil column containing potting soil or sandy loam soil, and then eluted by addition of 24 aliquots of DI water. The 24 fractions of collected efflux were assayed for the presence of tested samples by measuring the fluorescence of Rho as well as the bioavailability of Abm to *C. elegans* nematode. As shown in **Figure 4.6a**, the efflux of Abm/Rho mixture from the soil column presented the low fluorescent intensity and low toxicity to nematodes; indicating the poorly mobility of Abm/Rho in both two soil types, especially in sandy loam soil. The higher retention of Abm/Rho mixture in the soil might be attributed by their higher affinity to bind to the organic compounds in the soil due to their hydrophobic nature.<sup>[10]</sup> In contrast, PVN<sup>Rho/Abm</sup> was able to significantly mobilize the loading cargos of Rho and Abm in either sandy loam or potting soil as evident by the increased fluorescent intensity and nematode toxicity of their efflux (**Figure 4.6b**). While Abm encapsulated in PVN was successfully mobilized in soil, the degree of mobility was varied in two tested soil types; suggesting that the surface chemistry of PVNs may require adjustment for different soil types.

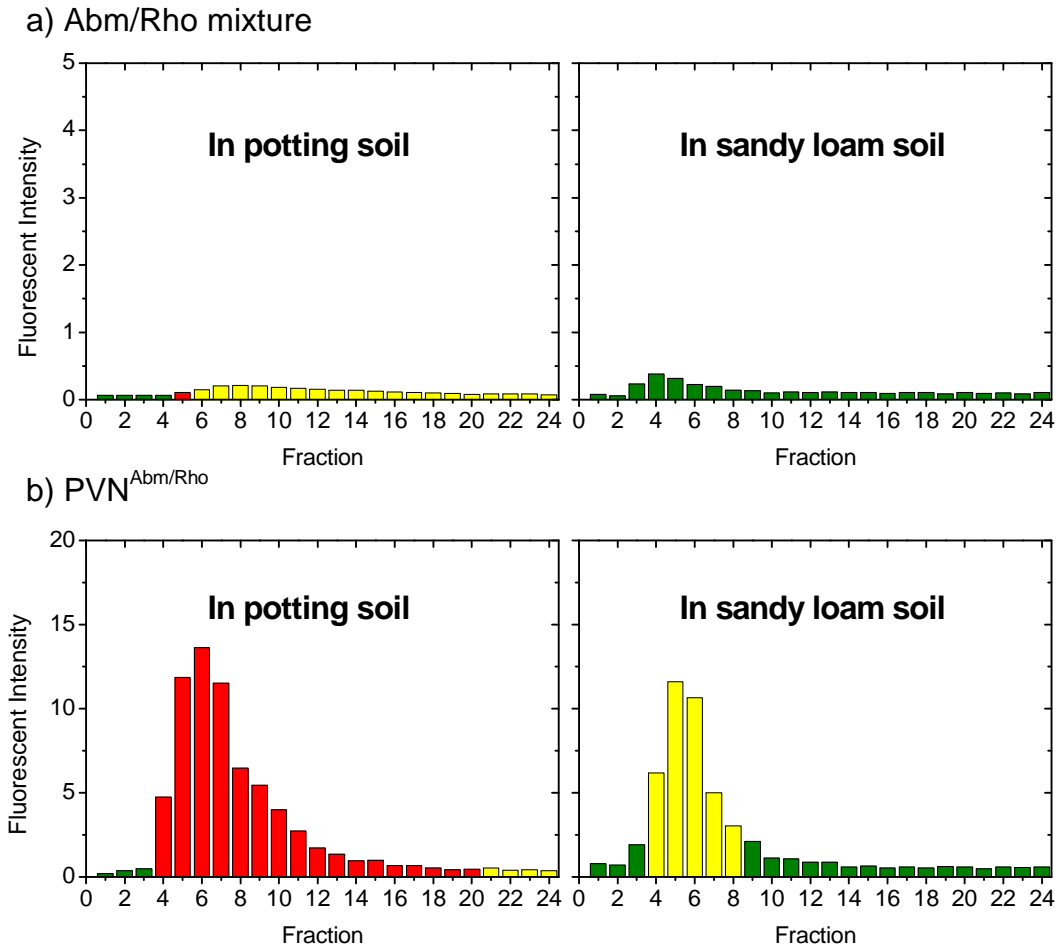


**Figure 4.6** Characterization of soil mobility for a) Abm/Rho mixture and b) PVN<sup>Abm/Rho</sup> and in the potting soil and sandy loam soil via the fluorescence intensity of Rho molecules and the bioavailability of Abm molecules to cause *C. elegans* nematodes to be mobilized (■), impaired (■) and immobilized(■).

#### 4.3.6 Improved nematicide performance of Abm in soil by PVN carrier

Abm has a high tendency to bind to the organic carbon contents in the soil,<sup>[10, 11]</sup> which promises its nematicide performance due to the less distribution of Abm in the nematode infected soil. Previous studies were inconclusive with regard to whether hydrophobic partitioning or more specific interactions are involved in sorption of Abm because it was

dependent on the specific physical chemistry of Abm in different soil conditions.<sup>[25, 26]</sup> In this study, we manipulated the Abm's physical chemistry in the soil via encapsulate Abm into a PVN carrier. The nematicide efficacy of PVN<sup>Abm</sup> against free Abm was tested in the tomato seedlings that were infected with Root knot nematode (RKN) *Meloidogyne hapla* in the sandy loam soils. After 5 weeks of RKN inoculation, the crop protection effect of PVN<sup>Abm</sup> and free Abm was evaluated by root growth and gallings on roots in the basis of 0 – 4 unit-scales. As listed in **Table 4.2**, the uninfected plant as a negative control has score of zero for its optimum root growth and score of zero for no galling on the root (**Figure 4.7a**). In contrast, the positive control of RKN-infected plant had the worst score of 4 for both root growth and root galling due to the less root growth and lots of galling on the root. (**Figure 4.7b**). Compared to positive control, applying free Abm in the RKN-infected soil didn't shown an effective prevention of RKN damage as evident by a very slight improvement in root growth (score of 3) and root galling (score of 3.75) of RKN-infected tomato seedlings (**Figure 4.7c**). However, the PVN<sup>Abm</sup> exhibited a significant enhancement in nematode control, which has score of 2.0 for root growth and score of 2.8 for root galling. As shown in **Figure 4.7d**, PVN<sup>Abm</sup> treated infected plants displayed the reduced number of gallings on the top part of plant root while a heavy RKN infection were still occurred on the bottom part of the root; indicating that applying PVN<sup>Abm</sup> in surrounding RKN-infected soil had protected the top part of plant root but not effective to the bottom part of the root. The reduced efficacy in the lower portion of the root could be caused by the limited mobility of PVN<sup>Abm</sup> in sandy loam soil. To achieve a complete protection, engineering the surface chemistry of PVN capsid to further increase its mobility in the soil would be necessary.

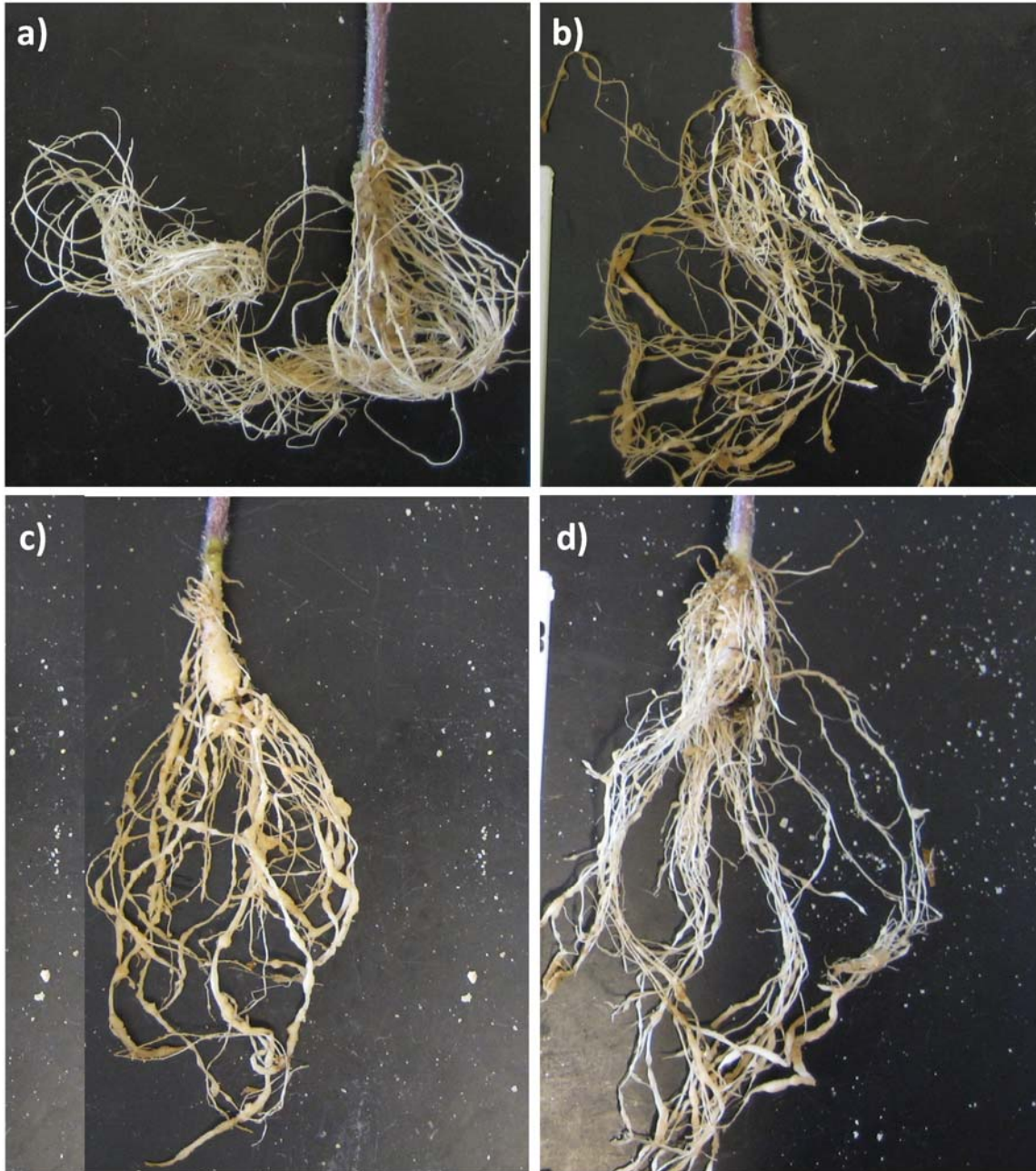


**Figure 4.7** Evaluation of root system for a) uninfected tomato seedling; b) *Meloidogyne hapla* root knot nematode (RKN) infected tomato seedling; c) RKN-infected tomato seedlings treated with free Abm and d) RKN-infected tomato seedling treated with PVN<sup>Abm</sup>. All plants were growth in greenhouse for 5-weeks after treatment.

**Table 4.2** Crop protection results of Abm and PVN<sup>Abm</sup> to tomato seedlings infected with *Meloidogyne hapla* root knot nematode (RKN) in greenhouse.

Evaluation	Uninfected plant	RKN-Infected plant		
		control	Free Abm	PVN <sup>Abm</sup>
Root growth index <sup>a</sup>	0	4.0	3.0	2.0
Root galling index <sup>b</sup>	0	4.0	3.7	2.8

<sup>a</sup> Plant root growth index were determined at 5 weeks after treatment, using a 0 - 4 unit scale where 0 = optimum growth of uninfected plant and 4 = worst root growth of the infected plant

<sup>b</sup> Nematode root galling index determined at 5 weeks after treatment, obtained using a 0 – 4 unit scale where 0 = no galling of uninfected plants and 4 = worst galling of infected plants. Data were reported by means of three replications.

#### 4.4 Conclusion

Abamectin is a soil-immobile pesticide that has a high nematicide activity against a wide variety of important plant parasitic nematodes in a large number of crops. However, its poor mobility within the soils compromises its nematicide performance due to the limited zone of protection surrounding the growing plants. In this study, we manipulated the Abm's physical chemistry in the soil via encapsulating Abm into a RCNMV-derived PVN carrier. The increased soil mobility of Abm demonstrated a very close correlation to the success of nematode control. Compared to free Abm, the improved soil mobility of Abm by formulated PVN<sup>Abm</sup> effectively enhanced its crop protection for nematode control as evident by the healthier root growth and the reduced the root gallings on nematode-infected tomato plants. However, PVN<sup>Abm</sup> had a reduced efficacy of nematode control in the bottom of infected plant's root system. This may be attributed by the constraint on the movement of PVN in the tested soil or the reduced amount of Abm in the PVN due to leakage of encapsulated Abm. In future work, the exterior surface of PVN capsid can be engineered by conjugating with hydrophilic

chemical moieties to increase its mobility in the soil or coupling with targeting peptides for specific delivery into nematodes. The interior protein subunits of PVN capsid also can be modified to bind with Abm to further tune its release profiles.

#### **4.5 References**

- [1] P. Abad, J. Gouzy, J. Aury, P. Castagnone-Sereno, E. Danchin, E. Deleury, L. Perfus-Barbeoch, V. Anthouard, F. Artiguenave, V. Blok, M. Caillaud, P. Coutinho, C. Dasilva, F. De Luca, F. Deau, M. Esquibet, T. Flutre, J. Goldstone, N. Hamamouch, T. Hewezi, O. Jaillon, C. Jubin, P. Leonetti, M. Magliano, T. Maier, G. Markov, P. McVeigh, G. Pesole, J. Poulain, M. Robinson-Rechavi, E. Sallet, B. Ségurens, D. Steinbach, T. Tytgat, E. Ugarte, C. van Ghelder, P. Veronico, T. Baum, M. Blaxter, T. Bleve-Zacheo, E. Davis, J. Ewbank, B. Favery, E. Grenier, B. Henrissat, J. Jones, V. Laudet, A. Maule, H. Quesneville, M. Rosso, T. Schiex, G. Smant, J. Weissenbach, P. Wincker, Genome sequence of the metazoan plant-parasitic nematode *Meloidogyne incognita*, *Nature Biotechnology*, 26 (2008) 909-915.
- [2] J. Sasser, Root-knot nematodes: a global menace to crop production, *Plant Disease*, 64 (1980) 36-41.
- [3] C.J. Nusbaum, H. Ferris, The Role of Cropping Systems in Nematode Population Management, *Annual Review of Phytopathology*, 11 (1973) 423-440.
- [4] R. Cook, Genetic resistance to nematodes: where is it useful?, *Australasian Plant Pathology*, 33 (2004) 139-150.

- [5] R. Sikora, E. Fernandez, Nematode parasites of vegetables., in: M. Luc, R. Sikora, J. Bridge (Eds.) Plant parasitic nematodes in tropical and subtropical agriculture, 2nd edition, CABI Publishing Wallingford, UK, 2005, pp. 319-392.
- [6] B.M. Santos, J.P. Gilreath, T.N. Motis, J.W. Noling, J.P. Jones, J.A. Norton, Comparing methyl bromide alternatives for soilborne disease, nematode and weed management in fresh market tomato, *Crop Protection*, 25 (2006) 690-695.
- [7] A.M. Stirling, G.R. Stirling, I.C. Macrae, Microbial Degradation of Fenamiphos After Repeated Application To a Tomato-Growing Soil, *Nematologica*, 38 (1992) 245-254.
- [8] I. Putter, J.G.M. Connell, F.A. Preiser, A.A. Haidri, S.S. Ristich, R.A. Dybas, Avermectins: novel insecticides, acaricides and nematicides from a soil microorganism, *Experientia*, 37 (1981) 963-964.
- [9] M.J. Turner, J.M. Schaeffer, Mode of action of Ivermectin, in: W.C. Campbell (Ed.) Ivermectin and abamectin, Springer, New York, USA, 1989, pp. 73-88.
- [10] K.A. Krogh, T. Søbørg, B. Brodin, B. Halling-Sørensen, Sorption and Mobility of Ivermectin in Different Soils All rights reserved. No part of this periodical may be reproduced or transmitted in any form or by any means, electronic or mechanical, including photocopying, recording, or any information storage and retrieval system, without permission in writing from the publisher, *J. Environ. Qual.*, 37 (2008) 2202-2211.
- [11] V.F. Gruber, B.A. Halley, S.C. Hwang, C.C. Ku, Mobility of avermectin B1a in soil, *Journal of Agricultural and Food Chemistry*, 38 (1990) 886-890.
- [12] J.A. Cabrera, R.D. Menjivar, A.e.-F.A. Dababat, R.A. Sikora, Properties and Nematicide Performance of Avermectins, *Journal of Phytopathology*, 161 (2013) 65-69.

- [13] A.C. Chukwudebe, W.F. Feely, T.J. Burnett, L.S. Crouch, P.G. Wislocki, Uptake of Emamectin Benzoate Residues from Soil by Rotational Crops, *Journal of Agricultural and Food Chemistry*, 44 (1996) 4015-4021.
- [14] H. Mrozik, Advances in Research and Development of Avermectins, in: *Natural and Engineered Pest Management Agents*, American Chemical Society, 1993, pp. 54-73.
- [15] V.R. Basnayake, T.L. Sit, S.A. Lommel, The genomic RNA packaging scheme of Red clover necrotic mosaic virus, *Virology*, 345 (2006) 532-539.
- [16] L. Loo, R.H. Guenther, S.A. Lommel, S. Franzen, Infusion of dye molecules into Red clover necrotic mosaic virus, *Chem. Commun. (Cambridge, U. K.)*, (2008) 88-90.
- [17] A. Ferrer, E. Quintana, I. Filpponen, I. Solala, T. Vidal, A. Rodríguez, J. Laine, O. Rojas, Effect of residual lignin and heteropolysaccharides in nanofibrillar cellulose and nanopaper from wood fibers, *Cellulose*, 19 (2012) 2179-2193.
- [18] M.B. Sherman, R.H. Guenther, F. Tama, T.L. Sit, C.L. Brooks, A.M. Mikhailov, E.V. Orlova, T.S. Baker, S.A. Lommel, Removal of divalent cations induces structural transitions in red clover necrotic mosaic virus, revealing a potential mechanism for RNA release, *J. Virol.*, 80 (2006) 10395-10406.
- [19] C.H. Opperman, S. Chang, Effects of Aldicarb and Fenamiphos on Acetylcholinesterase and Motility of *Caenorhabditis elegans*, *Journal of Nematology*, 23 (1991) 20-27.
- [20] OECD, Test No. 312: Leaching in Soil Columns, OECD Publishing, 2004.
- [21] L. Loo, R.H. Guenther, S.A. Lommel, S. Franzen, Encapsulation of nanoparticles by red clover necrotic mosaic virus, *J. Am. Chem. Soc.*, 129 (2007) 11111-11117.

- [22] S. Franzen, S.A. Lommel, Targeting cancer with 'smart bombs': equipping plant virus nanoparticles for a 'seek and destroy' mission, *Nanomedicine (Lond)*, 4 (2009) 575-588.
- [23] L.D. Payne, M.B. Hicks, T.A. Wehner, Determination of Abamectin and/or Ivermectin in Cattle Feces at Low Parts per Billion Levels Using HPLC with Fluorescence Detection, *Journal of Agricultural and Food Chemistry*, 43 (1995) 1233-1237.
- [24] J. W. Tolan, P. Eskola, D. W. Fink, H. Mrozik, L.A. Zimmerman, Determination of avermectins in plasma at nanogram levels using high-performance liquid chromatography with fluorescence detection, *Journal of Chromatography A*, 190 (1980) 367-376.
- [25] J. Tolls, Sorption of Veterinary Pharmaceuticals in Soils: A Review, *Environmental Science & Technology*, 35 (2001) 3397-3406.
- [26] R.A. Bloom, J.C. Matheson III, Environmental assessment of avermectins by the US food and drug administration, *Veterinary Parasitology*, 48 (1993) 281-294.

## **Chapter 5. Nematicide Loaded Lignocellulosic Matrices for Crop Protection**

### **Abstract:**

This chapter has explored the potential use of lignocellulosic materials as the fibrous matrix for sustainable release of agricultural chemicals, such as nematicides. Nematodes cause major damage to seedlings, and so abamectin (Abm)-based seed treatment is the logical and effective method to control nematode infections and damage. However, Abm has a high tendency to bind to the organic carbon contents in the soil, resulting in poor distribution of Abm in nematode infested soil. In this study, we manipulated the Abm's physical chemistry in the soil via incorporating Abm into different lignocellulosic matrix to improve its root-prevention zone. Our results indicate that lignin compounds in the bulk of mechanically pulped banana fibrous matrix appears to work as an adhesive to enable the slow and sustainable release of loaded Abm from the matrices; providing an efficacious delivery of Abm around the plant root to prevent it from plant parasite nematode damage. On the other hand, the lignin-concentrated surface of abaca fibrous matrix remains the loaded Abm on the top surface of matrix, which led to the burst release of Abm and hence compromises the delivery of Abm to the growing root of the plants.

## 5.1 Introduction

Sustainability, eco-friendly and green chemistry were guiding the development of the next generation of materials and products in all fields of industries. Native fibers like cellulose, hemp, flax and silk have already been studied extensively for different kinds of applications such as reinforcement composite, biomaterial, optical media, conductive materials, adhesion and a few to name.<sup>[1-3]</sup> Recently, bio-based polymers and composites derived from renewable biomass or lignocellulose have gained the growing interests to be the alternatives for traditional petroleum-based polymeric materials.<sup>[4]</sup> Lignocellulosic materials, such as wood, grass, and agricultural and forest residues, are the most abundant renewable recourses on the planet, with approximately 200 billion tons produced annually in the world.<sup>[5]</sup> Lignocelluloses are composite biopolymers composing the plant cells, whose main macromolecular constituents are cellulose (35-50%), hemicellulose (20-35%) and lignin (10-25%).<sup>[6]</sup> Cellulose is a long-chain polymer of glucopyranose units with a degree of polymerization ranges from 5,000-10,000. These long chain cellulose molecules build up the microfibril of lignocellulose by hydrogen bonds formed between hydroxyl side groups. These hydrogen bonds stiffen cellulose chains and promote aggregation into a crystalline structure.<sup>[6]</sup> Hemicellulose comprise a lower molecular weight branched polymer (50-300 degree of polymerization) with various monomers including glucose, D-manose, D-galactose, D-xylose and D-arabinose. Hemicellulose is amorphous and hydrophilic in the fiber wall and acts as an interfiber bonding agent to support cellulose microfibrils. Lignin is an amorphous, larger cross-linked phenolic polymer. It consists of three phenylpropane units, namely coniferyl alcohol, sinapyl alcohol, and *p*-coumaryl alcohol, which are linked through a variety of ether and carbon-carbon bonds.

Lignin is relatively hydrophobic due to its aromatic structure and covalently linked to hemicellulose to fill the spaces between microfibrils and/or between fibers in the plant cell wall.<sup>[7]</sup> Apart from these three main polymers, a remaining fraction of lignocellulose were defined as “extractives”, which are organic substances with low molecules weight and are soluble in neural solvents. According to the botanical origin and environmental factors, the lignocellulosic materials present considerably variations in their compositions. The different contents also can vary based on the conditions of the fibers pretreatment (e.g., chemical pulping, mechanical pulping or bleaching).<sup>[7]</sup>

The objective of this study is to explore the potential use of lignocellulosic materials as matrix carrier for loading and sustainable release of agricultural chemicals. Specially, manipulating the change of lignocellulosic fibrous matrix in its chemical compositions and physical properties to allow the loading and delivery of nematicides to plant seedlings for maximal effectiveness against plant parasitic nematodes (PPNs). PPNs are one of the world's major agricultural pests, causing in excess of \$157 billion in worldwide crop damage annually,<sup>[8]</sup> however, relatively few strategies exist for controlling PPN infection regarding as environmentally friendly, cost efficiently and use safely. PPN are primary a seedling disease, so protection early is critical to the success of the crop. This logical method to apply novel nematicide technology via seed treatments can reduce the required active ingredient by 1/1000 of the amount required for its granular application counterpart.<sup>[9]</sup> In addition to this reduction, seed treatments expose the target organism to a much higher concentration of active ingredient, substantially reducing non-target effects and environmental impact. In theory, seed treatment for nematode control is an excellent idea, but in practice it has been largely ineffectual due to

delivery problems post-germination. Avicta™ (Syngenta) is currently the most effective seed treatment for PPN on the market. Avicta™ has the active ingredient abamectin (Abm), a macrocyclic lactone with strong activity against a broad spectrum of nematodes combined with very low toxicity to mammals. However, Abm formulated in a seed treatment is limited by its lack of water solubility and high tendency to bind to the organic carbon contents in the soil.<sup>[10]</sup>

<sup>11]</sup> These traits create a very limited zone of protection around the developing root system. Hence, there is a critical need to resolve the soil mobility issues for compounds such as Abm to enhance its effectiveness against nematode damage. In previous chapter, we has developed a nanotechnological platform that increased the mobility or distribution of Abm within the soil via encapsulating Abm into a *Red clover necrotic mosaic virus*-derived plant viral nanoparticle. However, this nano-carrier for Abm compounds is not a cost-effective method. It is an elusive control method for smallholder farmers in impoverished countries: a farming population in dire need of a cost-effective approach for crop protection against PPN for higher crop yields. In this chapter, therefore, we aim to resolve the soil mobility issues for Abm using a simple lignocellulosic matrix delivery system. A variety of active ingredients have been successfully incorporated into polymeric matrices to achieve the sustained release profiles in different applications. For instance, the cellulosic carriers enabled to immobilize the loading compound, such as enzymes, and increase the ability and stability of the active ingredient because of the specific interaction between them.<sup>[12]</sup> To fight against PPN infestation, the incorporation of Abm nematicide into lignocellulosic matrix allows for widespread distribution of crop protection agent without interfering in subsistence farming practices. This nematicide-activated matrices can be simply applied at the point of seed planting where farmers can use

the concept of “wrap and plant” with their own seeds. The use of lignocellulosic materials allows for a cost-effective matrix yet still provides a controllable release mechanism for loaded active ingredients via manipulating with fiber porosity, diameter, and composition.

## **5.2 Experimental**

### **5.2.1 Materials**

The lignocellulosic fibers used in this study were abaca, banana, and two wood fibers (softwood and hardwood). Abaca was purchased from The Paperwright (Ottawa, Canada). Banana, softwood and hardwood fibers were provided by the Department of Forest Biomaterials at North Carolina State University. Abamectin and rhodamine were obtained from Sigma and used as received. Phosphate buffered saline (PBS) was purchased from Fisher Scientific. M9 buffer powder was obtained from Sigma-Aldrich.

### **5.2.2 Formation of lignocellulosic matrices and characterization**

Abaca, softwood and hardwood fibers were kraft pulped and bleached via traditional chemical and mechanical methodologies.<sup>[13]</sup> Banana fibers were chopped into 2-inch lengths and mechanically pulped by a Hollander beater for 30 minutes. The abaca pulps were made into fibrous matrices by a wooden deckle papermaking kit. Banana, softwood, softwood-hardwood pulps were made into fiber matrices by a vacuum deckle and mould. The softwood-hardwood pulp blend was at 60 weight percent softwood and 40 weight percent hardwood.

### 5.2.3 Chemical compositions of lignocellulosic matrix

Fourier transfer infrared spectroscopy in the attenuated total reflectance mode (FTIR-ATR) was used to characterize chemical compositions of the lignocellulosic matrices. All spectra were collected using a Nexus 470 FT-IR spectrometer (ESP™, Agilent Technologies) and a ATR sample attachment (Avatar OMNI-Sampler™, Thermo Scientific) with a spectral range of 4000 – 675  $\text{cm}^{-1}$ . The spectrum for each matrix was recorded in the spectral range of 4,000 – 700  $\text{cm}^{-1}$  using 64 scans at a resolution of 4  $\text{cm}^{-1}$ . The data analysis was completed with OMINC spectra software with a baseline correction and a subtraction of CO<sub>2</sub> vibration at wavelength number of ~ 2200  $\text{cm}^{-1}$ . The spectral peaks for each sample were identified and the peak areas were integrated from 1,800 to 700  $\text{cm}^{-1}$  wavenumbers using a peak analyzer program with OriginPro 8.5 data processing software (OriginLab®).

X-ray Photoelectron Spectroscopy (XPS) analysis was conducted for all lignocellulosic matrices using a SPECS™ XPS instrument (SPECS Surface Nano Analysis GmbH, Germany) with a hemispherical analyzer (SPECS PHOIBOS 150). The matrix samples were cut in small pieces (5 mm × 5mm) and fixed on the sample platform in a vacuum-analyzing chamber with base pressure in 10<sup>-10</sup> mbar range. An Mg  $\text{K}\alpha$  radiation source (1245 eV) was used to excite the electrons on the sample surface. X-Ray incidence angle is ~ 30° from surface and X-ray source to analyzer is ~ 60°. Both survey XPS spectra and high-resolution XPS spectra were measured for all lignocellulose matrices. The element determination, quantification and curve fitting of the XPS spectra were performed using CasaXPS data processing software (version 2.3.16, Casa Software Ltd.). Energy calibration was established by referencing to adventitious carbon (C1s line at binding energy of 285.0 eV)

#### 5.2.4 Physical properties of lignocellulosic matrix

The basis weight of the matrix was obtained by dividing the mass of a 2 cm × 2 cm square matrix by its area (reported in g m<sup>-2</sup>). The matrix thickness is an average of 10 separate measurements (ST-022 Ono Sokki Gauge Stand) per 2 cm × 2cm substrate. The reported thickness for each lignocellulosic matrix is the mean value of three specimen samples.

The bursting strength of the matrices was determined by using a modified standard ASTM D3787 Bursting Strength of Textile, Constant-Rate-of-Traverse (CRT).<sup>[14]</sup> The matrix sample was cut into a square sheet of 2.5 cm × 2.5 cm in size for mounting to a specially designed probe bursting apparatus (see Appendix) with a probe and two mounting plates. The bursting test was performed by an Instron Universal Tester (Bluehill Model # 5544, Morwood, MA) with a static load of 2 kN. The bursting strength is defined as the absolute force applied at the right angle to the plane of the matrix sample at the failure point divided by the area (30.7 mm<sup>2</sup>) of the probe point that was contact with matrix. The results are reported as the mean value from ten specimens of each matrix sample.

X-ray diffraction (XRD) was carried out for each matrix using a Philips/OMNI Auto-Mount™ diffractometer. The generator was utilized at 40 kV and 30 mA, and the intensities were measured in the range of 5 < 2θ < 30° with scan steps at 0.01° per second. The crystallinity index (*CrI*) was calculated from XRD data and determined based on the formula by Segal et al. as follows:<sup>[15]</sup>

$$CrI = 100 \times [(I_{002} - I_{am})/I_{002}] \quad (1)$$

in which  $I_{002}$  is the maximum intensity (in arbitrary units) of crystalline plane (002) of cellulose I, that usually lies around 2θ angle of 22°– 24° <sup>[16]</sup>, and  $I_{am}$  is the intensity of

diffraction due to the amorphous portion evaluated at  $2\theta$  angle of  $\sim 16^\circ$  for lignocellulosic materials <sup>[17]</sup>.

### **5.2.5 Loading nematicide into lignocellulosic matrices and surface characterization**

The nematicide, abamectin (Abm), was dissolved in 90 % (v/v) ethyl alcohol to make a stock solution at  $2 \text{ mg ml}^{-1}$ . The Abm solution was diluted and physisorbed onto the lignocellulosic matrices at  $32.5 \text{ ug Abm/m}^2$  based on the effective Abm dosage for nematode control as well as the size of matrix needed for the seedlings. The Abm-loaded lignocellulosic matrices (Abm-matrix) were air-dried overnight before further characterization and performance testing.

The contact angle measurements were carried out to determine the wettability of matrices before and after loading with Abm. Time-dependent contact angles (sessile drop technique) were measured by depositing  $2 \text{ }\mu\text{l}$  of deionized (DI) water drop (bulk resistivity  $14 \text{ M}\Omega\cdot\text{cm}$ ) on the matrix sample to record the average contact angle as a function of time using a DataPhysics OCA goniometer equipped with a high speed camera (30 frames/second). In addition, using the basis of Wilhelmy plate principle, the advancing contact angle, the receding contact angle and the contact angle hysteresis of matrix sample were measured by a dynamic contact angle tensiometer (DCAT 21, DataPhysics). The matrix sample (a rectangle sheet of 10 mm in length x 5 mm in width) was immersed into DI water bath to the depth of 3 mm and then retracted. During this procedure, the forces acting on the specimen were recorded by an electrobalance. The advancing contact angle ( $\theta_{adv}$ ), receding contact angle ( $\theta_{rec}$ ) and the corresponding hysteresis (CAH) are deduced from the following equations <sup>[18, 19]</sup>:

$$F = mg + p\gamma \cos \theta - \rho_l g Ax \quad (2)$$

$$CAH = \theta_{adv} - \theta_{rec} \quad (3)$$

where  $F$  is the force measured by the balance;  $m$  is the mass of sample and  $g$  is the gravitational constant;  $p$  is the perimeter of contact line (i.e., the perimeter of sample's cross-section);  $\gamma$  is the surface tension of the liquid;  $\rho_l g AL$  is the buoyancy force where  $\rho_l$  is the liquid density;  $A$  is the cross-sectional area of the sample; and  $x$  is the immersed depth of the sample.

### **5.2.6 *In vitro* released bioavailability of Abm-loaded lignocellulosic matrices to *C. elegans* nematode**

Abm release from the Abm-loaded lignocellulosic matrices was evaluated utilizing a model nematodes *Caenorhabditis elegans* (*C. elegans*) assay to determine *in vitro* release behaviors in two modes: time-dependent release and cycle-dependent release. Briefly, an Abm-matrix was cut into a 7 mm-diameter circle for immersion into 400  $\mu$ l of sterilized phosphate buffered saline (PBS) solution. For the time-dependent release test, the matrix samples were removed from the PBS solution at 1h, 2h, 3h and 4h time intervals. For the cycle-dependent release test, the matrix sample was removed from the PBS solution after 1h-immersion time and then re-immersed into a 400  $\mu$ l fresh PBS solution for 5 cycles. Subsequently, a 100  $\mu$ l aliquot of *C. elegans* culture (about 20 individual nematodes) was added into each Abm-matrix exposed PBS solution. If Abm is properly released from the lignocellulosic matrix during the PBS buffer immersion process, it serves as a paralytic to the *C. elegans* upon dosing. Healthy nematodes exhibit characteristic flexible form and undulating movement observed at 10X

magnification. If properly exposed to Abm, their movement appears rigid and linear. After 24-hour incubation at the room temperature, the number of immobilized nematodes and mobile nematodes were counted in each PBS solution under a dissecting microscope. All experiments were run in triplicate. The time-dependent and cycle-dependent releases of Abm from each Abm-matrix were reported by the nematode mortality at each time interval calculated as follows:

$$\text{Nematode mortality (\%)} = \frac{\text{number of immobile } C. elegans}{\text{total of added } C. elegans (\sim 20)} \times 100 \% \quad (4)$$

### **5.2.7 Crop protection of Abm-loaded lignocellulosic matrices to plant parasitic nematode-infected tomato plants**

To test the effectiveness of the Abm-lignocellulosic matrix to prevent root knot nematode (RKN) *Meloidogyne hapla*, tomato seedlings (selected at 2-weeks with uniform growth) were wrapped with a pre-wetted Abm matrix (6 cm x 5 cm, 0.8 gram Abm per matrix) and placed in a 6-ounce foam cup filled with sandy loam soil. Inoculation with RKN solution (5000 eggs) occurred through three holes surrounding the root. The same amount of free Abm solution was also applied in the soil as the positive control. Healthy plants without infection were taken as the negative control. Each treatment was run in triplicate, and the plants were watered as needed in the greenhouse. After 5 weeks of RKN inoculation, the roots of plants were harvested and gently washed with tap water. The galling on the root and the growth of the root were evaluated in each treatment to determine the efficacy of crop protection of different Abm-matrices.

## 5.3 Results and Discussion

### 5.3.1 Chemical characterization of lignocellulosic matrices by FTIR and XPS

The fabricated abaca, banana, softwood, and hardwood lignocellulosic matrices comprised different levels of cellulose, hemicellulose and lignin as a result of the inherent composition of the fiber source as well as due to the pulp treatment prior to sheet formation (**Table 5.2**).<sup>[7]</sup> The lignocellulose sources were selected for their regional access and in the case of banana, a known excess supply exists from harvesting its fruit. Also, due to containing phenylpropane units accessible to be self-crosslinked or reacted with other compounds, the lignin have been utilized as a coating materials or formulating matrix in controlled release applications.<sup>[20, 21]</sup> Therefore, FTIR-ATR and XPS analyses were used to characterize the chemical compositions of these lignocellulosic matrices before loading with nematicides.

**Figure 5.1** shows the FTIR spectra of the lignocellulosic matrices in the fingerprint region between  $2000\text{ cm}^{-1}$  and  $700\text{ cm}^{-1}$ , which consist of absorption bands for characteristic chemical groups of chemical compositions (cellulose, hemicellulose or lignin) in different matrices. For all matrices, the peak of C-H stretching vibration at  $899\text{ cm}^{-1}$  and the intense peaks of C-O stretching ( $\sim 1050\text{ cm}^{-1}$ ) correlated to cellulose and hemicellulose in the matrices.<sup>[22, 23]</sup> A relative larger peak at  $\sim 1610\text{ cm}^{-1}$  were shown in the spectra of banana matrix, which is characteristic of aromatic skeletal vibration present in lignin component.<sup>[24, 25]</sup> However, this lignin-related peak was decreased and become broad in other matrices; suggesting a decrease in their lignin content. Although the raw materials of abaca and woodfibers have a large amount of lignin components (**Table 5.2**), the kraft pulping and bleaching for these fibers prior to

matrix formation enabled the removal of the majority of lignin by dissolving it into small alkali soluble fragments.<sup>[26]</sup> In contrast, banana fibers were only mechanical pulped where the fibers were separated and refined without removing the lignin. For quantitative analysis, the integrated peak area of lignin-related aromatic vibration region ( $1690 - 1550 \text{ cm}^{-1}$ ) and that of cellulose/hemicellulose-related C-O stretching region ( $1090 - 922 \text{ cm}^{-1}$ ) was determined for all samples as shown in **Table 5.1**. According to the different respondent peak areas, the amount of lignin content in the matrices follows: banana (12.1 %) > abaca (4.8 %) > softwood (3.37 %) and hardwood (3.37 %). The opposite order was shown for the amount of cellulose/hemicellulose in the matrices.

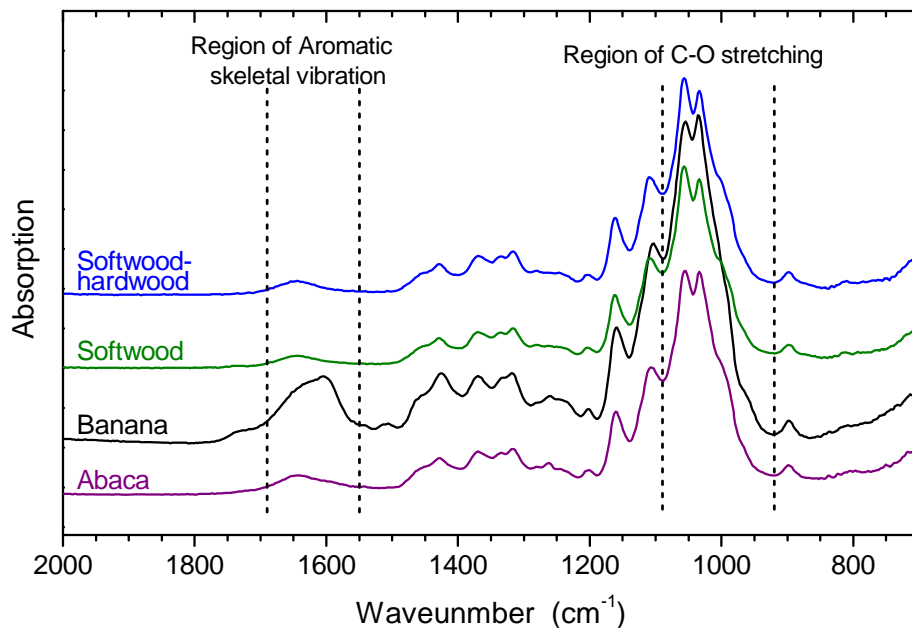


**Figure 5.1** Fourier transfer infrared spectroscopy (FTIR) analysis for abaca, banana, softwood and softwood-hardwood lignocellulosic matrices. FITR spectra of all matrices showed the peak patterns in the fingerprint region between  $2000 \text{ cm}^{-1}$  and  $700 \text{ cm}^{-1}$ , where the region of  $1690 - 1550 \text{ cm}^{-1}$  is related to aromatic skeletal vibration from lignin component and the region of  $1090 - 922 \text{ cm}^{-1}$  is related to C-O stretching from cellulose and hemicellulose content.

**Table 5.1** Chemical composition analysis for abaca, banana, softwood and softwood-hardwood lignocellulosic matrices via I. Fourier transfer infrared spectroscopy (FTIR) and II. X-ray spectroscopy (XPS).

	Abaca	Banana	Softwood	Softwood-hardwood
<i>I. FTIR analysis</i>	Integrated peak area (%) of regions			
Aromatic vibration <sup>a</sup>	4.80	10.2	3.38	3.37
C-O stretching <sup>b</sup>	50.6	44.5	52.5	52.5
<i>II. XPS analysis</i>	Fractional area (%) of C <sub>1s</sub> peak			
C <sub>1</sub> (285.0 eV)	33.0	34.7	26.2	18.9
C <sub>2</sub> (286.5 eV)	53.4	49.9	61.2	67.2
C <sub>3</sub> (288.1 eV)	13.6	15.5	12.7	13.9

<sup>a</sup>Region from 1690 to 1550 cm<sup>-1</sup> related to aromatic skeletal vibration from lignin component;

<sup>b</sup>Region from 1090 to 922 cm<sup>-1</sup> related to C-O stretching from cellulose and hemicellulose content.

XPS is a surface sensitive technique and measures the elemental composition (except H) and chemical binding information for the top 1–5 nm depth of the surface region<sup>[27]</sup>. On the other hand, FTIR-ATR has a much deeper depth of penetration (0.5 – 2 μm) from the sample surface. XPS survey spectra show that carbon and oxygen are the two main elements on all matrices' surfaces (**Figure 5.2a**). The previous study indicated that the theoretical XPS oxygen carbon atomic ratio (O/C) of cellulose and lignin are 0.83 and 0.33, respectively.<sup>[28, 29]</sup> For lignocellulose fibers, the higher O/C ratio indicates lower lignin concentration on the surface. We found that softwood-hardwood and softwood matrices have higher O/C ratio of 0.79 and 0.70 when compared with that of abaca (O/C = 0.62) and banana (O/C = 0.60) matrices; suggesting that abaca and banana matrices have more lignin content on the surface. In high-resolution XPS spectra, as shown in **Figure 5.2b**, the carbon signal (C<sub>1s</sub>) of the matrices can be resolved into three peaks (C<sub>1</sub>-C<sub>3</sub>) due to carbons at different oxidation levels: C<sub>1</sub> at binding

energy (BE) of 285.0 eV refers to unoxidized carbon (i.e., -C-H), C<sub>2</sub> at BE 286.5 eV refers to carbon with one bond to oxygen (i.e., O-C), and C<sub>3</sub> at BE 288.1 eV refers to carbon with two bonds to oxygen (i.e., O-C-O and C=O). The fractional peak areas of three C1s peaks for the different matrices are listed in **Table 5.1**. It is known that C<sub>1</sub> components arise mainly from lignin and wood extractives, whereas the C<sub>2</sub> and C<sub>3</sub> components correspond to the cellulose and hemicellulose.<sup>[28-31]</sup> Consistent with results of O/C ratio, the top surface of abaca and banana matrices was composed of higher amounts of lignin than wood fiber matrices as abaca and banana matrices have the C<sub>1</sub> peak area of 33 % and 34.7 % while that for softwood and hardwood-softwood are 26.2% and 18.9%. However, FTIR analysis demonstrate that abaca matrix have a much lower bulk lignin concentration than banana matrix. Therefore, although abaca matrix has the lower amount of bulk lignin as wood fiber matrices, due to delignification during kraft pulping, its residual lignin is largely accumulated on its top surface. This may be attributed by the re-adsorption of dissolved lignin in the final stage of pulping, washing and bleaching, forming a lignin-concentrated surface.<sup>[32, 33]</sup> XPS analysis of woodfiber matrices also suggested that wood matrices had a higher surface lignin concentration than that in the bulk as determined by FTIR analysis.

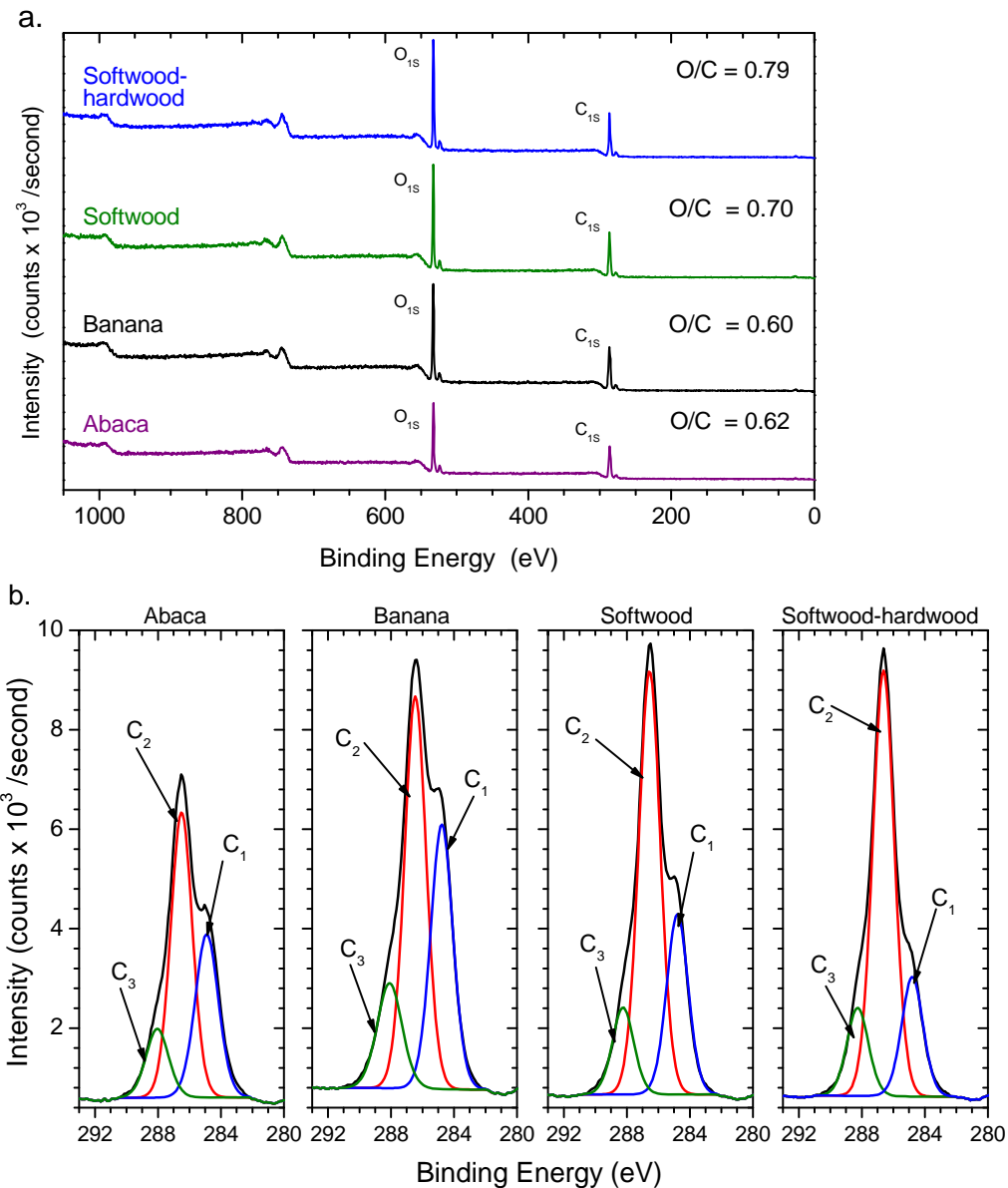


**Figure 5.2** X-ray spectroscopy (XPS) of a. low resolution survey scan and b. high resolution scan of carbon signal ( $C_{1s}$ ) for abaca, banana, softwood and softwood-hardwood lignocellulosic matrices. Only  $O_{1s}$  and  $O_{1s}$  peaks were detected in XPS survey spectra for all matrices.  $C_{1s}$  of all matrix can be resolved into three peaks:  $C_1$  at binding energy (BE) of 285.0 eV,  $C_2$  at BE of 286.5 eV and  $C_3$  at BE of 288.1 eV

### 5.3.2 Physical properties and XRD crystallinity of lignocellulosic matrices

The matrix physical properties are the critical parameters in the design of nematicide-loaded matrix in the study because our prototype is to apply the active matrix by wrapping the seed/or root of plants. It is of utmost importance that the wrapped plant seed or root can penetrate the matrix for germination and growth, which is correlated with an upper limit on burst strength for the matrices. However, the matrix too fragile or it would be a handling problem seed/ root application. The physical properties of all lignocellulose matrices were summarized in **Table 5.2**, which were governed by the chemical compositions, the pulping conditions as well as the matrix formation process. The abaca matrix exhibited the lowest bursting strength of  $\sim 67$  kPa even it had relatively higher basis weight and thickness, which may be attributed by its smaller fiber diameter as well as the chemical pulping process. The mechanical-pulped banana matrix had the largest burst strength of 101 kPa than the chemical-pulped softwood matrix (69 kPa) even though they had the similar basis weight, thickness and fiber diameter. Softwood-hardwood matrix achieved the highest burst strength of 115 kPa by increasing its basis weight and thickness. The pouch germination and pot growth studies demonstrated that tomato and corn seeds could germinate and penetrate the abaca, gampi, banana, softwood matrices. Conversely, the softwood-hardwood matrix reduced the seeds' germination and growth in some degree due to its higher bursting strength (Data not shown). We also found that the low strength of abaca matrix made it difficult to handle during crop protection testing.

**Table 5.2** Chemical and physical properties of different lignocellulosic matrices

	Abaca	Banana	Softwood	Softwood-hardwood
<i>I. Chemical Properties of raw materials</i>				
Source	leaf stalk	stem	stem	stem
<sup>a</sup> Cellulose <sup>[34-38]</sup>	56.0 – 68.3	32.5 – 39.1	39.2 – 47.3	39.2 – 45.7
<sup>b</sup> Hemicellulose <sup>[34-38]</sup>	14.9 – 19.0	12.5 – 16.6	14.1 – 20.9	14.1 – 23.2
<sup>c</sup> Lignin <sup>[34-38]</sup>	7.60 – 13.3	14.4 – 15.9	21.1 – 28.6	21.1 – 23.2
<i>II. Physical Properties</i>				
Basis weight, g m <sup>-2</sup>	80.0	62.7	64.0	122.5
Thickness, cm	0.13	0.052	0.053	0.17
Fiber diameter, μm	14.7	31.8	26.6	26.4
Burst strength, kPa	66.8	100.9	69.1	115.2
Moisture, %	6.64	8.22	6.17	6.56
Crystalline index	46	40	47	52

<sup>a</sup>Cellulose, <sup>b</sup>Hemicellulose and <sup>c</sup>Lignin data are literature values

Cellulose crystallinity, i.e. the relative portions of crystalline cellulose and amorphous cellulose, is another important factor that affect not only the physical properties of the fibrous matrices, but also the loading and release of nematicide with the matrices. XRD is a well-known techniques to measure the crystallinity of cellulose<sup>[16]</sup>. As shown in **Figure 5.3**, all matrices exhibited the similar XRD diffractogram with two major peaks: the first intensity peak at 23° and the secondary intensity peak around 16°. In the cellulose crystalline region, the parallel polymer chains align side-by-side via hydrogen bonding in flat sheets.<sup>[39, 40]</sup> The peak at 23° is indicative of the distance between hydrogen-bonded sheets in cellulose,<sup>[17]</sup> referring to the crystalline plane (002) in the lignocellulose samples. A broad peak at ~ 16°, which is known to be an overlapping of two peaks (16.7° and 14.9°) from cellulose, is assumed to correspond to the amorphous region for lignocellulose materials.<sup>[17, 41]</sup> For quantitative

analysis, the crystallinity index (CrI) of the lignocellulosic fibers was calculated from XRD patterns based on the Segal's peak height methods <sup>[15]</sup>. This is a simple and most frequently used method to determine CrI using the ratio of peaks' height at 23° and 16°.<sup>[42]</sup> Using this method we show in **Table 5.2** the degree of crystallinity of the matrices as follows: softwood/hardwood (51.6%) > softwood (47.2%) > abaca (45.6%) > banana (40.0%). The higher cellulose crystallinity of wood and abaca fibers may be attributed by the solubilization of lignin and the crystallization of amorphous cellulose during kraft pulping.<sup>[43]</sup> However, the low amount of cellulose and high amount of bulk lignin in banana fibers resulted in the lower crystallinity for the banana matrix. The degree of crystallinity affects its chemical and water absorptions of the matrices.<sup>[44]</sup> Lower cellulose crystallinity means higher amorphous regions, a region that is more accessible to chemicals and water. As a result, banana matrices had higher moisture absorption of 8.215 % and in comparison with abaca matrices (6.642 %), softwood (6.167%) and softwood/hardwood (6.563 %) matrices (**Table 5.2**).

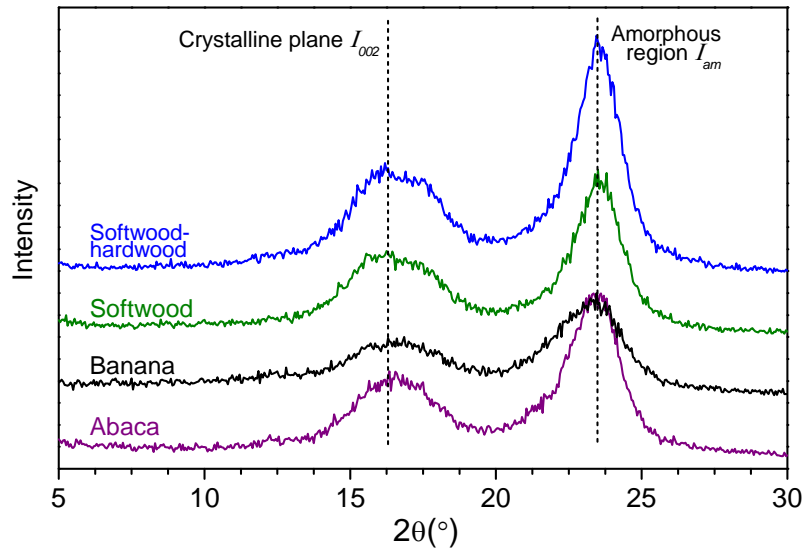


**Figure 5.3** X-ray diffraction (XRD) for abaca, gampi, banana, softwood and softwood-hardwood lignocellulosic matrices. All matrices showed the similar XRD diffractogram where a peak at  $23^\circ$  refers to crystalline plane (002) in matrices and a broad peak at  $\sim 16^\circ$  refers to the amorphous regions of matrices.

### 5.3.3 Surface characterization of Abm-loaded lignocellulosic matrices

The surface chemistry of Abm-loaded lignocellulosic matrices and untreated matrices was inferred by contact angle goniometer (sessile drop technique) and contact angle tensiometer (Wilhelmy plate method) measurements. In the sessile drop technique, a water drop is resting on the matrix surface, and the contact angle is defined as the angle formed by the intersection of the liquid-solid interface and the liquid-vapor interface. By this method, abaca, softwood, softwood/hardwood matrices demonstrated a more hydrophilic surface with the immediate drop absorption (denoted as a water contact angle of zero). Loading Abm into these matrices didn't show measurable change in the contact angle. However, as shown in **Figure 5.4**, the banana matrix comprised relative less wettability in comparison with a starting contact angle of  $69^\circ$  to  $20^\circ$  after 10 seconds. This less wettability of the banana matrix may be attributed to

the non-polar lignin content, impurities (e.g. wax), as well as its higher moisture absorption.<sup>[45]</sup> Loading Abm into banana matrix led to the increase of its starting contact angle to 95°, followed by a slower water adsorption as evidence that its contact angle were still kept at 70° after 10 seconds of contact time. This change in the surface properties of Abm-banana matrix would be mainly attributed by the hydrophobic properties of loaded Abm.<sup>[10]</sup>

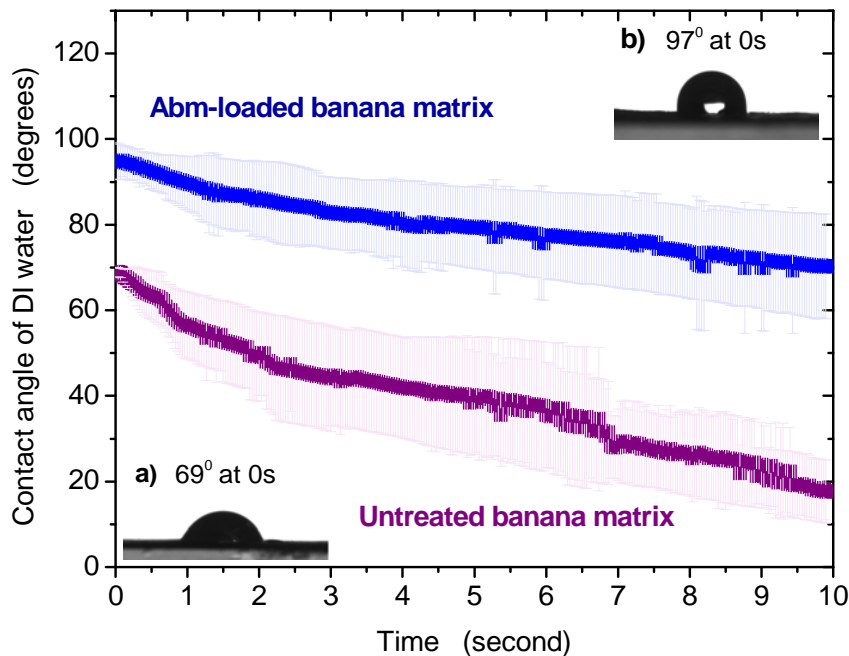


**Figure 5.4** Dynamic contact angle goniometer measurements for banana fiber and Abm-loaded banana fiber matrices. The loading concentration of Abm on the matrix was 32.5  $\mu\text{g m}^{-2}$ . The measurement for abaca, gampi, softwood, softwood/hardwood fiber matrices were negligible due to immediate drop absorption. The insert show photographs of water droplet on a) untreated banana matrix and b) Abm-loaded banana matrix.

It is hard to measure the contact angle by goniometer when the disposing water is very quick absorbed by the substrate sample. To overcome it, a Wilhelmy plate method by tensiometer is widely used to indirectly measure contact angle on a solid sample<sup>[46]</sup>. By this

technique, the studied lignocellulosic matrices were immersed to a depth of 3 mm and then retracted. The advancing contact angle ( $\theta_{adv}$ ), receding contact angles ( $\theta_{rec}$ ) for the samples were calculated from the slope of linear regression of the measured force and immersion depth. As listed in **Table 5.3**, banana matrix exhibited a significantly higher  $\theta_{adv}$  value of  $91.5^\circ$  when compared with the  $\theta_{adv}$  values of abaca ( $72.5^\circ$ ), softwood ( $70.3^\circ$ ), softwood/hardwood ( $70.6^\circ$ ) ( $p < 0.01$ ). The previous study has confirmed that  $\theta_{adv}$  was most closely associated with the lower surface free energy component and thereby it was more sensitive to the hydrophobic portion on the sample surface.<sup>[47]</sup> As a result, all Abm-matrices shown an increased  $\theta_{adv}$  values compared to untreated matrices due to the presence of hydrophobic Abm on the surface of the matrices. This is consistent with the goniometer results for banana matrix. On the other hand, the  $\theta_{rec}$  is most closely associated with the higher surface free energy component.<sup>[47]</sup> Once the matrix sample is entirely immersed in aqueous solution, the  $\theta_{rec}$  would correspond to carboxyl groups of cellulose component on the matrix to prevent the liquid from being pulled away. As a result, all matrices shown the approximate  $\theta_{rec}$  values, and adding hydrophobic Abm didn't cause the significant change for their  $\theta_{rec}$  values. A difference between  $\theta_{adv}$  and  $\theta_{rec}$  of the solid sample was recorded as contact angle hysteresis (*CAH*), which is affected by surface roughness, chemical heterogeneity of the surface, reorientation or mobility of the surface segment, swelling and deformation.<sup>[48, 49]</sup> It was found that banana matrix exhibited a much higher *CAH* value of  $24.8^\circ$  than other matrices. This may be attributed by chemical heterogeneity of its surface that remains lignin or wax due to its mechanically pretreatment. Whereas the woodfibers and abaca matrix have been chemical krafted pre-treated, which should remove the most of lignin, hemicellulose and other impurities while maintaining

cellulose in it. The increase in *CAH* was observed after Abm loading for all matrices; indicating the change in surface heterogeneity or swelling of the cellulose fibers.<sup>[49]</sup>

**Table 5.3** Advancing contact angle ( $\theta_{adv}$ ), receding contact angle ( $\theta_{rec}$ ) and contact hysteresis (*CAH*) tested via a modified Wilhelmy plate method for untreated and Abm-loaded lignocellulosic matrices

Fiber matrices	Untreated			Abm-loaded		
	$\theta_{adv}$	$\theta_{rec}$	<i>CAH</i>	$\theta_{adv}$	$\theta_{rec}$	<i>CAH</i>
Abaca	72.5°	68.6°	3.9°	77.2°	68.5°	8.8°
Banana	91.5°	66.8°	24.8°	97.8°	70.6°	26.4°
Softwood	70.3°	68.5°	1.8°	76.3°	68.7°	7.6°
Softwood-hardwood	70.6°	64.0°	6.6°	75.8°	65.1°	10.7°

#### 5.3.4 *In vitro* released bioassay of Abm-loaded lignocellulosic matrices

The hypothesis of this study is that a fibrous matrix can provide an additional mechanism for controlled release of loaded active ingredients, which can be tailored by chemical and physical properties of the matrices. **Figure 5.5a** shows the time-dependent release profiles of loaded Abm from Abm-matrices based on the bioavailability to *C. elegans* nematodes. For the Abm-abaca matrix, almost 95% of nematodes were immobilized within one hour of immersion, suggesting a quick release of loaded Abm. In contrast, a relative slow release of loaded Abm was displayed in Abm-banana, Abm-softwood and Abm-softwood-hardwood matrices with mortality rates of 23%, 42% and 21% in the one-hour immersion time, respectively. After four-hours of immersion, more than 93% and 97% nematode mortality was achieved by Abm-banana and Abm-softwood matrices, but Abm-softwood-hardwood matrix only resulted in a 78% mortality of nematodes. Adding same amount of free Abm in the

nematode culture caused 100 % nematode mortality. The virgin fibrous matrices didn't show any toxicity to nematodes.

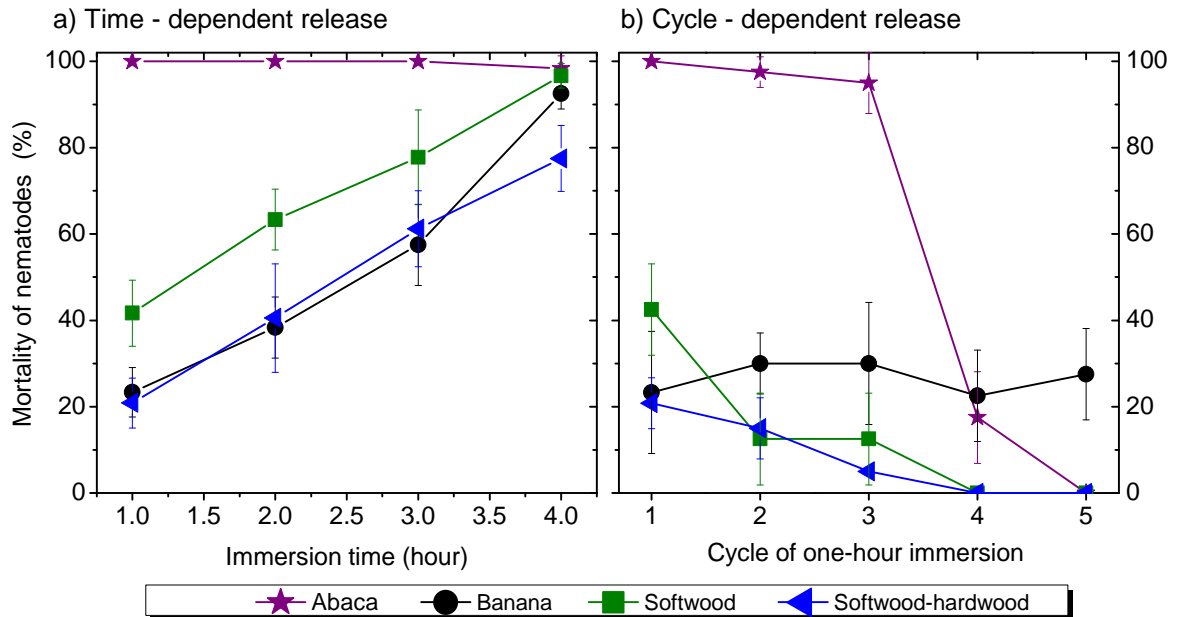


**Figure 5.5** *In vitro* bioassay to determine the mortality of *C. elegans* nematodes via a) time-dependent release and b) cycle-dependent release from Abm-loaded abaca (★), banana (●), softwood (■), and softwood/hardwood (▲) lignocellulosic matrices. The loading concentration of Abm on the matrix was 32.5  $\mu\text{g m}^{-2}$ .

As far as the crop protection of nematode-infected plant was concerned, the effective nematicide-loaded matrices should enable long-term release of its active ingredients during one month. With this purpose, an *in vitro* cycle-dependent release of Abm-matrix was designed to predict the long-term release behaviors of the studied matrices, where the Abm-matrix was re-immersed in a new fresh release medium after every 1 hour (one cycle). As illustrated in **Figure 5.5b**, the high nematode mortality of ~ 95% was achieved for Abm-abaca matrix in three cycles, and then it lost the bioavailability to nematodes in following cycles; suggesting a

depletion in released Abm from Abm-abaca matrix. In contrast, Abm-banana matrix exhibited the relative lower but more stable toxicity to nematodes in all five cycles (23%, 30%, 30%, 23%, and 28% of mortality for each cycle). The mortality of 43 % were achieved by Abm-softwood in the first cycle, but its effectiveness were reduced to 12.5 % in second and three cycles. Abm-softwood-hardwood matrix caused a mortality of 21 % in the first cycle, and then gradually reduced its toxicity to nematodes in the following cycles. We infer that the slow and sustainable release profiles of Abm-banana would be contributed by the potential interaction of Abm with lignin component in the banana matrix. Because lignin polymer is derived from phenylpropane units containing various functional groups, such as phenolic hydroxyl, alcohol hydroxyl, aromatic units, it could induce an interaction with Abm via chemical reaction, hydrophobic interaction or Van der Waals forces. Although the chemistry or physical nature of these potential interaction with lignin is not fully understood, Xiao et al. has demonstrated that the incorporation of lignin led to the improved adhesion strength of soy protein-based adhesive on wood veneer.<sup>[50]</sup> Khan et al. has successfully developed a wood adhesive using bagasse lignin that shown the same adhesive strength as traditional phenol-formaldehyde (PF) wood adhesive.<sup>[51]</sup> On the other hand, a lignin-concentrated surface of abaca matrix would prevent the diffusion of Abm molecules into the bulk of matrix, resulting in the distribution of Abm in its top surface. This could attribute to the burst release profile of Abm-abaca matrix.

### **5.3.5 Crop protection of Abm-loaded lignocellulosic matrices**

The crop protection efficacy of these Abm-matrices was tested in tomato seedlings that were infected with Root knot nematode (RKN) *Meloidogyne hapla* in the sand loam soils.

After 5 weeks of RKN inoculation, the crop protection of Abm-matrices was evaluated by root growth and root galling in the basis of 0 – 4 unit-scales, where the scale of zero refers to the optimum growth of root and no galling on roots, and scale of 4 refers to the worst growth of root and worst galling on roots. **Table 5.4** summarizes the crop protection results for free Abm and all studied Abm-matrices. Compared to positive control of RKN-infected plant (root growth of 3.5 and root galling of 4.0), applying free Abm in the RKN-infected soil didn't show an effective prevention of RKN damage as evident by only a very slight improvement in root growth (score of 3) and root galling (score of 3.75) for the infected plants.

**Table 5.4** Crop protection results of free Abm and Abm-loaded lignocellulosic matrices to tomato plants infected with *Meloidogyne hapla* nematode in greenhouse.

Evaluation	Uninfected control	Infected control	Free Abm	Abm-loaded lignocellulosic matrices			
				Abaca	Banana	Softwood	Softwood-hardwood
Root growth score <sup>a</sup>	0	3.50	3.00	3.00	2.00	2.53	3.67
Root galling score <sup>b</sup>	0	4.00	3.72	3.50	1.83	2.94	3.57

<sup>a</sup> Plant root growth score were determined at 5 weeks after treatment, using a 0 - 4 unit-scale where 0 = optimum growth of uninfected plant and 4 = worst root growth of the infected plant

<sup>b</sup> Plant root galling score determined at 5 weeks after treatment, obtained using a 0 - 4 unit-scale where 0 = no galling of uninfected plants and 4 = worst galling of infected plants. Data were reported by means of three replications.

Among all matrices, Abm-banana matrices are the most efficacious for crop protection of the RKN-infected plant with score of 2 for root growth and score of 1.83 for root galling. We attribute this positive result to the sustainable release properties of the banana matrix. Abm-softwood matrices also gave rise to better prevention of RKN (root growth of 2.53 and root

galling of 2.94) than free Abm. This result was consistent with its *in vitro* release profiles where Abm-softwood gradually released the loaded Abm and preserved its bioavailability to the nematode in first three cycles (**Figure 5.5**). Abm-abaca matrix, on the other hand, did not appear effective against RKN which we attribute to a potential burst release of loaded Abm cargo. Wrapping with Abm-softwood-hardwood matrix didn't improve RKN infestation, and it even caused the worst root growth due to its high bursting strength which prevented proper root propagation.

#### **5.4 Conclusion**

The major issue with Abm as an effective nematicide is its poor distribution in soil due to a high binding affinity to organic soil compounds. A simple and effective approach to improve the Abm's nematicide efficacy in the soil were developed by loading Abm into lignocellulosic matrices via physisorption. The interaction of Abm with the different supporting matrices dictated the release profiles of Abm, which can be manipulated by chemical compositions of celluloses, hemicellulose and lignin and their distributions within lignocellulosic materials. The higher amount of lignin content in the bulk of lignocellulosic matrix, e.g. mechanically pulped banana matrix, appears to be an adhesive to enable the slow and sustainable release of loaded Abm from the supporting matrices; providing an efficacious delivery of Abm around the plant root to prevent it from plant parasite nematode damage. In contrast, the kraft pulped lignocellulosic matrices decreased its lignin compounds and hence led to relatively quick release of physically loaded Abm from the matrices; compromising the delivery of Abm to the growing root of the plants. On the other hand, the lignin-concentrated surface of abaca

lignocellulosic matrix prevented the diffusion of Abm molecules into the bulk of fibrous matrix, resulting in the distribution of Abm in its top surface. This attributed to the burst release of Abm from Abm-abaca matrix. The physical properties of lignocellulose matrices, such as burst strength, cellulose crystallinity and moisture adsorption, also affect its function to be the substrate for Abm loading as well as its wrapping with plant seedling during application. Future work for this study is to elucidate the influence of different factors (e.g. Abm located on surface or inside of fiber, Abm-lignin interaction, matrix's cellulosic crystallinity) on the Abm release from Abm-lignocellulosic matrix. The lignocellulosic matrix also can be modified to graft the specific functional groups to create an additional approach for controlled release of Abm or other active ingredients in different applications.

## **5.5 References**

- [1] S. Thomas, S.A. Paul, L.A. Pothan, B. Deepa, Natural Fibres: Structure, Properties and Applications, in: S. Kalia, B.S. Kaith, I. Kaur (Eds.) Cellulose Fibers: Bio- and Nano-Polymer Composites, Springer Berlin Heidelberg, 2011, pp. 3-42.
- [2] S. Kalia, B.S. Kaith, I. Kaur, Pretreatments of natural fibers and their application as reinforcing material in polymer composites—A review, *Polymer Engineering & Science*, 49 (2009) 1253-1272.
- [3] W.K. Czaja, D.J. Young, M. Kawecki, R.M. Brown, The Future Prospects of Microbial Cellulose in Biomedical Applications, *Biomacromolecules*, 8 (2006) 1-12.
- [4] A. Carroll, C. Somerville, Cellulosic Biofuels, *Annual Review of Plant Biology*, 60 (2009) 165-182.

- [5] Y.H.P. Zhang, Reviving the carbohydrate economy via multi-product lignocellulose biorefineries, *J Ind Microbiol Biotechnol*, 35 (2008) 367-375.
- [6] S. Malherbe, T.E. Cloete, Lignocellulose biodegradation: Fundamentals and applications, *Re/Views in Environmental Science and Bio/Technology*, 1 (2002) 105-114.
- [7] F. Hu, A. Ragauskas, Pretreatment and Lignocellulosic Chemistry, *Bioenerg. Res.*, 5 (2012) 1043-1066.
- [8] P. Abad, J. Gouzy, J. Aury, P. Castagnone-Sereno, E. Danchin, E. Deleury, L. Perfus-Barbeoch, V. Anthouard, F. Artiguenave, V. Blok, M. Caillaud, P. Coutinho, C. Dasilva, F. De Luca, F. Deau, M. Esquibet, T. Flutre, J. Goldstone, N. Hamamouch, T. Hewezi, O. Jaillon, C. Jubin, P. Leonetti, M. Magliano, T. Maier, G. Markov, P. McVeigh, G. Pesole, J. Poulain, M. Robinson-Rechavi, E. Sallet, B. Ségurens, D. Steinbach, T. Tytgat, E. Ugarte, C. van Ghelder, P. Veronico, T. Baum, M. Blaxter, T. Bleve-Zacheo, E. Davis, J. Ewbank, B. Favery, E. Grenier, B. Henrissat, J. Jones, V. Laudet, A. Maule, H. Quesneville, M. Rosso, T. Schiex, G. Smant, J. Weissenbach, P. Wincker, Genome sequence of the metazoan plant-parasitic nematode *Meloidogyne incognita*, *Nature Biotechnology*, 26 (2008) 909-915.
- [9] Fungicide and Nematicide Tests, in: Seed treatment vs. in-furrow applied nematicides and insecticides for reniform nematode and thrips control, The American Phytopathological Society, 206.
- [10] K.A. Krogh, T. Søbørg, B. Brodin, B. Halling-Sørensen, Sorption and Mobility of Ivermectin in Different Soils All rights reserved. No part of this periodical may be reproduced or transmitted in any form or by any means, electronic or mechanical, including photocopying,

recording, or any information storage and retrieval system, without permission in writing from the publisher, *J. Environ. Qual.*, 37 (2008) 2202-2211.

[11] V.F. Gruber, B.A. Halley, S.C. Hwang, C.C. Ku, Mobility of avermectin B1a in soil, *Journal of Agricultural and Food Chemistry*, 38 (1990) 886-890.

[12] G.K. Robinson, *Methods in biotechnology—immobilization of enzymes and cells*: Edited by G F Bickerstaff. pp 367. Humana Press, New Jersey. 1996, *Biochemical Education*, 25 (1997) 232.

[13] C. Haqiopol, J.W. Johnston, *Chemistry of modern papermaking*, , CRC Press, Boca Raton, FL, 2011.

[14] L.D. de Sa, A.L. Gomes, A. Nogueira Jde, T.C. Villa, K.M. de Souza, P.F. Palha, Intersectorality and bonding in tuberculosis control in Family Health, *Rev Lat Am Enfermagem*, 19 (2011) 387-395.

[15] L. Segal, J.J. Creely, A.E. Martin, C.M. Conrad, An Empirical Method for Estimating the Degree of Crystallinity of Native Cellulose Using the X-Ray Diffractometer, *Textile Research Journal*, 29 (1959) 786-794.

[16] N. Terinte, R. Ibbett, K.C. Schuster, Overview on native cellulose and microcrystalline cellulose i structure studied x-ray diffraction (WAXD): comparison between measurement techniques., *Lenzinger Berichte*, 89 (2011) 118-131.

[17] G. Cheng, P. Varanasi, C. Li, H. Liu, Y.B. Melnichenko, B.A. Simmons, M.S. Kent, S. Singh, Transition of Cellulose Crystalline Structure and Surface Morphology of Biomass as a Function of Ionic Liquid Pretreatment and Its Relation to Enzymatic Hydrolysis, *Biomacromolecules*, 12 (2011) 933-941.

- [18] C.M. Alves, R.L. Reis, J.A. Hunt, The dynamics, kinetics and reversibility of protein adsorption onto the surface of biodegradable materials, *Soft Matter*, 6 (2010) 4135-4143.
- [19] J.A. Kleingartner, S. Srinivasan, J.M. Mabry, R.E. Cohen, G.H. McKinley, Utilizing Dynamic Tensiometry to Quantify Contact Angle Hysteresis and Wetting State Transitions on Nonwetting Surfaces, *Langmuir*, 29 (2013) 13396-13406.
- [20] M. Fernández-Pérez, E. González-Pradas, M.D. Ureña-Amate, R.M. Wilkins, I. Lindup, Controlled Release of Imidacloprid from a Lignin Matrix: Water Release Kinetics and Soil Mobility Study, *J. Agric. Food Chem.*, 46 (1998) 3828-3834.
- [21] W.J. Mulder, R.J.A. Gosselink, M.H. Vingerhoeds, P.F.H. Harmsen, D. Eastham, Lignin based controlled release coatings, *Industrial Crops and Products*, 34 (2011) 915-920.
- [22] H. Yang, R. Yan, H. Chen, D.H. Lee, C. Zheng, Characteristics of hemicellulose, cellulose and lignin pyrolysis, *Fuel*, 86 (2007) 1781-1788.
- [23] H. Ornaghi, Jr., M. Poletto, A. Zattera, S. Amico, Correlation of the thermal stability and the decomposition kinetics of six different vegetal fibers, *Cellulose*, (2013) 1-12.
- [24] P. Yu, Microprobing the molecular spatial distribution and structural architecture of feed-type sorghum seed tissue (*Sorghum Bicolor L.*) using the synchrotron radiation infrared microspectroscopy technique, *Journal of Synchrotron Radiation*, 18 (2011) 790-801.
- [25] X. Colom, F. Carrillo, F. Nogués, P. Garriga, Structural analysis of photodegraded wood by means of FTIR spectroscopy, *Polymer Degradation and Stability*, 80 (2003) 543-549.
- [26] J. Gierer, Chemical aspects of kraft pulping, *Wood Sci. Technol.*, 14 (1980) 241-266.
- [27] C.Y. Tang, Y.-N. Kwon, J.O. Leckie, Probing the nano- and micro-scales of reverse osmosis membranes—A comprehensive characterization of physiochemical properties of

uncoated and coated membranes by XPS, TEM, ATR-FTIR, and streaming potential measurements, *Journal of Membrane Science*, 287 (2007) 146-156.

[28] G.M. Dorris, D.G. Gray, The surface analysis of paper and wood fibres by ESCA (electron spectroscopy for chemical analysis). I. application to cellulose and lignin, *Cellulose chemistry and technology*, 12 (1979) 9-23.

[29] G.M. Dorris, D.G. Gray, The surface analysis of paper and wood fibres by ESCA. II. Surface composition of mechanical pulps, *Cellulose chemistry and technology*, 12 (1978) 721-734.

[30] A. Koubaa, B. Riedl, Z. Koran, Surface analysis of press dried-CTMP paper samples by electron spectroscopy for chemical analysis, *Journal of Applied Polymer Science*, 61 (1996) 545-552.

[31] L. Zhong, S. Fu, F. Li, H. Zhen, Chlorine dioxide treatment of sisal fiber: surface lignin and its influences on fiber surface characteristics and interfacial behavior of sisal fiber/phenolic resin composites, *BioResources*, 5 (2010) 2431-2446.

[32] N. Maximova, M. Österberg, K. Koljonen, P. Stenius, Lignin adsorption on cellulose fibre surfaces: Effect on surface chemistry, surface morphology and paper strength, *Cellulose*, 8 (2001) 113-125.

[33] K. Koljonen, M. Österberg, M. Kleen, A. Fuhrmann, P. Stenius, Precipitation of lignin and extractives on kraft pulp: effect on surface chemistry, surface morphology and paper strength, *Cellulose*, 11 (2004) 209-224.

- [34] R. Punyamurthy, D. Sampathkumar, C.V. Srinivasa, B. Bennehalli, EFFECT OF ALKALI TREATMENT ON WATER ABSORPTION OF SINGLE CELLULOSIC ABACA FIBER, *BioResources*, 7 (2012) 3515-3524.
- [35] J.C. del Río, A. Gutiérrez, Chemical Composition of Abaca (*Musa textilis*) Leaf Fibers Used for Manufacturing of High Quality Paper Pulps, *Journal of Agricultural and Food Chemistry*, 54 (2006) 4600-4610.
- [36] L. Singh, T.K. Bandyopadhyay, Handmade paper from banana stem, *International Journal of Scientific & Engineering Research*, 4 (2013) 2074-2079.
- [37] K. Li, S. Fu, H. Zhan, Y. Zhan, L. Lucia, ANALYSIS OF THE CHEMICAL COMPOSITION AND MORPHOLOGICAL STRUCTURE OF BANANA PSEUDO-STEM, *BioResources*, 5 (2010) 576-585.
- [38] J.V. Trigueiro, A. Nogueira Jde, L.D. de Sa, P.F. Palha, T.C. Villa, D.R. Trigueiro, Tuberculosis control: decentralization, local planning and management specificities, *Rev Lat Am Enfermagem*, 19 (2011) 1289-1296.
- [39] Y. Nishiyama, J. Sugiyama, H. Chanzy, P. Langan, Crystal Structure and Hydrogen Bonding System in Cellulose I $\alpha$  from Synchrotron X-ray and Neutron Fiber Diffraction, *Journal of the American Chemical Society*, 125 (2003) 14300-14306.
- [40] Y. Nishiyama, P. Langan, H. Chanzy, Crystal Structure and Hydrogen-Bonding System in Cellulose I $\beta$  from Synchrotron X-ray and Neutron Fiber Diffraction, *Journal of the American Chemical Society*, 124 (2002) 9074-9082.

- [41] L.P. Xiao, Z.J. Sun, Z.J. Shi, F. Xu, R.C. Sun, Impact of Hot Compressed Water Pretreatment on the Structural Changes of Woody Biomass for Bioethanol Production, *BioResources*, 6 (2011) 1576-1598.
- [42] A. Thygesen, J. Oddershede, H. Lilholt, A.B. Thomsen, K. Ståhl, On the determination of crystallinity and cellulose content in plant fibres, *Cellulose*, 12 (2005) 563-576.
- [43] R. Evans, R.H. Newman, U.C. Roick, I.D. Suckling, A.F.A. Wallis, Changes in cellulose crystallinity during kraft pulping. Comparison of infrared, X-ray diffraction and solid state NMR results, *Holzforschung*, 49 (1995) 498-504.
- [44] H.N. Dhakal, Z.Y. Zhang, M.O.W. Richardson, Effect of water absorption on the mechanical properties of hemp fibre reinforced unsaturated polyester composites, *Composites Science and Technology*, 67 (2007) 1674-1683.
- [45] K.N. Indira, Y. Grohens, C. Baley, S. Thomas, K. Joseph, L.A. Pothen, Adhesion and wettability characteristics of chemically modified banana fibre for composite manufacturing, *Journal of Adhesion Science and Technology*, 25 (2011) 1515-1538.
- [46] Y. Yuan, T.R. Lee, Contact Angle and Wetting Properties, in: G. Bracco, B. Holst (Eds.) *Surface Science Techniques*, Springer Berlin Heidelberg, 2013, pp. 3-34.
- [47] R.E. Johnson Jr, R.H. Dettre, D.A. Brandreth, Dynamic contact angles and contact angle hysteresis, *Journal of Colloid and Interface Science*, 62 (1977) 205-212.
- [48] H. Otsuka, Y. Nagasaki, K. Kataoka, Dynamic wettability study on the functionalized PEGylated layer on a polylactide surface constructed by the coating of aldehyde-ended poly(ethylene glycol) (PEG)/polylactide (PLA) block copolymer, *Science and Technology of Advanced Materials*, 1 (2000) 21-29.

[49] L.S. Penn, B. Miller, A study of the primary cause of contact angle hysteresis on some polymeric solids, *J. Colloid Interface Sci.*, 78 (1980) 238-241.

[50] Z. Xiao, Y. Li, X. Wu, G. Qi, N. Li, K. Zhang, D. Wang, X.S. Sun, Utilization of sorghum lignin to improve adhesion strength of soy protein adhesives on wood veneer, *Industrial Crops and Products*, 50 (2013) 501-509.

[51] M.A. Khan, S.M. Ashraf, V.P. Malhotra, Development and characterization of a wood adhesive using bagasse lignin, *International Journal of Adhesion and Adhesives*, 24 (2004) 485-493.

## Chapter 6. Plan Viral Nanoparticle Loaded Lignocellulosic Matrices for Active Delivery

### Abstract:

A hybrid active-delivery matrix comprising plant viral nanoparticles (PVNs) embedded on a lignocellulosic fibrous matrix is fabricated to enable efficacious delivery and tunable release of nematicide for nematode control. The nematicide, abamectin, is encapsulated by the PVN derived from the *Red clover necrotic mosaic virus*, and then incorporated into lignocellulosic matrices via physisorption. Although structural dynamics of PVN to environmental stimuli enables the controlled release of loaded Abm, varying the supporting lignocellulosic matrices that are different in chemical compositions and physical properties provides an additional release transport mechanism of Abm for nematode control. Incorporating PVN<sup>Abm</sup> into chemically pulped abaca and softwood matrices resulted in a burst release of PVN<sup>Abm</sup> and thus comparative effectiveness to *C. elegans* nematode as free PVN<sup>Abm</sup> in the solution. In contrast, the slow and sustainable delivery of Abm is achieved by loading PVN<sup>Abm</sup> into mechanically pulped banana matrix, which exhibits a delayed activity against *C. elegans* nematodes in liquid culture. However, it was found loading PVN<sup>Abm</sup> in any lignocellulosic matrix compromises its nematicide efficacy in the soil condition. In summary, although incorporating cargo loaded PVN to fibrous matrix shows an ability to additionally tune the release of loading cargo, the stability of PVN on the matrix and interaction between them needs to be elucidated for optimization of this hybrid delivery system.

## 6.1 Introduction

In previous Chapters, we discussed the potential of *Red clover necrotic mosaic virus* (RCNMV) derived plant viral nanoparticles to be a “smart” active delivery system due to their monodisperse, well-defined robust structures for cell active delivery, a polyvalent ligand-display surface for cell targeting engineering, and non-pathogenic and non-infectious nature in humans.<sup>[1, 2]</sup> However, cargo release from PVNs is dependent on the inherent structural dynamics of the virus. This places a constrained platform for tailoring the release of active ingredients. To overcome this problem, we aim to incorporate abamectin-loaded PVN (PVN<sup>Abm</sup>) into lignocellulosic fibrous matrix for optimum delivery and controllable release of abamectin for plant parasite nematode control. By combining the PVN with a fibrous matrix, we increase the surface area to volume capacity of the delivery vehicle. This ecological bonus prevents killing beneficial organisms in the soil as well as isolates the toxicity of the nematicide from the end-user. More importantly, the physical properties (or polymer dynamics) of the matrices and interaction between PVNs and matrices could be an additional tuning mechanism for the release of the active ingredient.

Our hypothesis for this PVN<sup>Abm</sup>-matrix system is that the release of small Abm from the PVN-matrix system varies with the binding affinities between all three components: Abm, PVN and fibrous matrix. As Chapter 4 addresses the abamectin’s interaction with PVN, the future studies will seek to understand the influence of chemical composition, surface chemistry and morphology of the supporting matrix on the distribution of PVNs throughout the material as well as the impact on nematicide performance of abamectin. The long-term goal is to elucidate the PVNs’ interaction with supporting matrices that are made of different materials

(e.g. cellulosic, biodegradable polymer) and the mutual interactions by different incorporation methods for PVNs and fibrous matrix (e.g. physisorption, *in situ* processing or chemical conjugation). The specific aim of this Chapter is to 1) physically incorporate PVN<sup>Abm</sup> with different lignocellulosic matrices that provide an additional sustainable release or burst release profile for loaded PVN<sup>Abm</sup> and 2) determine the incorporation impact on release behavior and efficiency of the loaded cargo. These results will provide the preliminary support for our PVN-matrix delivery system; allowing the optimization of this hybrid delivery system specific for different applications.

## **6.2 Experimental**

### **6.2.1 Materials**

The lignocellulosic fibers used in this study were abaca, banana, and two woodfibers (softwood and hardwood). Abaca was purchased from The Paperwright. Banana, softwood and hardwood fibers were provided by the Department of Forest Biomaterials at NC State University. Abamectin, rhodamine and M9 buffer powder were obtained from Sigma-Aldrich. Phosphate buffered saline (PBS) was purchased from Fisher Scientific.

### **6.2.2 Non-chemical incorporation of PVN and lignocellulosic matrices**

A nematicide of Abamectin (Abm) and a dye of Rhodamine (Rho) were infused separately into RCNMV capsid to form Abm-loaded plant viral nanoparticle (PVN<sup>Abm</sup>) and Rho-loaded plant viral nanoparticle (PVN<sup>Rho</sup>) according to previously mentioned methods (See Chapter 3). Subsequently, the PVN<sup>Abm</sup> or PVN<sup>Rho</sup> suspension was loaded into four lignocellulosic matrices (abaca, banana, softwood, softwood-hardwood). The formation and characterization of these

matrices were described in Chapter 4. The PVN<sup>Abm</sup> or PVN<sup>Rho</sup>-loaded matrices (PVN-matrix) were air dried overnight before characterization and application testing.

### **6.2.3 Characterization of PVN-loaded lignocellulose matrices**

#### *FE-SEM and EDS*

A JEOL JSM-6400F Field emission scanning electron microscopy (FE-SEM) was utilized to observe the surface change of lignocellulosic matrices after loading with PVN. FE-SEM is a high resolution electron microscopy that can reveal details of a sample surface at the nano-level scale. A 520  $\mu\text{l}$  aliquot of PVN suspension at a concentration of 2.3  $\text{mg ml}^{-2}$  was loaded into the each matrix (square sheet of 2.0  $\text{cm} \times 2.0 \text{ cm}$  in size). The samples were coated with Au sputtering before SEM measurement. Another SEM experiment were carried out in a Hitachi S3200N Variable Pressure SEM (VP-SEM) equipped with Oxford Energy dispersive X-ray spectroscopy (EDS) for elemental analysis on the matrix surface.

#### *Contact angle*

The contact angle measurements were carried out to determine the wettability of matrices before and after loading with PVN<sup>Abm</sup>. Contact angle goniometer (sessile drop technique) were measured by depositing 2  $\mu\text{l}$  of deionized (DI) water drop (bulk resistivity 14  $\text{M}\Omega\cdot\text{cm}$ ) on the matrix sample and recording the average contact angle as a function of contact time using a DataPhysics OCA goniometer equipped with a high speed camera (30 frames/second). Each specimen was measured in three replications.

#### **6.2.4 *In vitro* release profiles of PVN<sup>Rho</sup>-loaded lignocellulosic matrices**

The release behaviors of PVN<sup>Rho</sup> particles from the supporting lignocellulosic matrix was tested via a filtration assay. Briefly, a PVN<sup>Rho</sup>-matrix was placed as a filter paper in a column. Continuously, 12 aliquots of 100 µl DI water was flowed through the testing matrix and collected individually in the wells of a 96-well plate. Each collected fraction was assayed for the presence of released PVN<sup>Rho</sup> by measuring the fluorescence of Rho at the excitation wavelength of 530 nm and emission wavelength of 530 nm.

#### **6.2.5 Bioavailability of PVN<sup>Abm</sup>-loaded lignocellulosic matrices**

##### *Lethal dosage to C. elegans nematodes*

The bioavailability of PVN<sup>Abm</sup>-matrix against PVN<sup>Abm</sup> was assayed utilizing *C. elegans* nematodes. Since a previous study has shown the lethal dose 100 percent of PVN<sup>Abm</sup> that kills 100% of tested *C. elegans* nematodes is  $\sim 2.5 \times 10^{-7}$  M, PVN<sup>Abm</sup>-matrix and PVN<sup>Abm</sup> in suspension at an equivalent concentration were applied to a *C. elegans* nematodes ( $\sim 50$  individuals) culture. After 24-hours incubation at room temperature, the treated nematodes were evaluated on three scales: totally mobilized, impaired (50/50 mobilized/immobilized) and totally immobilized.

##### *Crop protection to Root knot nematode-infected plants*

PVN<sup>Abm</sup>-matrix and PVN<sup>Abm</sup> suspensions were applied to test the prevention of Root knot nematode (RKN) *Meloidogyne hapla* in 6-ounce foam cups under greenhouse condition. The cups were filled with sandy loam soil and pre-wetted prior to transplanting. Two-week-old

tomato seedlings that had uniform growth wrapped with a piece of PVN<sup>Abm</sup>-matrix (6 cm x 5 cm, 0.8 gram Abm per matrix). Then, the tomatoes seedlings were planted in the soil-filled cups and inoculated with RKN solution (5000 eggs) through three holes surrounding the root. The same amount of PVN<sup>Abm</sup> suspension was also applied in the soil as the positive control. Healthy plants without infection were taken as the negative control. Each treatment was run in triplicate, and the plants were watered as needed in the greenhouse. After 5 weeks of RKN inoculation, the roots of plants were harvested and gently washed with tap water. The galling on the root was evaluated in each treatment to determine the efficacy of crop protection for different PVN<sup>Abm</sup>-matrices.

## **6.3 Results and Discussion**

### **6.3.1 Characterization of PVN-loaded lignocellulosic matrices by contact angle, SEM and EDS**

Surface chemistry of PVN-matrices and virgin matrices was inferred by contact angle goniometer measurements. The previous study indicated that abaca, softwood, softwood/hardwood matrices showed immediate wicking of the water droplet thus the contact angle of water was not measurable (or taken to be zero). However, the banana matrix presented less absorbency or wicking and possessed a starting contact angle of 69° and that gradually decreased to 20° after 10 seconds. With the constant drop volume, **Figure 6.1a** shows a significant increase in the contact angle of PVN<sup>Abm</sup>-banana matrix, where the starting contact angle increased 104°, followed by a slow water absorption as indicated by a contact angle of 70° after 10 seconds. This increased starting contact angle and slow water adsorption would

be attributed by hydrophobic nature of Abm and PVN protein capsid, or the nanoscale surface roughness due to the presence of PVN<sup>Abm</sup> on the matrix.<sup>[3]</sup> The more hydrophobic nature of the PVN<sup>Abm</sup>-banana matrix is also consistent with the initial water contact angles of the other PVN<sup>Abm</sup> loaded matrices as well, but the water drop was quickly absorbed by matrix preventing accurate measurement. After increasing the loading amount of PVN<sup>Abm</sup> on the matrices, the change of contact angle on PVN<sup>Abm</sup>-matrix became more obvious. A starting water contact angle of 90° was detected in the PVN<sup>Abm</sup>-softwood matrix, which gradually decreased as shown **Figure 6.1b**.

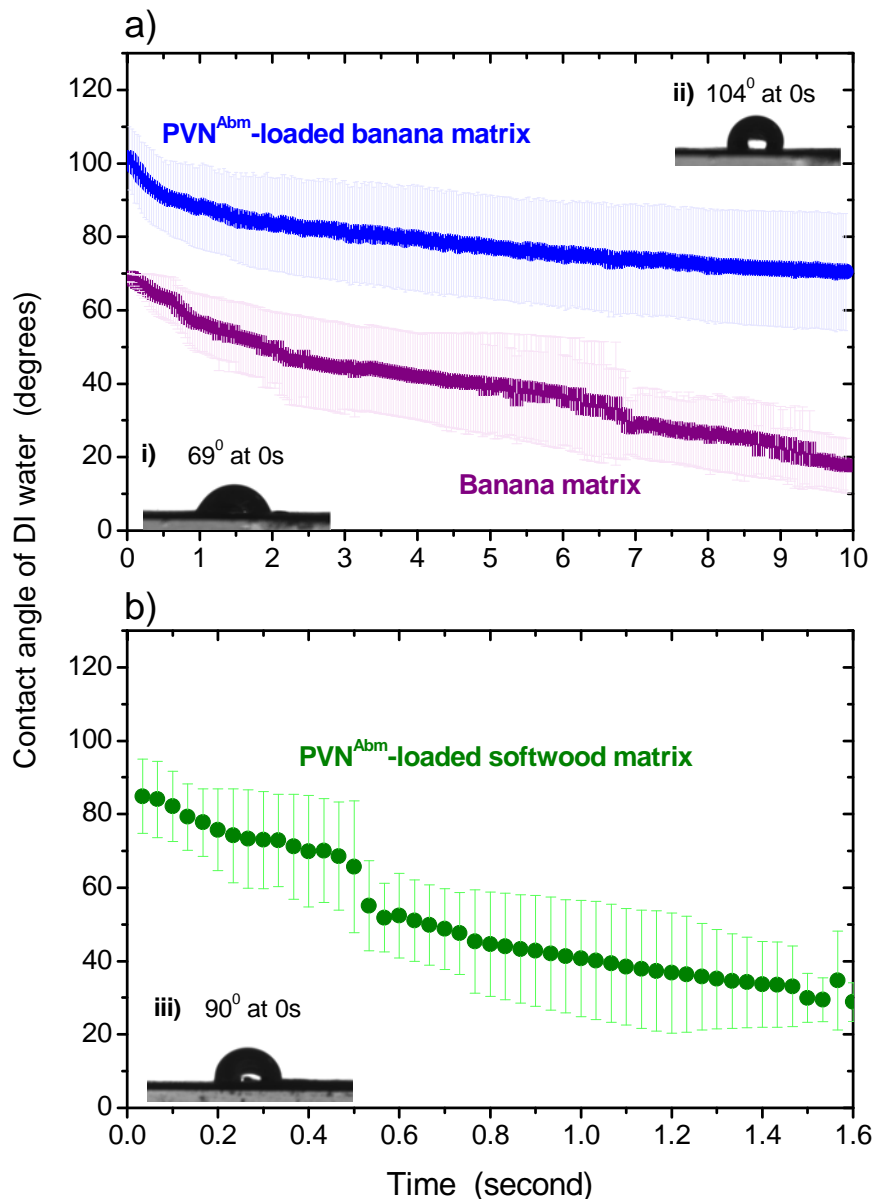


**Figure 6.1** Contact angle goniometer measurement for a) banana lignocellulosic matrix before and after loading with PVN<sup>Abm</sup> at the concentration of 0.3 mg cm<sup>-2</sup>; b) softwood lignocellulosic matrix after loading with PVN<sup>Abm</sup> at the concentration of 0.6 mg cm<sup>-2</sup>. The measurement for softwood matrix before loading were negligible due to immediate drop absorption resulting in an apparent water contact angle of 0°. The insert show photographs of water droplet on banana matrix i) before loading and ii) after PVN<sup>Abm</sup> loading; and iii) softwood matrix after PVN<sup>Abm</sup> loading at the contact time of zero

FE-SEM micrographs show a change on the surface of the banana matrix after loading with PVN<sup>Abm</sup>. Compared to virgin banana matrix (**Figure 6.2a** and **b**), PVN<sup>Abm</sup>-matrix presented a rough surface and appeared to be covered with small particles (**Figure 6.2c** and **d**). However, the size of these particles on the surface is much larger than a single PVN<sup>Abm</sup> 37 nm diameter particle. It is uncertain if the particles are the salt crystals from the sodium phosphate buffer used to suspend PVN, or formed by accumulation of PVNs. Therefore, the PVN<sup>Abm</sup> was measured with VP-SEM with EDS for element analysis (**Figure 6.3**). No change in the surface of PVN<sup>Abm</sup>-banana matrix was detected in VP-SEM imaging when compared to the virgin banana matrix due to its relatively lower resolution than FE-SEM. The EDS analysis of virgin banana matrix indicated that the matrix contained the main elements of C and O, and small amount of Ca elements (**Figure 6.3b**). Since the exterior surface of PVN is made of proteins, it was expected to show the N or S elements on the PVN<sup>Abm</sup>-matrix. However, only sodium was present in the EDS of PVN<sup>Abm</sup>-banana matrix (**Figure 6.3d**), attributed to the sodium phosphate buffer. Elemental nitrogen is normally difficult to detect in EDS analysis. This is because the element N with an atomic number between C and O is easily overlapped by the EDS intensity of C and O elements. Another limitation is that EDS is not a surface detection technique because its detection region is about 2 microns in depth. Therefore, if the PVN accumulated on the very top surface of the lignocellulosic matrix, EDS cannot detect its presence.

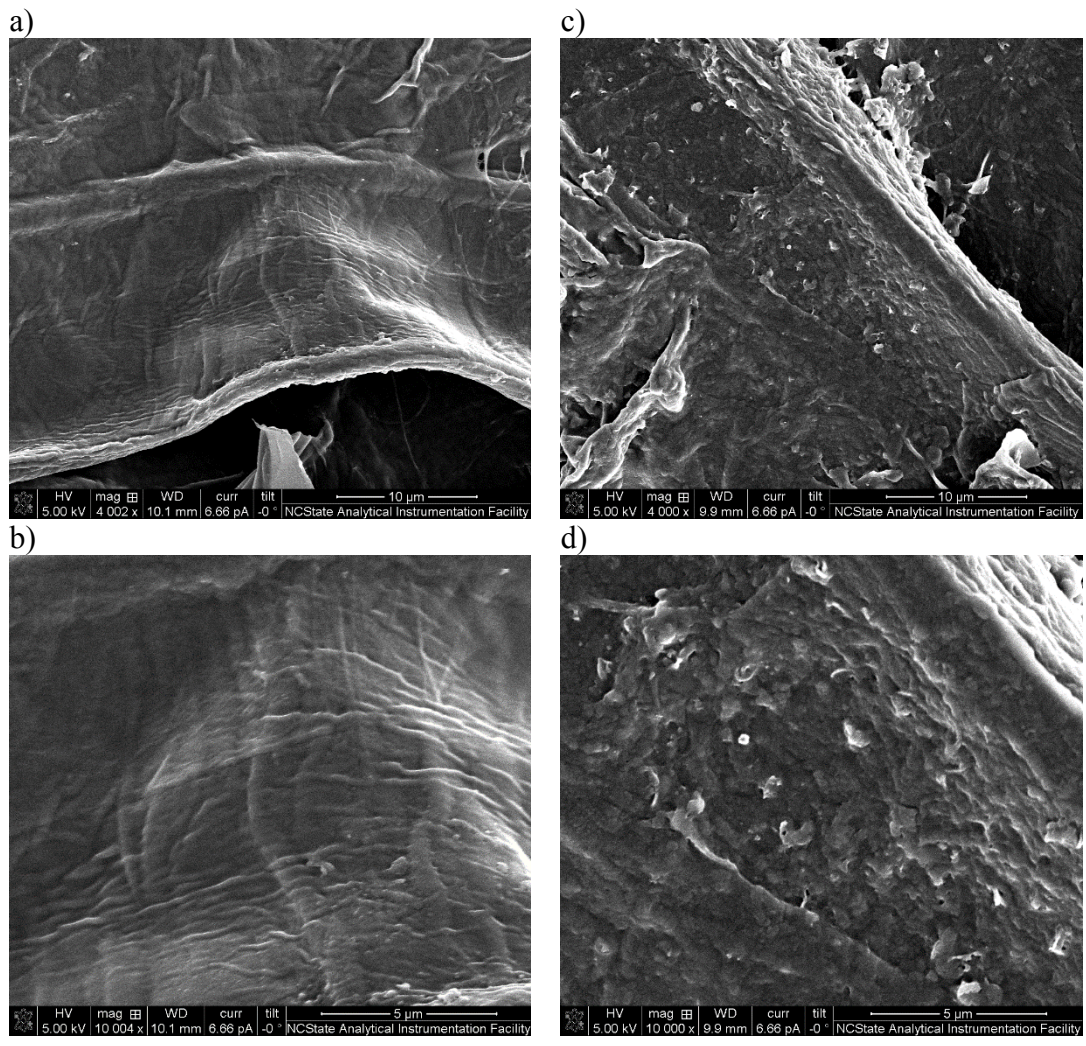


**Figure 6.2** Field emission scanning electron microscope (FE-SEM) micrographs of a) and b) untreated banana lignocellulosic matrix at magnification of 4kX and 10kX; b) and d) PVN<sup>Abm</sup> – loaded banana lignocellulosic matrix at magnification of 4kX and 10kX. \*PVN<sup>Abm</sup> were loaded on the matrix at the concentration of 0.3 mg cm<sup>-2</sup>.

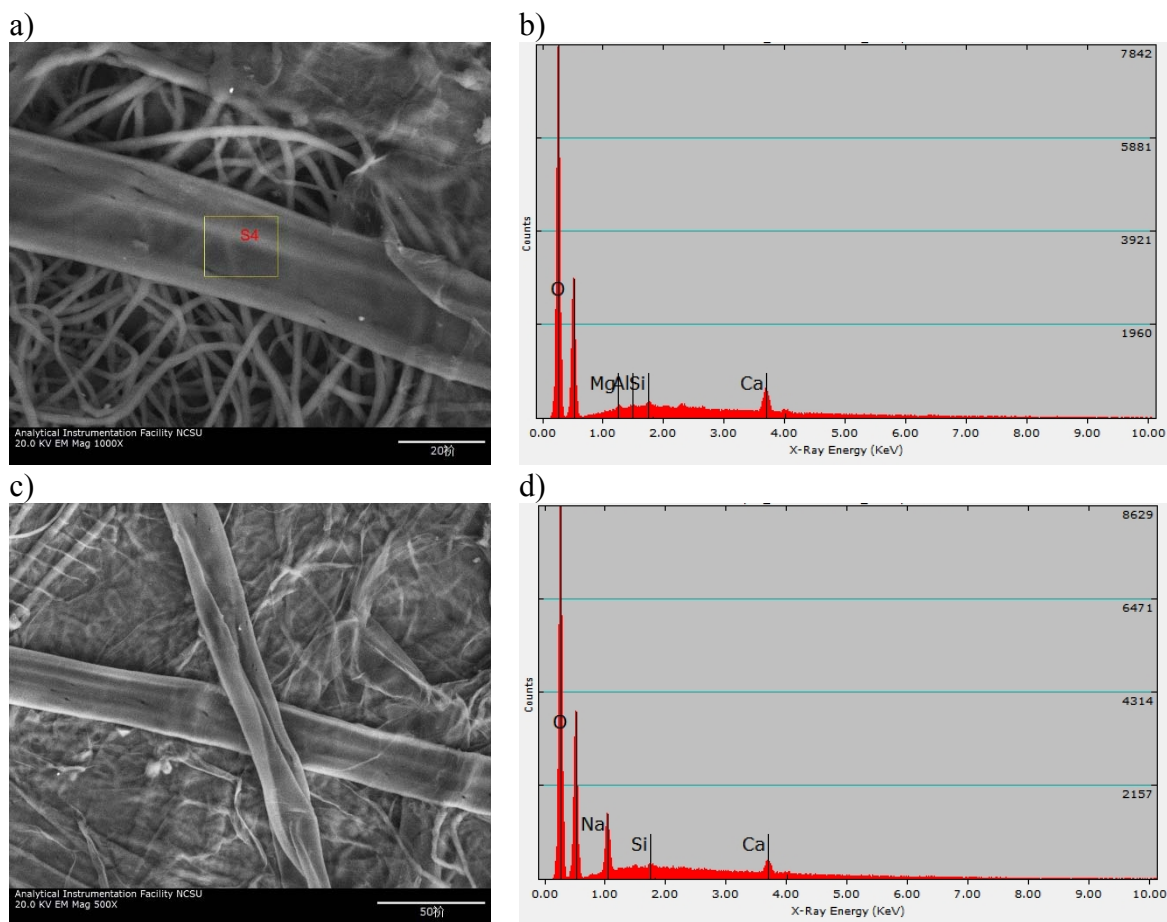


**Figure 6.3** Variable pressure scanning electron microscopy (SEM) micrographs and corresponding Energy dispersive X-ray spectroscopy (EDS) for a) and b) untreated banana lignocellulosic matrix; b) and d) PVN<sup>Abm</sup>-loaded banana lignocellulosic matrix. \*PVN<sup>Abm</sup> were loaded on the matrix at the concentration of 0.3 mg cm<sup>-2</sup>.

### 6.3.2 Release behaviour of PVN from supporting nonwoven matrices

**Figure 6.4** shows the release profiles of PVN<sup>Rho</sup> and free Rho after physisorption on different fiber matrices. Abaca, banana, softwood and hardwood are lignocellulosic materials from different sources, which resulted in distinct differences in the cargo release rate. The banana matrix exhibited a tendency to retain PVN<sup>Rho</sup> or free Rho with the potential for sustainable long-term release. Softwood matrices, on the other hand, possessed a burst release profile of loaded cargo (PVN<sup>Rho</sup> or free Rho). Softwood-hardwood matrices show the intermediate release rate of loading cargo between banana and softwood matrices. According to the desired release profiles, these fibrous matrices can be combined for multi-modal release behavior for cargo delivery. Compared with the release of free Rho from matrices, the total release of PVN<sup>Abm</sup> from abaca and banana matrices was increased from 4.4 % to 8.8 % and 62 % to 88 %, respectively; suggesting that matrix's interaction with PVN was different from matrix's interaction with free Rho. This results supported our hypothesis for this PVN<sup>Abm</sup>-matrix system that the release of active cargo from the PVN-matrix system varies with the binding affinities between all three components: Abm, PVN and fibrous matrix.

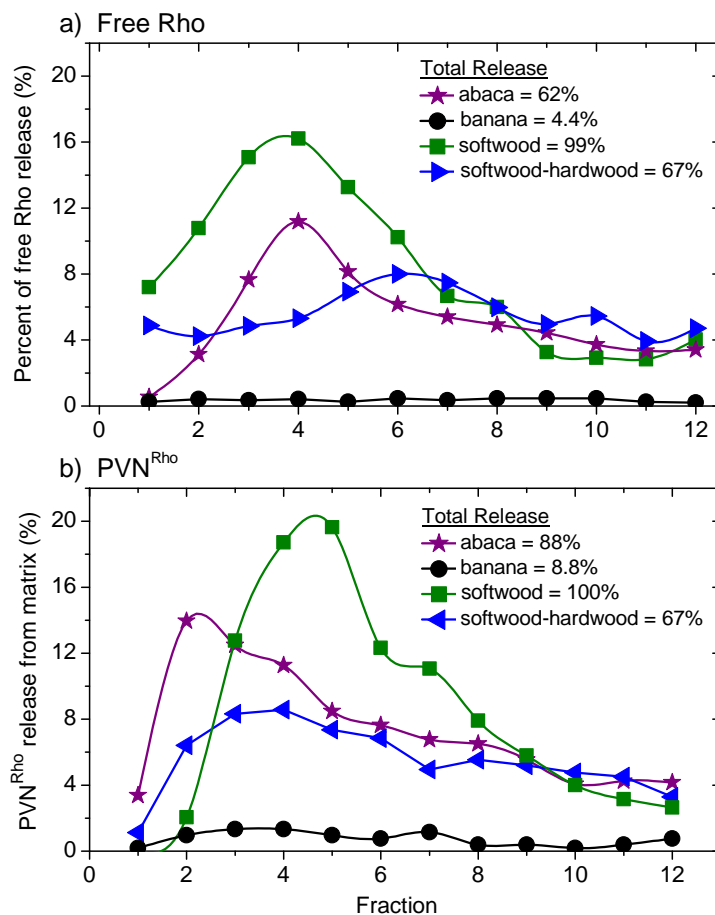


**Figure 6.4** Release of a) Free Rhodamine and b) PVN<sup>Rhodamine</sup> after physisorbed on different lignocellulosic matrices: abaca (★), banana (●), softwood (■) and softwood-hardwood (▲). The number represents the percent of total release for each fibrous matrix.

### 6.3.3 Bioavailability of PVN<sup>Abm</sup> to *C. elegans* nematode

Bioavailability of each PVN<sup>Abm</sup>-matrix was evaluated against PVN<sup>Abm</sup> suspension in a bioassay utilizing *C. elegans* nematodes. The nematode culture was directly dosed with the lethal concentration of  $2.5 \times 10^{-7}$  M with either PVN<sup>Abm</sup> suspension or PVN<sup>Abm</sup> loaded in the matrix. After 24-hour incubation, the evaluation of nematodes on a scale of totally mobilized, impaired (50/50 mobilized/immobilized) or totally immobilized for each treatment are

summarized in **Table 6.1**. PVN<sup>Abm</sup>-abaca and PVN<sup>Abm</sup>-softwood matrices caused 100 % of immobilized nematodes as PVN<sup>Abm</sup> in the suspension. This would be attributed by the burst release of PVN<sup>Abm</sup> from abaca and softwood matrices. In contrast, the slow-released banana and softwood-hardwood matrices only had 50% of nematode immobilization at the same concentration of PVN<sup>Abm</sup>. Hence, a certain amount of PVN<sup>Abm</sup> would remain in the banana and softwood-hardwood matrices. However, the different release of free Abm from lignocellulosic matrix didn't cause any change in the Abm's bioavailability. Based on this phenomenon, we infer that without PVN encapsulation, the retained Abm in fibrous matrix may be exposed to the nematode and thus result in the same bioavailability as free Abm in the solution. In contrast, the PVN-matrix system provided an additional mechanism of Abm controlled release.

**Table 6.1** Mortality of *C. elegans* nematodes dosed at lethal concentration with free Abm and PVN<sup>Abm</sup> in the suspension or loaded on the lignocellulose matrices via physisorption.

	Free Abm	PVN <sup>Abm</sup>	Fiber only
Lethal concentration, mol L <sup>-1</sup>	2.4 x 10 <sup>-7</sup> ± 0.2	2.5 x 10 <sup>-7</sup> ± 0.6	
Abaca	I	I	M
Banana	I	P	M
Softwood	I	I	M
Softwood-hardwood	I	P	M

Mortality of nematodes were evaluated in three scales: **I** totally immobilized, **P** impaired at 50/50 mobilized/immobilized and **M** totally mobilized.

### 6.3.4 Crop protection of PVN<sup>Abm</sup>-loaded lignocellulosic matrices

The crop protection of these PVN<sup>Abm</sup>-matrices were tested in tomato seedlings that were infected with Root knot nematode (RKN) *Meloidogyne hapla* in the sand loam soils. After 5 weeks of RKN inoculation, the crop protection of PVN<sup>Abm</sup>-matrices was evaluated based on the scales of gallings on the roots. As listed in **Table 6.2**, compared to PVN<sup>Abm</sup> in suspension (2.8 of galling), loading PVN<sup>Abm</sup> in the matrix didn't improve its nematicide efficacy for nematode control. Among all matrices, PVN<sup>Abm</sup>-banana (3.0 of galling) and PVN<sup>Abm</sup>-softwood (3.25 of galling) matrices demonstrated better crop protection than abaca (4.0 of galling) and softwood-hardwood (3.67 of galling) matrices. Compared to the crop protection result of Abm-loaded matrices (Chapter 4), PVN<sup>Abm</sup>-loaded matrices shown the reduced activity against nematode within the soil. One possible reason would be the release of free Abm from PVN-loaded matrix. Without PVN carrier, released Abm have a high potential to bind to the organic particles in the soil;<sup>[4, 5]</sup> resulting in the limited zone of protection around the developing root system.

**Table 6.2** Crop protection results of PVN<sup>Abm</sup> and PVN<sup>Abm</sup> -loaded lignocellulosic matrices to tomato plants infected with *Meloidogyne hapla* nematode in greenhouse.

Evaluation	Infected control	PVN <sup>Abm</sup>	PVN <sup>Abm</sup> -loaded lignocellulosic matrices			
			Abaca	Banana	Softwood	Softwood-hardwood
Root galling score <sup>a</sup>	4.00	2.80	4.00	3.00	3.25	3.67

<sup>a</sup> Plant root galling score determined at 5 weeks after treatment, obtained using a 0 - 4 unit-scale where 0 = no galling of uninfected plants and 4 = worst galling of infected plants. Data were reported by means of three replications.

## 6.4 Conclusion

We have shown the feasibility of incorporating plant viral nanoparticle (PVN) infused with nematicides, abamectin (Abm), into lignocellulosic matrices for tailorable release of active agent for nematode control. Varying the supporting lignocellulosic matrices that were different in chemical compositions and physical properties provided an additional approach for controlled release transport mechanism of abamectin based on the interactions among all three components: Abm, PVN and fibrous matrix. While their interactions are not yet elucidated, the slow and sustainable delivery of Abm is achieved by physically loading PVN<sup>Abm</sup> into banana matrix, which showed a delayed activity against *C. elegans* nematode in liquid culture. In contrast, incorporating PVN<sup>Abm</sup> into abaca and softwood matrix resulted in a burst release of active agent, thus it showed the same nematicide activity as free Abm in the solution. Loading PVN<sup>Abm</sup> in lignocellulosic matrix didn't improve its nematicide effectiveness in the soil condition. Contact angle measurement and scanning electron microscopy suggested that PVN<sup>Abm</sup> may be present on the surface of fiber, but integrity and stability of PVN<sup>Abm</sup> after loading on the matrix are still unknown. Therefore, future work is needed to characterize the PVN on the matrix by transmission electron microscopy or confocal laser scanning microscopy. A compromised PVN capsid would cause the release of free Abm that would bind to soil and so lost bioavailability to nematode. Another incorporation method for PVN and fibrous matrix such as chemical conjugation is also recommended in the further work. The specific chemical binding between PVN and fibrous matrix would enable the release of PVN by some environmental triggers, such as pH, light, oxidation or reduction.

## 6.5 Reference

- [1] P. Singh, M.J. Gonzalez, M. Manchester, Viruses and their uses in nanotechnology, *Drug Development Research*, 67 (2006) 23-41.
- [2] Y. Ren, S. Wong, L. Lim, Application of Plant Viruses as Nano Drug Delivery Systems, *Pharmaceutical research*, 27 (2010) 2509-2513.
- [3] P. Roach, N.J. Shirtcliffe, M.I. Newton, Progress in superhydrophobic surface development, *Soft Matter*, 4 (2008) 224-240.
- [4] K.A. Krogh, T. Søbørg, B. Brodin, B. Halling-Sørensen, Sorption and Mobility of Ivermectin in Different Soils All rights reserved. No part of this periodical may be reproduced or transmitted in any form or by any means, electronic or mechanical, including photocopying, recording, or any information storage and retrieval system, without permission in writing from the publisher, *J. Environ. Qual.*, 37 (2008) 2202-2211.
- [5] V.F. Gruber, B.A. Halley, S.C. Hwang, C.C. Ku, Mobility of avermectin B1a in soil, *Journal of Agricultural and Food Chemistry*, 38 (1990) 886-890.

## Chapter 7. Summary and Outlook

### 7.1 Summary

The overall aim of this Ph.D. dissertation was to develop a hybrid active-delivery matrix comprising plant viral nanoparticles (PVNs) and polymeric fibrous materials to enable precise delivery and tunable release of active ingredients for particular applications. Combining active cargo infused PVNs with a fibrous matrix leads to a “smart” delivery system that enables the controllable release features from both components. We have built upon past work that utilized the reversible structural dynamics to divalent cation depletion and re-addition for *Red clover necrotic mosaic virus* (RCNMV) derived PVNs for controllable drug delivery and translated this technology as a nanotechnology for agricultural applications.

We enhanced the understanding of the PVN technology by elucidating its mechanism for loading and release of charged molecules via using a chemotherapeutic drug, doxorubicin (Dox), as a model molecule for the active ingredient. Of critical importance is the methodology for defining tunable release profiles of PVN via manipulation of the Dox’s loading capacity and the specificity of the drug’s binding locations on the exterior or interior of the PVN. This was determined with electrokinetic characterization of RCNMV as a function of the buffer system and divalent ion concentration during the formulation of PVN. We found that the outer surface of the RCNMV was more negatively charged in the phosphate buffer at pH7.5, which dictated the maximum surface binding of positively

charged Dox resulting in burst release profiles. Conversely, to minimize surface-bound Dox with PVN, we used a cationic buffer to allow for maximum Dox infusion into the virus interior as there was not competing ions in the buffer system. This allowed for a controlled release profile of Dox after formulation of PVN<sup>Dox</sup> upon exposure to the appropriate environmental condition. These results are significant because the foundational understanding of the PVN formulation methodology enables process robustness for science-driven commercialization, a critical need in the biotechnology community.

This PVN system was further exploited as a nanocarrier for delivery of the nematicide, abamectin, for the plant parasite nematode control. As a neutral molecule, Abm was not attracted to the negatively charged outer surface of PVN. The formulation of Abm with RCNMV resulted in a complete infusion/ encapsulation within the virus with a loading capacity of ~177 Abm molecules in each protein capsid and the loading efficiency of 37 %. The encapsulation of Abm into the PVN addressed the Abm's lack of mobility in soil conditions to render a controlled release strategy for the Abm bioavailability during application. As a result, the PVN<sup>Abm</sup> enlarged the zone of protection around a root system that was previously limited by granular or liquid application of free Abm within the soil. This improved Abm formulation enhanced the nematicidal performance for better root knot nematode control. However, it was found that the release of loaded Abm from PVN is dependent on the PVN's inherent structural dynamics response to environmental stimuli; by combining the PVN delivery mechanism with a polymeric material, we expect to have another mechanism to tailor active ingredient delivery for any given application. We have

chosen to use lignocellulosic materials due to their abundance in nature and beneficial biodegradation components to agricultural systems.

The lignocellulosic materials, the composite biopolymer containing cellulose, hemicellulose and lignin, were utilized to form fibrous matrices to enable the additional controlled release mechanism. We evaluated as them as a supporting matrix for loading and releasing either free Abm or PVN<sup>Abm</sup>. Abaca, banana, softwood and hardwood were the sources for the lignocellulosic materials. Incorporating Abm into these matrices via physisorption yielded a distinct difference in the Abm release profiles as compared to free Abm. In addition, these release profiles were dependent on chemical compositions of lignocellulosic materials. The slow and sustainable release of Abm was achieved with banana matrix comprising a higher amount of lignin in the bulk. This slower release appeared to provide long-term crop protection around the plant root. In contrast, the decreased amount of lignin in abaca and woodfiber matrices led to the fast release of loaded Abm, hence compromised the delivery of Abm to the growing root system of the plants.

A hybrid delivery matrix was fabricated by incorporating PVN<sup>Abm</sup> into a lignocellulosic matrix. In this case, the tailorable release of Abm is determined by 1) PVN, 2) the matrix composition and 3) the combined component interactions. Although structural dynamics of PVN to environmental stimuli enables the triggered release of loaded Abm, varying the supporting lignocellulosic matrices that are different in chemical compositions and physical properties provides an additional release transport mechanism of Abm for nematode control. Combing PVN<sup>Abm</sup> into abaca and softwood matrices resulted in a burst release of PVN<sup>Abm</sup> displaying the same effectiveness to *C. elegans* nematode as free PVN<sup>Abm</sup> in the solution. On

the other hand, the slow and sustainable delivery of Abm was achieved by loading PVN<sup>Abm</sup> into a banana matrix, which exhibited a retarded activity against the nematodes in liquid culture. However, loading PVN<sup>Abm</sup> in lignocellulosic matrices didn't improve its nematicide efficacy in the soil condition, which would be attributed by release of free Abm from PVN<sup>Abm</sup>-matrix. In summary, although incorporating cargo loaded PVN into a fibrous matrix shows an ability to additionally tune the release of loading cargo, the stability of PVN on the matrix and interaction between them needs to be more thoroughly understood to optimize the application of this delivery system.

## **7.2 Recommendations for Future Work**

Throughout the research of this Ph.D. dissertation, there seems to be unlimited options and opportunities for future work. The findings of this work demonstrated that the mutual interactions among 1) active ingredient, 2) PVN and 3) fibrous matrix dictate the delivery and release of the active ingredient. However, there are more options and techniques that could be conducted to optimize this “smart” delivery system for different applications. In the remainder of this chapter, we will discuss some recommended work that includes the additional manipulation of loading cargo and PVNs, incorporating PVN with other fiber materials, and using chemical conjugation of PVN on the surface of supporting matrix to create nano-scale topographical features.

### **7.2.1 Chemical conjugation of loading cargo into interior capsid of PVN**

In the Chapter 3, we found the electrostatic interactions between loading cargo and PVN determines its loading capacity and loading location on / within the PVN as well as the

subsequent release profiles. The future work can be carried out to introduce a new interaction between guest cargo and PVN capsid for desired loading or release properties. For instance, previous studies indicated that the lysine residues (-NH<sub>2</sub>) on R domain (Interior) of RCNMV's protein capsid were accessible to be conjugation with specific targeting peptide via a cross-linker of sulfosuccinimidyl-4-(N-maleimidomethyl) cyclohexane-1-carboxylate (sSMCC).<sup>[1]</sup> During this reaction, as illustrated in **Figure 7.1**, the *N*-Hydroxysuccinimide (NHS) ester group on sSMCC was reacted with lysine residues of RCNMV, and then the RCNMV-sSMCC maleimide moiety was reacted with cysteine (-SH) on the peptide. Therefore, If we can introduce a -SH group to the loading cargo, the chemical conjugation could be conducted by a similar reaction scheme. In Chapter 4, the results showed that only ~177 Abm molecules were loaded into each PVN capsid due to weak interactions between RCNMV's anionic RNA and neutral Abm. Therefore, rendering a chemical conjugation between Abm and PVN internal cavity is expected to increase the loading capacity of PVN<sup>Abm</sup>, and meanwhile the properties of specific chemical interaction could enable an additional controlled release function. The exterior protein shell of PVN<sup>Abm</sup> can be labeled with biological peptide for targeted delivery and increased uptake by nematode.

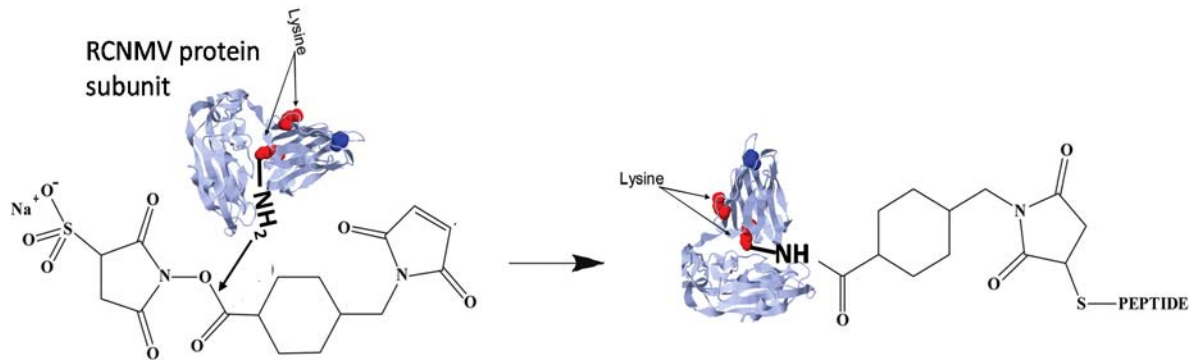


**Figure 7.1** Schematic of chemical conjugation of lysine residues of RCNMV capsid with cysteine-terminated peptide via a cross-linker of sSMCC.

### 7.2.2 Additional fibrous materials for PVN incorporation.

In Chapter 5, it was concluded that different lignin amounts and distribution in the lignocellulose matrix varied the release of loaded Abm from the supporting matrix due to the hydrophobic interaction between Abm and lignin. This finding will be carried over to make fibrous matrices containing different lignin amounts and lignin distribution to control the release of Abm at specific rates. Moreover, the fabrication of PVN-matrix with other fibrous materials and incorporation methods can be designed according to different potential applications. Besides the lignocellulosic matrices that have been studied, cargo-infused PVN can be incorporated into biodegradable polymeric matrix or biodegradable elastomeric polyester by physisorption, in situ processing, or chemical conjugation. Our preliminary work has shown a successful incorporation of ethidium bromide-infused PVN (PVN<sup>EtBr</sup>) into poly (ethylene oxide) (PEO) fibrous matrix via co-electrospinning (**Figure 7.2**). At the same electrospinning condition, adding PVN<sup>EtBr</sup> into PEO solution resulted in nanofibrous matrix with the smaller fiber diameter. The decreased fiber diameter would increase the surface area

of fibrous matrix to the environments and so enhancing its delivery efficiency of loading cargo. The water-soluble and biodegradation properties of PEO materials allow for additional controlled transport mechanism of PVN and its infused molecules. Poly(caprolactone) (PCL) has the advantages of being highly extensible (over 500% elongation before break) and biodegradable.<sup>[2, 3]</sup> It has also been shown that when chitosan, a natural polysaccharide, was grafted to PCL, the extensibility (or strain) of the polymer exceeded 1500% of its original length.<sup>[4]</sup> The rate of biodegradation also has been tuned by the addition of starch.<sup>[5]</sup> Therefore, incorporating PVN<sup>Abm</sup> with PCL or PCL-starch fibrous matrix is expected to yield a hybrid delivery matrix with appropriate mechanical properties that can extend with the growing root to provide a sufficient zone of protection around the root mass to protect against nematode infestation.

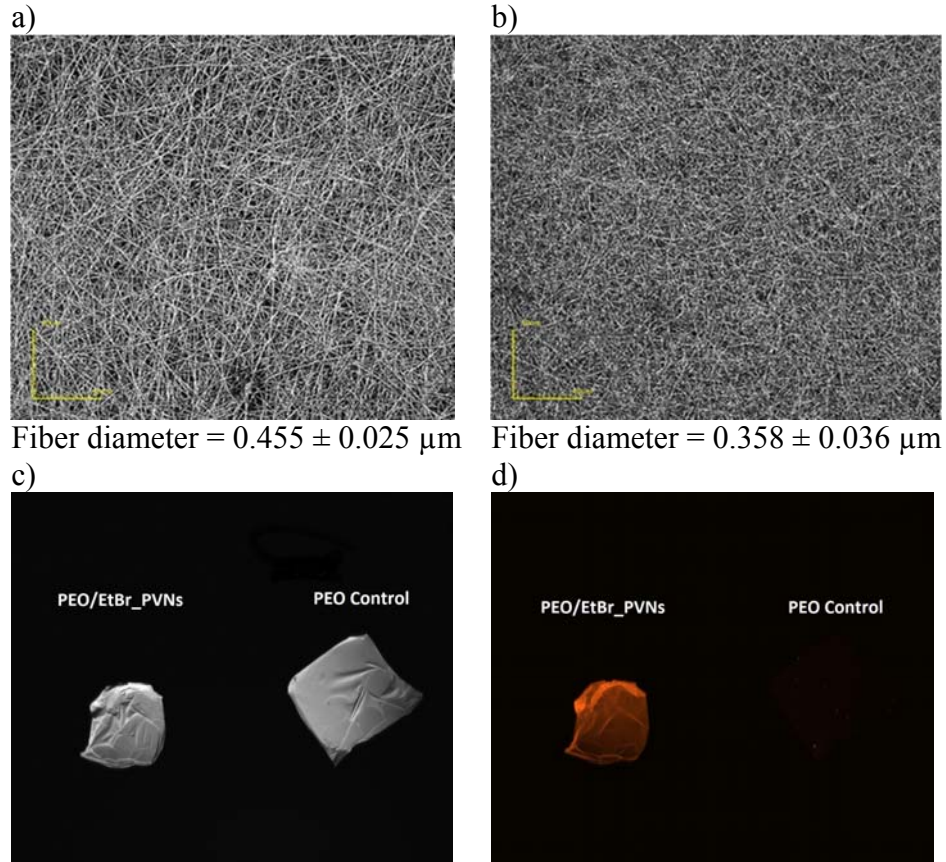


**Figure 7.2** Laser confocal microscope images of a) electrospun PEO matrix and b) co-electrospun PEO matrix with ethidium bromide-infused PVN (PVN<sup>EtBr</sup>); Images of PVN<sup>EtBr</sup>-PEO and PEO electrospun matrices under c) white light and d) VU light. The fluorescence emitted from PVN<sup>EtBr</sup>-PEO matrix indicated that PVN<sup>EtBr</sup> were uniformly incorporated into PEO fibers by co-electrospinning. Both matrices were electrospun at the voltage of 12 kV, flow rate of 5ul/min and distance of 16cm.

### 7.2.3 Chemical Conjugation of PVNs into polymeric matrices

The well-defined nanoscale topographies of plant viral nanoparticles have attracted much attention in applications of electronics, sensing and biomedical engineering. It would be a great benefit to uniformly tether PVNs on the polymeric matrices while preserving their active delivery properties. This can be carried out with two separate reaction schemes on

cellulose substrates: 1) *N*-hydroxysuccinimid (NHS) substrate activation and 2) maleimide substrate activation as described below:

1) *NHS/EDC Reaction of PVN-(NH<sub>2</sub>)<sub>x</sub> and Polymeric Matrix.*

*N*-Hydroxysuccinimid (NHS) is commonly reacted with lysine residues (-NH<sub>2</sub>) of viral capsid.<sup>[6]</sup> Introduction of 1-ethyl-3-[3-dimethylaminopropyl]-carbodiimide (EDC) can chemically conjugate NHS to carboxyl groups of substrate. **Figure 7.3** illustrates a NHS/EDC grafting reaction to chemically bind PVN into a cellulose matrix: a) creating carboxylated cellulose substrate by (carboxymethylated cellulose) CMC adsorption; b,c) CMC-modified cellulose will react with NHS/EDC to form a NHS activated surface; and d) PVN-(NH<sub>2</sub>)<sub>x</sub> will react with NHS and chemically tethered to a cellulose matrix.

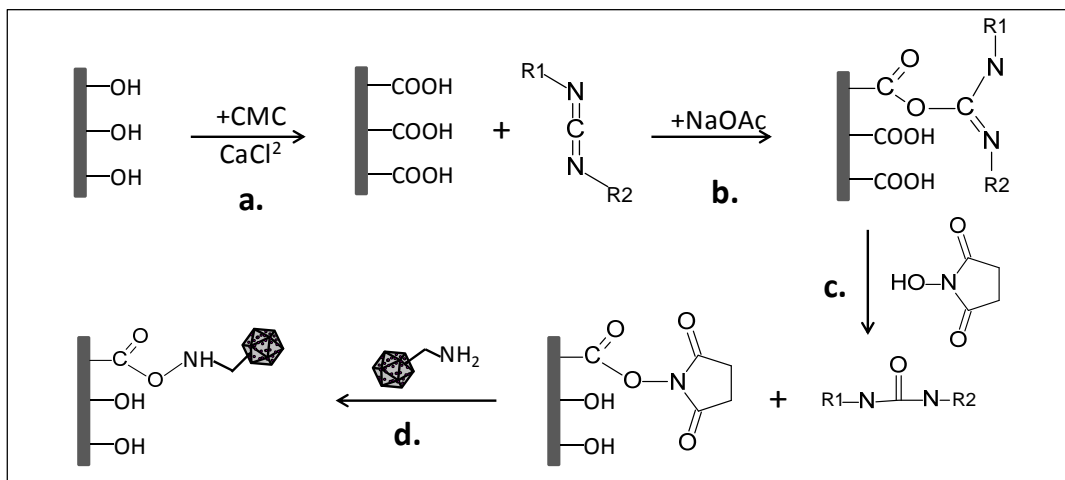


**Figure 7.3** Schematic of NHS/EDC reaction for reacting the lysines of PVN capsid with a cellulose matrix.

## 2) Thiol-maleimide Reaction of PVN-(SH)<sub>x</sub> and Polymeric Matrix.

The cysteine residues of viral capsid can be chemical conjugated to the polymer substrate via a thiol-maleimide reaction. Using a cellulose matrix as the model polymer to demonstrate the approach (see **Figure 7.4**): a) amino groups will be introduced to cellulose via a silane coupling (3-aminopropyltriethoxysilane (3-APTES)) through the condensation reaction between Si-OH of silane coupling agent and C-OH of cellulose; b) NH<sub>2</sub> activated cellulose will react with 3-(maleimido)propionic acid N-hydroxysuccinimide ester (MPS) to form a maleimide activated surface; c) PVN-(SH)<sub>x</sub> will be chemically grafted to cellulose matrix via a thiol-maleimide reaction.

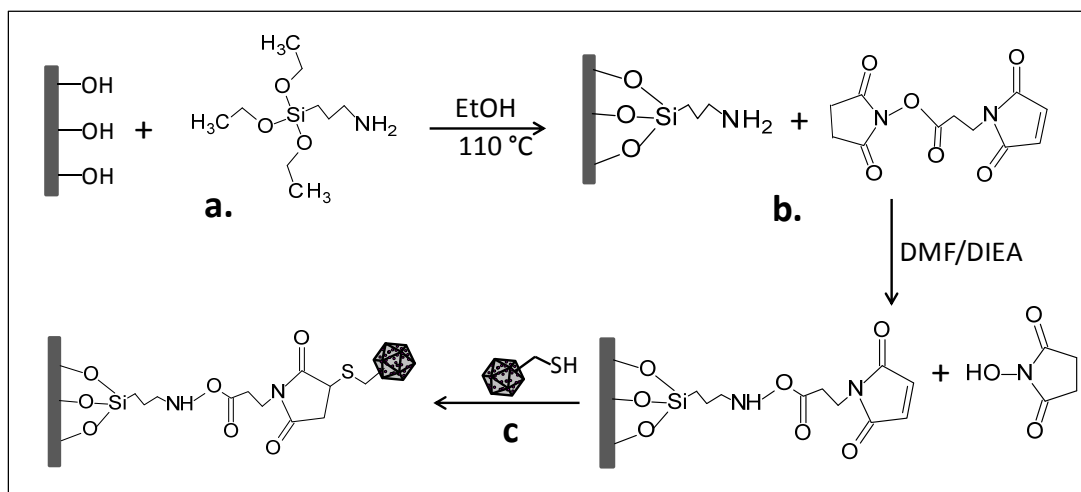


**Figure 7.4** Schematic of thiol-maleimide reaction for tethering the PVN capsid to a cellulose matrix.

Accomplishment of this work is expected to provide a PVN-immobilized matrix with well-defined nanoscale topographies as well as triggered release features for the active ingredient. The utilization of this PVN-immobilized matrix could be tested, but not limited, in two applications:

- Nematicide-loaded PVN immobilized biodegradable matrix for nematode control where the release of nematicide will be further tailored by degradation rate of matrix
- Lidocaine-loaded PVN immobilized matrix for skin regenerations where the nanoscale feature of PVN will improve epidermal cells (keratinocytes) differentiation and released lidocaine molecules will relieve pain.

### **7.3 Reference**

- [1] R. Wang, D.M. Lockney, M.B. Goshe, S. Franzen, Mass Spectrometric Detection of Targeting Peptide Bioconjugation to Red clover necrotic mosaic virus, *Bioconjugate Chemistry*, 22 (2011) 1970-1982.
- [2] P. Wutticharoenmongkol, N. Sanchavanakit, P. Pavasant, P. Supaphol, Preparation and Characterization of Novel Bone Scaffolds Based on Electrospun Polycaprolactone Fibers Filled with Nanoparticles, *Macromolecular Bioscience*, 6 (2006) 70-77.
- [3] M.M.-U. Haque, M.E. Errico, G. Gentile, M. Avella, M. Pracella, Functionalization and Compatibilization of Poly( $\epsilon$ -caprolactone) Composites with Cellulose Microfibres: Morphology, Thermal and Mechanical Properties, *Macromolecular Materials and Engineering*, 297 (2012) 985-993.

- [4] Z. Zhou, H. Huang, P. Xu, L. Fan, J. Yu, J. Huang, Simultaneous enhancement of the strength and elongation of polycaprolactone: The role of chitosan-graft-polycaprolactone, *Journal of Applied Polymer Science*, 112 (2009) 692-699.
- [5] M.A. Huneault, H. Li, Preparation and properties of extruded thermoplastic starch/polymer blends, *Journal of Applied Polymer Science*, 126 (2012) E96-E108.
- [6] N.F. Steinmetz, D.J. Evans, G.P. Lomonosoff, Chemical Introduction of Reactive Thiols Into a Viral Nanoscaffold: A Method that Avoids Virus Aggregation, *ChemBioChem*, 8 (2007) 1131-1136.